

**MICRO/NANOSCALE TRIBOLOGY AND MECHANICS OF
COMPONENTS AND COATINGS FOR MEMS**

DISSERTATION

Presented in Partial Fulfillment of the Requirements for the
Degree Doctor of Philosophy in the Graduate School of
The Ohio State University

By

Sriram Sundararajan, M.S.

* * * * *

The Ohio State University
2001

Dissertation Committee:

Professor Bharat Bhushan, Adviser

Professor Bernard J. Hamrock

Professor J. William Rich

Approved by

Adviser

Department of Mechanical Engineering

ABSTRACT

'Microelectromechanical systems' (MEMS) is the collective term for microcomponents and microdevices that have been developed using lithography-based and other techniques with physical dimensions ranging from a couple to a few hundred microns. Several studies have shown that tribology (friction and wear) is an important factor affecting the performance and reliability of MEMS. Good mechanical properties are also critical for mechanical integrity of microstructures. There is a need to develop a fundamental understanding of tribological phenomena and to evaluate mechanical properties on the scale pertinent to MEMS. This research addresses this need using atomic force microscopy (AFM)-based experimental techniques.

To address the problem of friction, a study of the static friction of polysilicon micromotors was performed. A technique to measure the static friction forces in the devices was developed and forces measured indicated that the coefficient of static friction for unlubricated motors was far larger than one. A molecularly thin bonded layer of perfluoropolyether lubricant appeared to reduce the static friction and rendered the contact interfaces insensitive to the environment. Meniscus effects and surface roughness characteristics of the contacting surfaces were identified as the mechanisms for high friction.

To address the problem of wear, ultra-thin hard amorphous carbon coatings for use as protective coatings were studied. Nanoscale scratch and wear studies were conducted to identify the optimum coating properties for the best scratch/wear resistance. Ploughing, associated with plastic deformation, was identified as the initial failure mechanism followed by brittle fracture and delamination. High hardness and matching of elastic modulus values of the coating and the substrate promoted better scratch/wear resistance.

AFM-based techniques to evaluate mechanical properties of nanometer-sized silicon and silica (SiO_2) beams under static and dynamic loading were developed. Elastic modulus and fracture toughness appeared to be comparable to bulk values while bending strength values were on order of magnitude higher than values obtained from larger specimens. Cleavage fracture appeared to be the failure mechanism under both static and dynamic loading.

Surface topography is known to have a significant effect on localized friction on the nanoscale, which is pertinent to tribology of MEMS. The effect of surface topography on the friction forces measured using an AFM was studied to understand its origins and to clarify confusing interpretations in the literature. Topography-induced transitions in the friction signal always corresponded to transitions in surface slope even when friction signals from opposing scan directions are subtracted. The ratchet mechanism and the dynamic effect of an AFM tip colliding against a surface feature with a sudden increase in slope were found to be the reasons for this observation.

Dedicated to my wife, Sumana
my parents
and to the loving memory of my mother-in-law

ACKNOWLEDGMENTS

I would first like to thank my adviser, Prof. Bharat Bhushan for giving me the chance to work with him for my graduate degrees. I am grateful for his guidance and the resources of his state-of-the-art laboratory. He is an advisor and manager from whom I have learnt a great deal. I thank my committee members who also served on my candidacy examination committee: Prof. Bernard Hamrock and Prof. William Rich. Their encouragement and advice have been invaluable. I would also like to express my gratitude to the following faculty; Prof. Vish Subramaniam (ME), who served on my Master's examination committee and who has engaged in useful discussions during the course of this work; Prof. Mark Walter (ME) for providing valuable insight into fracture mechanics and Prof. David Rigney (MSE) for his discussions on materials issues of silicon and general encouragement.

I would like to thank the following collaborators who made it possible to perform the various studies reported in this dissertation. The micromotor samples were provided by Dr. N. Fabre and V. Conedera during their visit to Ohio State from LAAS-CNRS, Toulouse France. I am extremely grateful to them and to Dr. H. Camon, (also of LAAS-CNRS), for their discussions regarding the fabrication processes and for their views on the friction problems associated with the motors. The nanobeam samples were prepared by T. Namazu and Prof. Y. Isono of the Dept. of Mechanical Engineering at Ritsumeikan University, Japan. They also graciously engaged in several productive discussions during the course of this study. The DLC coatings used in the study were obtained from Commonwealth Scientific, Alexandria, Virginia; Veeco Instruments, Plainview, New York; Shimadzu, Hadano City, Kanagawa, Japan and Quantum Inc., Shrewsbury, Massachusetts.

The following people deserve my sincere thanks for their expertise and assistance: John Mitchell (of MARC in Geological Sciences) and Cameron Begg (of CEOF, MSE) performed scanning electron microscopy; Hendrik Colijn (of CEOF in MSE) and Joel Haynes (Chemistry) performed Auger electron spectroscopy and X-ray photoelectron spectroscopy, respectively; Jerry Kingzett (ME), who never failed to produce the various scopes, probes and other basic laboratory accessories that are essential for research; Joseph West (ME) for his assistance in troubleshooting my less than impressive electronic circuits; Mary Richards, Adrian Thomas, Grace Hines, Carol Bird and other staff at the ME department offices; Mike Holmstrom, Pat McPhail, Jean Jarvaiz, Mike Mayburn and others of the technical support division at Digital Instruments who have helped me with various problems and issues in AFM maintenance and troubleshooting.

I could not have lasted all these years without the friendship and company of my colleagues in the lab. They have been a source of entertainment and support. I thank Bill Scott, Zheming Zhao, Xiaodong Li, Sameera Chilamakuri, Weihua Sheng, Sumit Chandra, Wei Peng, Prasad Mokashi, Nikhil Tambe, and other friends. Some have also offered valuable discussions and assisted me during this work. Dr. Xiaodong Li performed mechanical property measurements using the nanoindenter. Dr. Zheming Zhao and Dr. Huiwen Liu assisted with lubrication of micromotors. David Lee performed sample cleaning for the nanobeam samples and saved the project. I thank the other members of the lab who have offered me their assistance.

I would like to express my heartfelt gratitude to my colleagues in the AFM group, past and present: Volker Scherer, Derik DeVecchio, M.S. Bobji, Anton Goldade, Huiwen Liu and David Lee. They have been constant sources of fun, knowledge and inspiration through all the good and bad times in the lab and have helped me to think and work better as a researcher.

The financial support for this research was provided by the National Science Foundation (Contract No. ECS-9820022). The content of this information does not necessarily reflect the position or policy of the Government and no official endorsement should be inferred.

Finally I would like to thank my parents, without whom I would not be what I am today, my father-in-law for his constant encouragement and the one person who has been my strongest source of strength and inspiration, my wife, for her patience, love and support through all these years.

VITA

February 15, 1974.....Born – Madras, India

1995B.E. (Hons.) Mechanical Engineering
Birla Institute of Technology and Science, Pilani, India

1997M.S., Mechanical Engineering
The Ohio State University

January 1996 - present.....Graduate Research Associate,
The Ohio State University

PUBLICATIONS

Research Publications

1. Sundararajan, S. and Bhushan, B. (2001), “Micro/Nanoscale Tribology of MEMS Materials, Lubricants and Devices,” (keynote paper), in *Proceedings of the Second World Tribology Congress*, edited by F. Franek, W. J. Bartz, and A. Pauschitz, The Austrian Tribology Society, Vienna, Austria, Sept. 2001, 347-359.
2. Sundararajan, S. and Bhushan, B. (2001), “Static Friction Force and Surface Roughness Studies of Surface Micromachined Electrostatic Micromotors Using an Atomic Force/Friction Force Microscope”, *Journal of Vacuum Science and Technology A* **19**, 1777-1785.
3. Sundararajan, S. and Bhushan, B. (2001), “Micro/Nanoscale Tribology of MEMS Materials, Lubricants and Devices”, in *Fundamentals of and Bridging the Gap between the Macro and Micro/Nano Scales*, edited by B. Bhushan, NATO Science Series II - Mathematics, Physics and Chemistry, Kluwer Academic Publishers, Dordrecht, Netherlands, 821-850.
4. Sundararajan, S. and Bhushan, B. (2001), “Development of a Continuous Microscratch Technique in an Atomic Force Microscope and its Application to Study Scratch Resistance of Ultra-thin Hard Amorphous Carbon Coatings”, *Journal of Materials Research* **16**, 437-445.

5. Sundararajan, S. and Bhushan, B. (2000), "Topography-Induced Contributions to Friction Forces Measured Using an Atomic Force/Friction Force Microscope", *Journal of Applied Physics* **88**, 4825-4831.
6. Sundararajan, S. and Bhushan, B. (1999), "Micro/Nanotribology of Ultra-Thin Hard Amorphous Carbon Coatings using Atomic Force/Friction Force Microscopy", *Wear* **225-229**, 678-689.
7. Sundararajan, S. and Bhushan, B. (1998), "Micro/Nanotribological Studies of Polysilicon and SiC Films for MEMS Applications", *Wear* **217**, 251-261.
8. Bhushan, B., Sundararajan, S., Li, X., Zorman, C.A. and Mehregany, M. (1998), "Micro/Nanotribological Studies of Single-Crystal Silicon and Polysilicon and SiC Films for Use in MEMS Devices", in *Tribology Issues and Opportunities in MEMS*, edited by B. Bhushan, Kluwer Academic Publishers, Dordrecht, Netherlands, 407-430.
9. Bhushan, B. and Sundararajan, S. (1998), "Micro/Nanoscale Friction and Wear Mechanisms of Thin Films Using Atomic Force and Friction Force Microscopy", *Acta Mater.* **46**, 3793-3804.
10. Bhushan, B., Sundararajan, S., Scott, W.W. and Chilamakuri, S. (1997), "Stiction Analysis of Magnetic Tapes", *IEEE Trans. Magn.* **33** (5), 3211-3213.

FIELDS OF STUDY

Major field: Mechanical Engineering

TABLE OF CONTENTS

	<u>Page</u>
Abstract.....	ii
Dedication.....	iv
Acknowledgments.....	v
Vita.....	viii
List of Tables	xiii
List of Figures	xiv
Chapters:	
1. Introduction.....	1
1.1 Microelectromechanical Systems (MEMS).....	1
1.1.1 Fabrication techniques for MEMS.....	3
1.1.2 Some applications of MEMS	5
1.2 Critical issues affecting MEMS reliability and widespread commercialization...6	
1.2.1 Tribological Issues.....	6
1.2.2 Mechanical property issues	12
1.3 Micro/nanotribology and the Atomic Force Microscope (AFM).....	15
1.4 Objectives of Research and Overview of Research Efforts.....	16
2. Topography-induced contributions to friction forces measured using an atomic force/friction force microscope.....	19
2.1 Introduction and Literature Review.....	19
2.2 Experimental	21
2.3 Results and Discussion	21
2.4 Summary	32
3. Static friction and surface roughness studies of surface micromachined electrostatic micromotors.....	33
3.1 Introduction and Literature Review.....	33
3.2 Micromotor Samples and Lubricants	36

3.2.1	Polysilicon electrostatic micromotors.....	36
3.2.2	Lubricants and lubrication of micromotors.....	38
3.3	Technique to Measure Static Friction Force of the Micromotor.....	40
3.4	Results and Discussion	44
3.4.1	Static friction force measurements	44
3.4.2	Effect of rest time and humidity.....	46
3.4.3	Surface roughness measurements.....	47
3.4.4	Discussion	51
4.	Micro/Nanotribological Studies of Ultra-Thin Hard Amorphous Carbon Coatings for Scratch and Wear Resistance	54
4.1	Introduction	54
4.2	DLC coating samples.....	55
4.3	Experimental techniques.....	58
4.3.1	Scratch and wear tests using multiple cycles	59
4.3.2	Development of a continuous microscratch technique to study scratch resistance using an AFM.	61
4.3.2.1	Generation of a scratch at increasing normal load	61
4.3.2.2	Measuring friction force during scratching.....	62
4.3.2.3	Effect of detector cross talk and topography on measured friction signal.....	63
4.4	Results and discussion	65
4.4.1	Scratch and wear tests using multiple cycles	65
4.4.1.1	Coating failure mechanisms	70
4.4.2	Continuous microscratch tests.....	76
4.4.2.1	Coating failure mechanisms	84
4.4.3	Surface analysis of coatings	84
4.5	Summary	88
5.	Mechanical Properties of Nanoscale Structures.....	90
5.1	Introduction and literature review	90
5.2	Experimental Procedure.....	93
5.2.1	Fabrication of nanometer-scale specimens	93
5.2.2	Nanometer-scale bending test using an AFM	96
5.2.3	Determination of elastic modulus and bending strength.....	99
5.2.4	Finite element model	101
5.2.5	Method to estimate nanoscale fracture toughness	102
5.2.6	Fatigue experiments of nanobeams	106
5.3	Results and Discussion	106
5.3.1	Elastic modulus and bending strength	106

5.3.2	Fracture toughness	114
5.3.3	Fatigue.....	117
5.3.4	SEM observations of fracture surfaces	120
5.4	Summary	122
6.	Conclusions	123
6.1	Topography-induced contributions to friction forces measured using an AFM.....	123
6.2	Static friction in micromotors	124
6.3	Scratch/wear resistance of ultra-thin DLC coatings	125
6.4	Mechanical properties of nanoscale structures	125
Appendices		
A.	Description of Atomic Force/Friction Force Microscope, Tips and Techniques....	127
A.1	Description of AFMs	127
A.2	Friction measurements	130
A.3	Scratch/wear experiments at constant load	132
A.4	Tips used in AFM/FFM studies.....	133
B.	Macros for Controlled Tip Movement for Various AFM Experiments.....	135
B.1	Continuous microscratch experiment.....	135
B.2	Quasi-static bending of nanobeams	136
B.3	Monotonic-cyclic loading of nanobeams	137
C.	Surface Roughness Parameters.....	139
Bibliography		143

LIST OF TABLES

<u>Table</u>		<u>Page</u>
3.1	Data in the literature on coefficient of static friction measurements of MEMS devices and structures.....	34
3.2	Surface roughness parameters and microscale coefficient of friction for various micromotor component surfaces measured using an AFM. Mean and $\pm 1\sigma$ values are given.	48
4.1	List of coatings studied and their selected parameters.	56
4.2	Hardness, elastic modulus and fracture toughness of various 100 nm thick coatings.	57
5.1	Dimensions of nanobeams used in this study.	96
5.2	Material properties used for finite element model	102
5.3	Fracture stresses for experiments to estimate K_{IC}	115
5.4	Summary of measured parameters from quasi-static bending tests.	116
5.5	Summary of fatigue test data	117

LIST OF FIGURES

<u>Figure</u>	<u>Page</u>
1.1	SEM micrographs demonstrating the scale and complexity of MEMS devices. 2
1.2	Schematics of process steps involved in bulk micromachining and surface micromachining fabrication of MEMS..... 4
1.3	Schematic of process steps involved in LIGA. 4
1.4	(a) Examples of microstructures exhibiting stiction; from left to right; micromachined polysilicon cantilever beams; microengine with one of the fingers in the driving comb collapsed; suspended polysilicon plates (from Bhushan, 1998). (b) Wear of gear and flange (left) and a hub of a microgear train (Sandia Labs, 1990) 7
1.5	Examples of MEMS devices and components that may experience tribological problems 8
1.6	Examples of MEMS devices having commercial use that can experience tribological problems 10
1.7	Summary of tribological issues in MEMS device operation and fabrication 13
1.8	Examples of MEMS devices consisting of structures that vibrate at high frequencies. In such applications, fatigue strength is a critical factor affecting reliability. 14
1.9	Outline of research efforts 17
2.1	Typical friction loop representing friction forces between the AFM tip and sample in the forward (Trace) and backward (Retrace) scanning directions. Note that the sign of the friction forces for the Retrace portion is reversed with respect to the Trace portion due to the reversal of the torque applied to the end of the tip when the scanning direction is reversed..... 20
2.2	2D profiles of surface height, friction force (loop) and subtracted friction force across a silicon grid pit obtained using a Dimension 3000 AFM (left) and Multimode AFM (right)..... 23

2.3	Grayscale images and representative 2D profile of surface height and friction forces of a gold ruler. Note that subtracting the friction force data (T-R) does not eliminate topography-induced effects.....	24
2.4	(a) Grayscale images and 2D profiles of surface height and friction forces and (b) grayscale images and 2D profiles of surface slope (dz/dx) across a single ruling of the gold ruler.....	26
2.5	Schematic of friction forces expected when a tip traverses a sample that is composed of different materials and sharp changes in topography. A schematic of surface slope is also shown.....	30
2.6	(a) 2D profiles of surface height, surface slope and friction force for a scan across the silicon grid pit	31
3.1	One of the first electrostatically actuated polysilicon micromotors (Tai et al., 1989).	34
3.2	Optical micrograph of a typical surface micromachined polysilicon micromotor used in this study	36
3.3	(a) Fabrication process sequence of surface micromachined polysilicon micromotors. (b) Dimensions of the micromotor; the clearance between the rotor and the hub is about 250 nm. The figures are not to scale.....	37
3.4	Friction force as a function of number of cycles using an Si_3N_4 tip at 300 nN normal load for unlubricated and PFPE-lubricated silicon samples (Koinkar and Bhushan, 1996a).....	40
3.5	(a) Schematic of the technique used to measure the force, F_s , required to initiate rotor movement using an AFM/FFM. (b) As the tip is pushed against the rotor, the lateral deflection experienced by the rotor due to the twisting of the tip prior to rotor movement is a measure of static friction force, F_s , of the rotors. (c) Schematic of lateral deflection expected from the above experiment. The peak V_f is related to the static friction of the motor. (d) Raw lateral deflection and normal deflection data obtained using an AFM (Si_3N_4 tip) against a rotor.....	42
3.6	(a) Static friction force data (raw and normalized with the weight of the rotor) for unlubricated and lubricated micromotors. The solid points indicate the force obtained in the first experiment for a given rotor, while the open points indicate values obtained on subsequent runs. Motors M1 – M4 and M6 – M8 are from Batch 1 and M5 is from the Batch 2. (b) Normalized static friction force data for selected micromotors as a function of rest time and relative humidity. Rest time is defined as the time elapsed between a given experiment and the first experiment in which motor movement was recorded (time 0). The motors were allowed to sit at a particular humidity for 12 hours prior to measurements.	45

3.7	Representative AFM surface height images obtained in tapping mode (5 μm x 5 μm scan size) of various component surfaces of the micromotors (Images shown are that of motor M1). RMS roughness (σ) and peak-to-valley (P-V) values of the surfaces are given. The underside of the rotor exhibits drastically different topography from the top side.	49
3.8	Surface height images of polysilicon regions directly below the rotor (for motor M1). Region A is away from the rotor while region B was initially covered by the rotor prior to the release etch of the rotor. During this step, slight rotation of the rotor caused region B to be exposed.	50
3.9	Summary of effect of liquid and solid lubricants on static friction force of micromotors. Despite the hydrophobicity of the lubricant used (Z-DOL), a mobile liquid lubricant (Z-DOL as is) leads to very high static friction force due to increased meniscus forces whereas a solid-like lubricant (bonded Z-DOL) appears to provide some amount of reduction in static friction force.	52
4.1	(a) An example of scratch depths obtained on uncoated Si(100) during the course of the scratch tests, illustrating the effect of blunting of the diamond tip. (b) Magnitudes of the scaling factors used for the scratch data.	60
4.2	Schematic of continuous microscratch technique implemented in a commercial atomic force/friction force microscope (AFM/FFM).	62
4.3	(a) Coupling effect between vertical (normal) and lateral deflection (friction) signals and (b) effect of topography on friction signal on Si(100). Both effects are negligible in this study.	64
4.4	Scratch data of the coatings (a) grouped by deposition technique and (b) by coating thickness. FCA – Filtered Cathodic Arc, IB – Ion Beam, ECR-CVD – Electron Cyclotron Resonance Chemical Vapor Deposition, SP – Sputtered.	66
4.5	AFM 3D images of scratches on FCA and SP coatings	68
4.6	(a) Wear data on Si(100).....	68
	(b) Wear data for all DLC coatings.	69
4.7	(a) AFM 3D image of a wear mark on Si(100).....	70
	(b) AFM 3D images of wear marks for all 10 nm coatings and (c) for all FCA coatings. The arrows indicate regions of sudden failure.	71
4.8	2D Surface height and corresponding friction force maps of FCA and SP 10 nm coatings during wear showing the failure process. Brighter regions correspond to higher surface height and higher friction force in the surface height and friction force images, respectively.	73

4.9	Schematics illustrating (a) the suggested failure mechanism of FCA, IB and ECR-CVD coatings at thicknesses of 5 to 20 nm (b) the difference in load-carrying capacities between thick and thin coatings and (c) the suggested failure mechanism of 3.5 nm coatings.....	74
4.10	(a) Applied normal load and friction signal measured during a continuous microscratch experiment on Si(100) as a function of scratch distance. (b) Friction data averaged for a given normal load and plotted in the form of coefficient of friction as a function of normal load and (c) AFM surface height image of scratch obtained in tapping mode.....	77
4.11	Coefficient of friction profiles during scratch as a function of normal load and corresponding AFM surface height images for (a) FCA, (b) ECR-CVD and (c) SP coatings	79
4.12	(a) Critical loads estimated from the coefficient of friction profiles and AFM images for the various coatings. (b) Critical loads estimated from continuous scratch tests using a Nanoindenter for the various coatings	82
4.13	Normal loads at which the residual depth of the scratches as measured using the AFM first exceeds the coating thickness for the various coatings.....	83
4.14	Variation of observed critical loads as a function of (a) coating hardness and (b) fracture toughness.....	85
4.15	Quantified XPS data for all the coatings. Atomic concentrations are shown.....	86
4.16	(a) XPS spectra for FCA and SP coatings at 5 nm and 20 nm coating thicknesses and (b) AES spectra for FCA and SP coatings at 5 nm thickness.....	87
5.1	Techniques developed by other researchers to measure elastic modulus, fracture strength and fracture toughness of microscale specimens	91
5.2	Schematic of fabrication process of nanoscale silicon beams. SiO ₂ beams are fabricated from the silicon beams by thermal oxidation as indicated in the final step.....	94
5.3	(a) SEM micrographs of nanobeam specimens and (b) a schematic of the shape of a typical nanobeam. The trapezoidal cross-section is due to the anisotropic wet etching during the fabrication. Typical dimensions are given in Table 5.1.....	95
5.4	(a) Schematic of experiment to determine sensitivity of the photodetector for a diamond tip setup in the AFM. (b) The sensitivity is used in determining cantilever deflection in the nanoscale bending test technique. The AFM tip is brought to the center of the nanobeam and the piezo is extended over a known distance. By measuring the tip displacement, a load displacement curve of the nanobeam can be obtained.....	98

5.5	A schematic of the bending moments generated in the beam during a quasi-static bending experiment, with the load at the center of the span. The maximum moments occur under the load and at the fixed ends. Due to the trapezoidal cross section, the maximum tensile bending stresses occur at the top surfaces at the fixed ends.	100
5.6	(a) A comparison of load displacement curves of a nanobeam obtained from an AFM experiment and using the finite element model. The curves show good correlation indicating that the model can be confidently used to estimate stresses in the beams. (b) Bending stress distribution indicating that the maximum tensile stresses occur on the top surfaces near the fixed ends.	103
5.7	(a) Schematic of technique to generate a defect (crack) of known dimensions in order to estimate fracture toughness. A diamond tip is used to generate a scratch across the width of the beam. When the beam is loaded as shown, a stress concentration is formed at the bottom of the scratch. The fracture load is then used to evaluate the stresses using FEM. (b) AFM 3-D image and 2-D profile of a typical scratch. (c) Finite element model results verifying that the maximum bending stress occurs at the bottom of the scratch.	104
5.8	Schematic of crack tip and coordinate systems used in Equation 5.9 to describe a stress field around the crack tip in terms of the stress intensity parameter, K_I	105
5.9	(a) Schematic showing the details of the technique to study fatigue behavior of the nanobeams. The diamond tip is located at the middle of the span and a cyclic load at 4.2 Hz is applied to the beam by forcing the piezo to move in the pattern shown. An extension is made every 300 s to compensate for the piezo drift to ensure that the load on the beam is kept fairly constant. (b) Data from a fatigue experiment on a nanobeam until failure. The normal load is computed from the raw vertical deflection signal. The compensations for piezo drift keep the load fairly constant.	107
5.10	Typical load displacement curves of silicon and SiO ₂ nanobeams. The curves are linear until sudden failure, indicative of brittle fracture of the beams. The elastic modulus (E) values calculated from the curves are shown.	108
5.11	Elastic modulus values measured for Si and SiO ₂ . The average values are shown. These are comparable to bulk values, which shows that elastic modulus shows no specimen size dependence.	109
5.12	SEM micrographs of nanobeams that failed during quasi-static bending experiments. The beams failed at or near the ends, which is the location of maximum tensile bending stress.	110

5.13	Bending strength values obtained from bending experiments. Average values are indicated. These values are much higher than values reported for microscale specimens, indicating that bending strength shows a specimen size effect.....	111
5.14	Weibull analysis of bending strength data. (a) Both Si and SiO ₂ data fit a 2-parameter Weibull distribution as shown. The slopes of the fitted lines give the Weibull moduli. (b) Failure probability plotted as a function of bending strength (fracture stress).	113
5.15	Values of fracture toughness (K_{IC}) calculated from Eq. 5.9 for increasing values of r corresponding to distance between neighboring atoms in {111} planes in silicon (0.4 nm). Hence r -values between 0.4 and 1.6 nm are chosen. The K_{IC} values thus estimated are comparable to values reported by others for both Si and SiO ₂	115
5.16	(a) Optical micrographs with arrows indicating beams failed under cyclic (fatigue) loading. During fatigue, failure of the beam occurs under the point of loading (near the center of the span) or at the beam-ends. (b) SEM micrograph showing a close up of failure locations under quasi-static bending and fatigue	118
5.17	Fatigue test data showing applied bending stress as a function of number of cycles; nanoscale SN curves.	119
5.18	Fracture surfaces of silicon and SiO ₂ beams subjected to (a) quasi-static bending and (b) fatigue.....	121
A.1	The small sample MultiMode AFM (left) and the large sample Dimension 3000 AFM (right) from Digital Instruments.	127
A.2	Schematics of operation of (a) small sample AFM and (b) large sample AFM.....	128
A.3	Schematic of ‘height’ mode operation of an AFM to obtain surface topography	129
A.4	Friction calibration data obtained on Al ₂ O ₃ . (a) Three data sets of Trace minus Retrace (TMR) value of surface height as a function of normal load. The slope of this plot δ , is related to the coefficient of friction μ between sample and tip. (b) Two data sets of true friction signal as a function of normal load. Equating the slope of this plot to μ obtained from (a), the conversion factor to convert lateral deflection signal to friction force can be obtained.....	131
A.5	Schematics of micro/nanoscale scratch and wear tests conducted using an AFM.....	132
A.6	Tips used in AFM/FFM	134

A.7	Schematic of diamond tip-cantilever assembly mounted in an AFM cantilever holder. The cantilever sits in the machined groove. The thin aluminum plate and spring clip provide rigid clamping of the cantilever. The cantilever length L can be varied	134
C.1	Surface roughness of solid surfaces	140
C.2	Surface height distributions with different values of skewness and kurtosis. Most surfaces have a Gaussian distribution of surface heights, with skewness of 0 and kurtosis of 3	141
C.3	Examples of surface profiles with different values of skewness and kurtosis.....	142

CHAPTER 1

INTRODUCTION

1.1 Microelectromechanical Systems (MEMS)

Microelectromechanical systems (MEMS) is the collective term for microcomponents and microdevices that have been developed using lithography-based and other techniques with physical dimensions ranging from a couple to a few thousand microns. While most of the work in the first several years consisted of fabrication and laboratory demonstration of such devices, the field of MEMS has grown considerably over the last decade and includes several industrial applications such as accelerometers in air-bag deployment in automobiles and actuators for magnetic heads in rigid-disk drives (for an early review, see Peterson, 1982; for recent reviews, see Muller et al., 1990; Madou, 1997; Trimmer, 1997; Bhushan, 1998; Kovacs, 1998). Figure 1.1 shows some examples of the scale and complexity of MEMS devices. The field of MEMS has received increased attention over the last few years and various industry and government scribes have been predicting the ‘imminent broad-based impact of MEMS technology in society’ suggesting that MEMS devices should by now be as common as the personal computer.

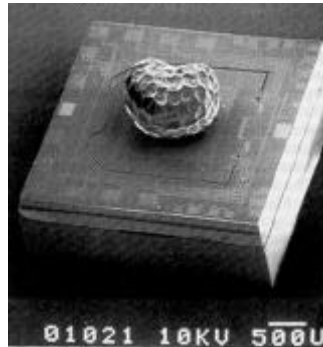
Despite the increasing popularity of MEMS in research and industry, these devices experience severe tribological (friction and wear) and other problems that undermine their performance and reliability. In fact, several studies have shown that tribology and mechanics of MEMS appear to be the limiting factors to the imminent broad-based impact of MEMS in our everyday lives (Komvopoulos, 1996; Maboudian

and Howe, 1997; Bhushan, 1998). These issues could also potentially hinder the arrival of nanotechnology-based products, which is the newest research area receiving a lot of attention. These facts provide the motivation for this research, which is aimed at developing a better understanding of tribological and mechanical issues pertaining to MEMS on a pertinent scale, that is, the micro/nanoscale.

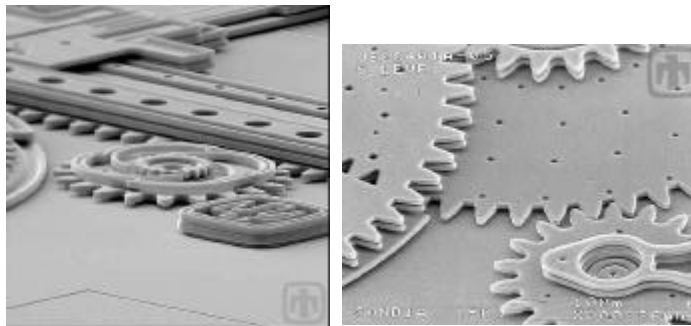
The remainder of this chapter consists of a brief overview of the fabrication techniques for MEMS and examples of MEMS devices, followed by a description of the tribological and mechanics-related issues that affect the reliable operation of such devices. This is followed by the research objectives and a brief overview of the various studies comprising the research effort that are presented in this dissertation.



An ant and a gear
(Forschungszentrum
Karlsruhe, GmbH, Germany)



Silicon cantilever
accelerometer chip
with a poppy seed
placed on the seismic
mass (Trimmer, 1997)



(Left) An anti-reverse mechanism in a rack and pinion system
and (right) close-up of a gear train (Sandia National Labs, 1990)

Figure 1.1: SEM micrographs demonstrating the scale and complexity of MEMS devices.

1.1.1 Fabrication techniques for MEMS

The three most common fabrication techniques for MEMS devices are: bulk micromachining, surface micromachining, and LIGA (a German acronym for Lithographie Galvanoformung Abformung), a German term for lithography, electroforming, and plastic molding. The first two approaches, bulk and surface micromachining, use planar photolithographic fabrication processes developed for semiconductor devices in producing two-dimensional (2D) structures (Jaeger, 1988; Madou, 1997). The various steps involved in these two fabrication processes are shown schematically in Fig. 1.2. Bulk micromachining employs anisotropic etching to remove sections through the thickness of a single-crystal silicon wafer, typically 250 to 500 μm thick. Bulk micromachining is a proven high-volume production process and is routinely used to fabricate microstructures such as acceleration and pressure sensors and magnetic head sliders. Surface micromachining is based on deposition and etching of structural and sacrificial films to produce a freestanding structure. These films are typically made of low-pressure chemical vapor deposition (LPCVD) polysilicon film with 2 to 20 μm thickness. Surface micromachining is used to produce complex micromechanical devices such as motors, gears, and grippers.

The LIGA process is based on the combined use of X-ray lithography, electroforming, and molding processes. The steps involved in the LIGA process are shown schematically in Fig. 1.3. LIGA is used to produce high-aspect ratio (HAR) MEMS devices that are up to 1 mm in height and only a few microns in width or length (Becker et al., 1986). The LIGA process yields very sturdy 3D structures due to their increased thickness. One of the limitations of silicon microfabrication processes originally used for fabrication of MEMS devices is the lack of suitable materials that can be processed. With LIGA, a variety of non-silicon materials such as metals, ceramics and polymers can be processed. Non-lithographic micromachining processes, primarily in Europe and Japan, are also being used for fabrication of millimeter-scale devices using direct material microcutting or micromechanical machining (such as micromilling, microdrilling, microturning) or removal by energy beams (such as microspark erosion, focused ion beam, laser ablation, and machining, and laser polymerization) (Madou,

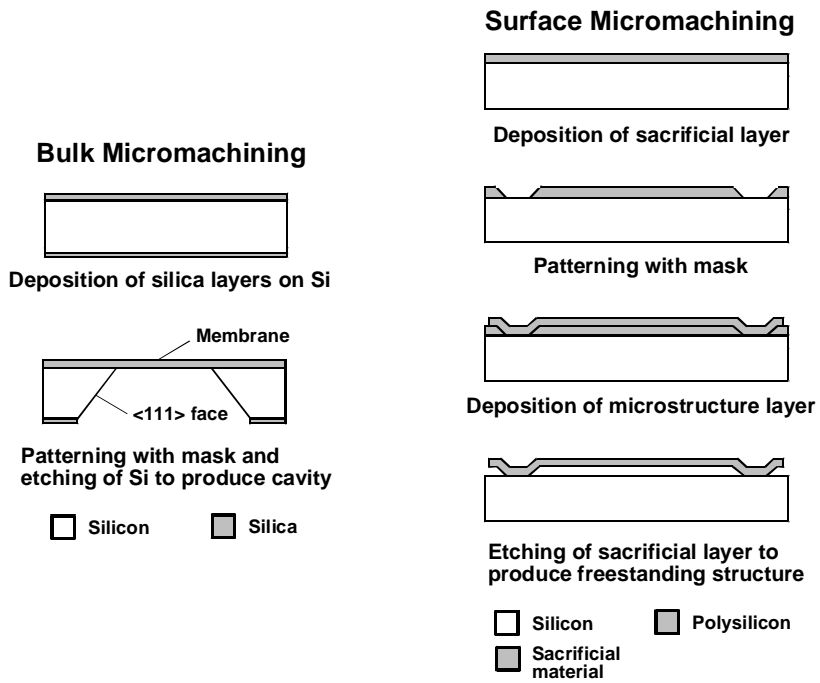


Figure 1.2: Schematics of process steps involved in bulk micromachining and surface micromachining fabrication of MEMS.

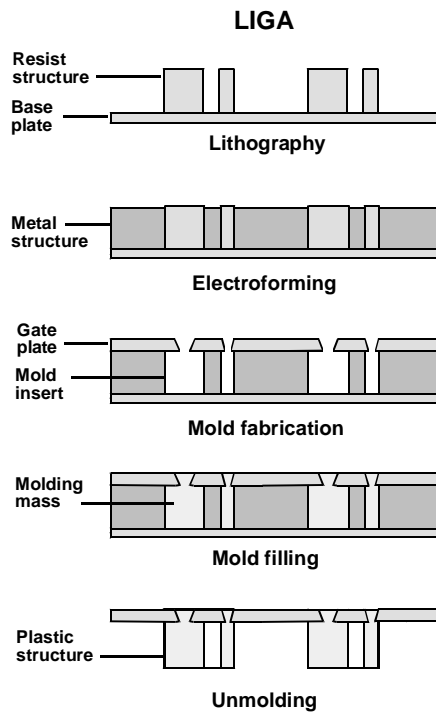


Figure 1.3: Schematic of process steps involved in LIGA.

1997; Friedrich and Warrington, 1998). Hybrid technologies including LIGA and high-precision micromachining techniques have been used to produce miniaturized motors, gears, actuators, and connectors (Lehr et al., 1996, 1997; Michel and Ehrfeld, 1998). These millimeter-scale devices may find more immediate applications.

1.1.2 Some applications of MEMS

MEMS devices have begun to be commercially used, particularly in the automotive industry. Silicon-based high-G acceleration sensors are used in airbag deployment (Core et al., 1993; Bryzek et al., 1994). Acceleration sensor technology is slightly less than a billion-dollar-a-year industry dominated by Lucas NovaSensor and Analog Devices. The digital micromirror devices (DMD) provided by Texas Instruments are large-scale integrated spatial light modulators (Hornbeck and Nelson, 1988; Hornbeck, 1999). These use deformable mirror arrays on microflexures as part of airline-ticket laser printers and high-resolution projection devices. MEMS devices are also being pursued in magnetic storage systems (Bhushan, 1996), where they are being developed for super compact and ultrahigh-recording-density magnetic disk drives. Several integrated head/suspension microdevices have been fabricated for contact recording applications (Hamilton, 1991; Ohwe et al., 1993). High-bandwidth servo-controlled microactuators have been fabricated for ultrahigh-track-density applications which serve as the fine-position control element of a two-stage, coarse/fine servo system, coupled with a conventional actuator (Miu and Tai, 1995; Fan et al., 1995; Horsley et al., 1998). Millimeter-sized wobble motors and actuators for tip-based recording schemes have also been fabricated (Fan and Woodman, 1995). Other potential applications of MEMS devices include silicon-based acceleration sensors for anti-skid braking systems and four-wheel drives, silicon-based pressure sensors for monitoring pressure of cylinders in automotive engines and of automotive tires, and various sensors, actuators, motors, pumps, and switches in medical instrumentation, cockpit instrumentation, and many hydraulic, pneumatic, and other consumer products (Fujimasa, 1996; Kovacs, 1998).

The advantages of MEMS are (a) they are inexpensive to produce since they are based on existing production infrastructure, that is, semiconductor-processing technology and can therefore be batch-fabricated; (b) they can be easily integrated into multi-functional systems since their fabrication is semiconductor-technology based and (c) the portability and/or low power consumption associated with their miniature size.

1.2 Critical issues affecting MEMS reliability and widespread commercialization

Despite the above advantages, there are issues that undermine their reliability which are still to be successfully dealt with. The most critical is that of tribology, which is the study of phenomena associated with friction and wear at all levels of technology where the rubbing of surfaces are involved. Also, there is an issue with mechanical properties on the scale of MEMS; are these the same as for bulk materials evaluated at larger scales?

1.2.1 Tribological Issues

In MEMS devices, various forces associated with the device scale down with the size. When the length of the machine decreases from 1 mm to 1 μm , the surface area decreases by a factor of million while the volume decreases by a factor of a billion. As a result, surface forces such as friction, adhesion, meniscus forces, viscous drag and surface tension that are proportional to area, become a thousand times larger than the forces proportional to the volume, such as inertial and electromagnetic forces. Since the start-up forces and torques involved in MEMS operation available to overcome retarding forces are small, the increase in resistive forces such as friction and adhesion become serious tribological concerns that limit the life and reliability of MEMS devices (Komvopoulos, 1996; Maboudian and Howe, 1997; Bhushan, 1998).

In addition to the consequence of a large surface-to-volume ratio, since MEMS devices are designed for small tolerances, physical contact becomes more likely, which makes them particularly vulnerable to adhesion between adjacent components. A large lateral force required to initiate relative motion between two smooth surfaces is referred

to as “stiction” or static friction, which has been studied extensively in tribology of magnetic storage systems (Bhushan, 1996). Stiction problems are extremely prevalent in MEMS from the fabrication stage to the operation and are a major cause for extremely low reliability of devices (Mastrangelo, 1997). Figure 1.4(a) shows examples of stuck or collapsed MEMS structures as a result of stiction. Friction/stiction (static friction), wear and surface contamination affect device performance and in some cases, can even prevent devices from working. Figure 1.4(b) shows examples of the damage that can be caused as result of wear in such devices.

Figure 1.5 shows examples of several MEMS devices that can encounter the above-mentioned tribological problems. The polysilicon electrostatic micromotor has 12 stators and a 4-pole rotor and is produced by surface micromachining. The rotor diameter is 120 μm and the air gap between the rotor and stator is 2 μm (Tai et al., 1989). It is capable of continuous rotation up to speeds of 100,000 rpm. The intermittent contact

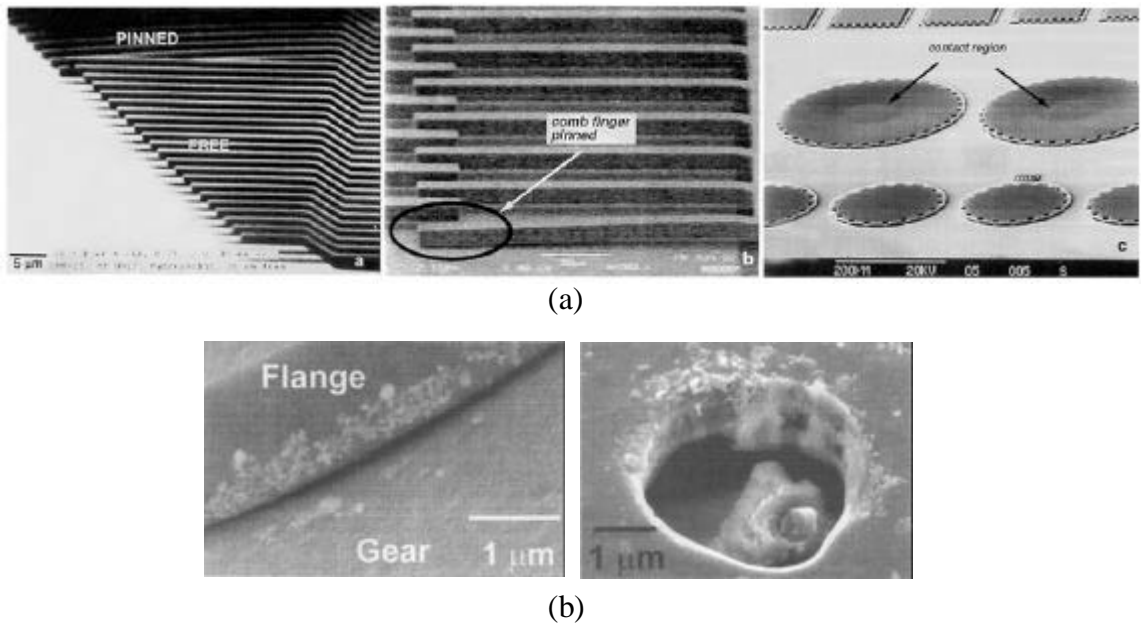


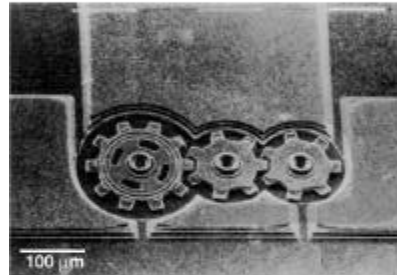
Figure 1.4: (a) Examples of microstructures exhibiting stiction; from left to right; micromachined polysilicon cantilever beams; microengine with one of the fingers in the driving comb collapsed; suspended polysilicon plates (Bhushan, 1998). (b) Wear of gear and flange (left) and a hub of a microgear train (Sandia Labs, 1990).



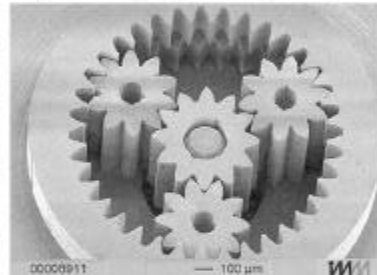
Electrostatic micromotor
(Tai et al., 1989)



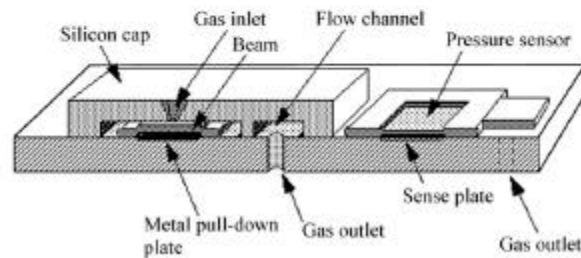
Partially released pair of tongs
(Mehregany et al., 1988)



Gear train in an air microturbine
(Mehregany et al., 1988)



Ni-Fe wolfram-type gear system
by LIGA (Lehr et al., 1996)

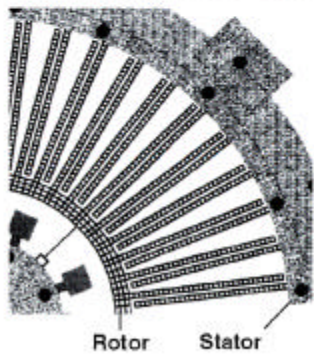
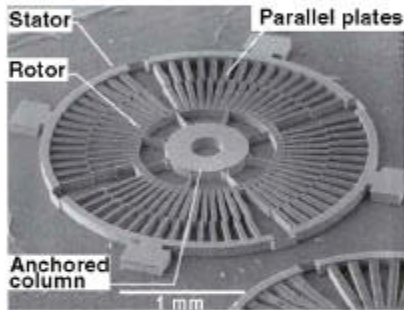
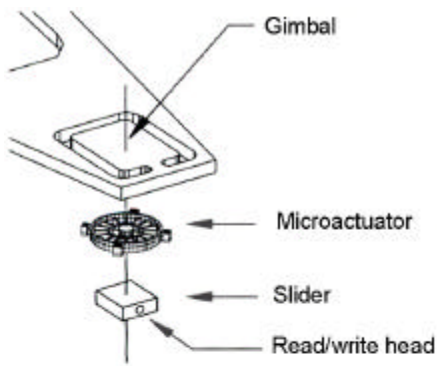


Low-pressure flow modulator with electrostatically actuated microvalves (Robertson and Wise, 1998)

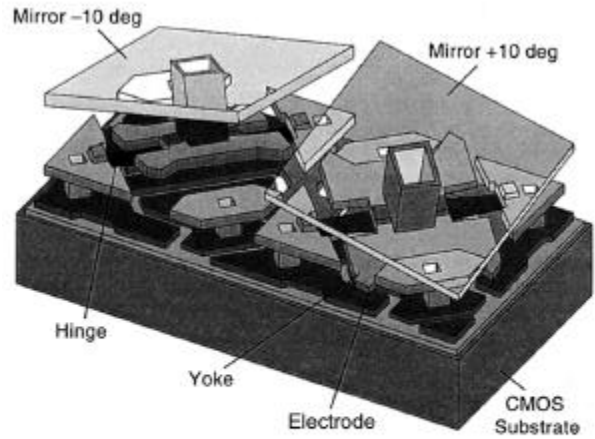
Figure 1.5: Examples of MEMS devices and components that may experience tribological problems.

at the rotor-stator interface and physical contact at the rotor-hub flange interface result in wear issues (Fig. 1.4b). In addition to wear problems, stiction between the contacting surfaces limits the repeatability of operation or may even prevent the operation altogether. Figure 1.5 also shows an SEM micrograph of a pair of tongs (Mehregany et al., 1988). The jaws open when the linearly sliding handle is pushed forward, demonstrating linear-to-rotary motion conversion. For this pair of tongs, the jaws open up to 400 μm in width. Wear at the gear teeth and end of the jaws is of concern. A surface micromachined polysilicon gear train for an air turbine is shown with gear or blade rotors, 125 to 240 μm in diameter (Mehregany et al., 1988). The two flow channels on the top are connected to the two independent input ports and the two flow channels at the bottom are connected to the output port of an air turbine. As an example of non-silicon components, a milligear system produced using the LIGA process for a DC brushless permanent magnet millimotor (diameter = 1.9 mm, length = 5.5 mm) with an integrated milligear box (Lehr et al., 1996, 1997; Michel and Ehrfeld, 1998) is also shown. The gears are made of metal (electroplated Ni-Fe) but can also be made from injected polymer materials (e.g., POM) using the LIGA process. Wear at the contact of gear teeth is a concern. In the micromachined flow modulator, eight micromachined flow channels are integrated in series with eight electrostatically actuated microvalves (Robertson and Wise, 1998). The flow channels lead to a central gas outlet hole drilled in the glass substrate. Gas enters the device through a bulk micromachined gas inlet hole in the silicon cap. The gas, after passing through an open microvalve, flows parallel to the glass substrate through flow channels and exits the device through an outlet. The normally open valve structure consists of a freestanding double-end-clamped beam, which is positioned beneath the gas inlet orifice. When electrostatically deflected upwards, the beam seals against inlet orifice and the valve is closed. In these microvalves used for flow control, the mating valve surfaces should be smooth enough to seal while maintaining a minimum roughness to ensure low friction/stiction (Komvopoulos, 1994; Bhushan, 1999b). Stiction is a major issue.

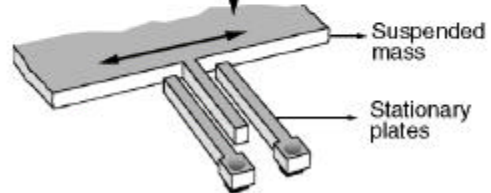
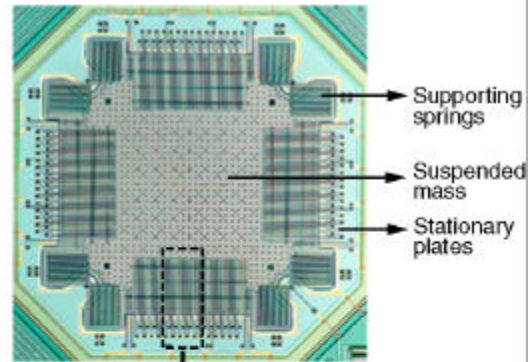
Commercially available MEMS devices may exhibit tribological problems as well. Figure 1.6 shows a digital micromirror device (DMD) pixel for xerographic type



Polysilicon rotary microactuator for magnetic disk drives (Horsley et al., 1998)



Digital micromirror device for displays (Hornbeck, 1999)



Capacitive type silicon accelerometer for automotive sensory applications (Sulouff, 1998)

Figure 1.6: Examples of MEMS devices having commercial use that can experience tribological problems.

printers and digital projection displays (Hornbeck, 1999). It consists of an array of rotatable aluminum mirrors fabricated on top of a CMOS static random access memory integrated circuit. The surface micromachined array consist of a half of a million to a million or more of these independently controlled reflective, digital light switches. The electrostatically activated pixel strikes the electrode surface with a certain amount of energy. The pixel operated in a bistable mode where the equilibrium positions occur when the yoke with the mirror is rotated $\pm 10^\circ$ (with respect to the horizontal plane) into contact with the electrode surface. Contact between the yoke and the electrode surface is required for true digital (binary) operation. Stiction and wear during these contacts are the issues affecting the reliable operation of the micromirror device (Henck, 1997). An electrostatically driven, surface-micromachined rotary microactuator for a magnetic disk drive is shown in Fig. 1.6 (Horsley et al., 1998). This high-bandwidth servo-controlled microactuator is being developed for ultrahigh-track-density applications, which serves as the fine-position control element of a two-stage, coarse/fine servo system when coupled with a conventional actuator (Miu and Tai, 1995; Fan et al., 1995; Horsley et al., 1998). Actuation is accomplished via capacitive parallel plates, which are alternately attached to the rotor and stator in to form pairs as shown in Fig. 1.6. A voltage applied across these plates results in an electrostatic force, which rotates the central rotor. Any unintended contacts between the rotor and stator plates may result in wear and stiction. Also shown in Fig. 1.6 is a surface micromachined integrated capacitive silicon accelerometer fabricated by Analog Devices, which is used for automotive sensory applications (Core et al., 1993; Sulouff, 1998; for more information on Analog Devices, visit www.analog.com). The central suspended beam mass is supported on the four corners by spring structures. The central beam has interdigitated plates on the four sides that alternate with those of the stationary plates as shown. Motion of the central beam causes a change in the capacitance between these plates, which is used to measure the acceleration. Here stiction of the beam structure with the underlying substrate as well as stiction between the adjacent plates (fingers) are detrimental to the operation of the sensor (Core et al., 1993; Sulouff, 1998). Wear during unintended contacts of these plates is also a problem.

Friction/stiction and wear clearly limit the lifetimes and compromise the performance and reliability of microdevices. Figure 1.7 summarizes some of the various tribological problems encountered in various MEMS devices and components just discussed.

In addition, there are tribological issues in the fabrication processes that are also being addressed. For example, in surface micromachining, the suspended structures can sometimes collapse and permanently adhere to the underlying substrate due to meniscus effects during the final rinse and dry process as shown in Fig. 1.7 (Guckel and Burns, 1989). The mechanism of such adhesion phenomena needs to be understood (Mastrangelo and Hsu, 1993; Maboudian and Howe, 1997).

It is clear that tribology is an important factor affecting the performance and reliability of MEMS devices. There is a need to develop a fundamental understanding of friction/stiction, wear phenomena on the scale pertinent to MEMS and to understand the role of surface contamination and environment in microdevices. Another requirement is to develop lubricants and identify lubrication methods that are suitable for MEMS. Component-level studies are required to provide a better understanding of the tribological phenomena occurring in MEMS.

1.2.2 Mechanical property issues

It is essential for designers of MEMS to have mechanical property information on the nanoscale, as most mechanical properties are known to exhibit a dependence on specimen size (Gane and Cox, 1970; Sargent, 1986; Bhushan et al., 1996). Mechanical property evaluation of nanometer-scale structures is therefore necessary to help design reliable MEMS/NEMS since good mechanical properties are of critical importance in such applications.

Properties such as elastic modulus, hardness, fracture toughness and breaking strength affect the load/stress levels that devices can withstand. For MEMS application such as high-frequency oscillators and resonators (Nguyen and Howe, 1999), which consist of beam-like structures that vibrate at frequencies on the order of several hundred megahertz to several hundred gigahertz, fatigue properties are also important. Figure 1.8

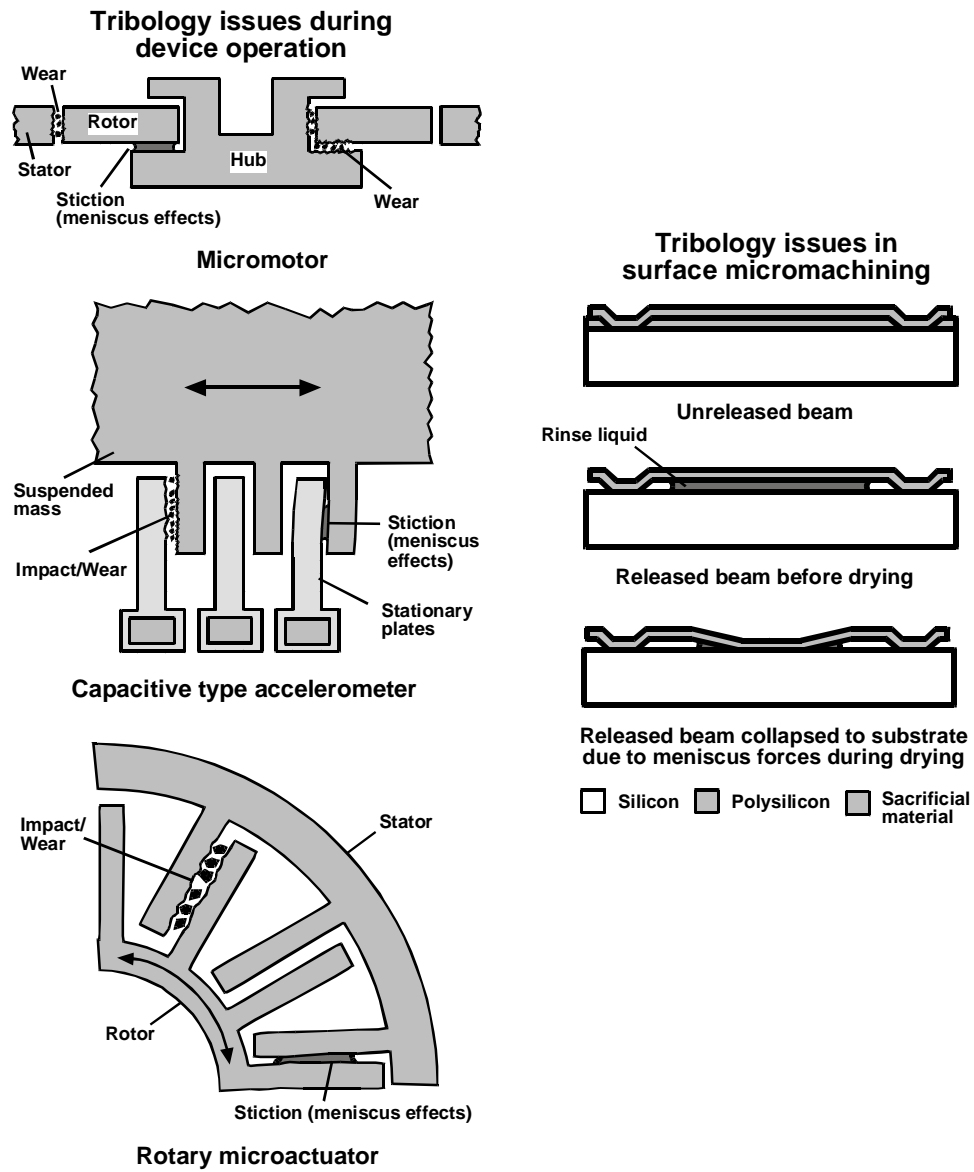


Figure 1.7: Summary of tribological issues in MEMS device operation and fabrication.

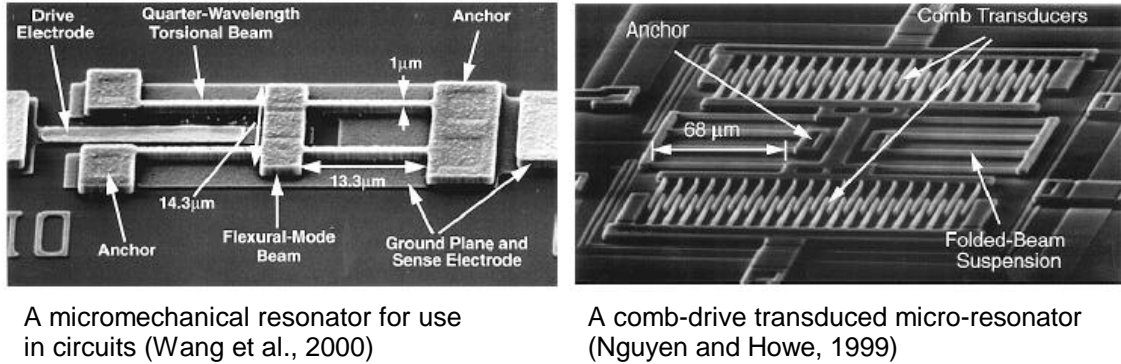


Figure 1.8: Examples of MEMS devices consisting of structures that vibrate at high frequencies. In such applications, fatigue strength is a critical factor affecting reliability.

shows examples of such devices. Such structures need to exhibit excellent mechanical properties on the nanoscale to withstand long lifetimes of failure-free operation. Thus nanomechanics of MEMS structures becomes another critical issue. There is a need to measure mechanical properties of nanoscale MEMS structures to see if the values are comparable to bulk properties of the materials used. We also need to understand how and why the structures fail during static and dynamic loading in order to better design them for longer lives.

Researchers have performed studies on millimeter and micrometer scale silicon-based specimens to determine elastic modulus, fracture toughness, fracture strengths (Johansson et al., 1988; Ericson and Schweitz, 1990; Mazza et al., 1996; Wilson et al., 1996; Wilson and Beck, 1996; Sharpe et al., 1997; Sato et al., 1998; Greek et al., 1999; Tsuchiya et al., 1998, 2000) and fatigue properties (Connally and Brown, 1993; Komai et al., 1998; Kahn et al., 1999). As MEMS structures shrink further to nanoscale dimensions, there is a need to evaluate these properties at the nanoscale. However, studies to study mechanical properties of nanometer scale specimens are lacking, primarily due to difficulties in fabrication of such small-scale test specimens and problems associated with measuring ultra-small physical phenomena in such experiments.

1.3 Micro/nanotribology and the Atomic Force Microscope (AFM)

It is quite clear that tribology and mechanics are critical issues affecting reliable operation of MEMS. Very few studies of these phenomena on the scale relevant to MEMS exist. The advent of micro/nanotribology, pertaining to experimental and theoretical investigations of interfacial processes on scales ranging from atomic- to the microscale, and its associated techniques (Bhushan, 1999a) has provided a viable means of addressing the tribological issues in MEMS.

The introduction of the atomic force microscope (AFM) in 1985 (Binnig et al., 1986) provided a method of measuring ultra-small forces between a probe tip and an engineering surface. It has since then been used for topographical measurements of surfaces on the micro/nanoscale, as well as for adhesion and electrostatic force measurements. Subsequent modifications of the AFM led to the development of the friction force microscope (FFM), designed for atomic- and microscale studies of friction. Today in addition to topography, adhesion and friction, the AFM is being used to investigate a whole range of microscale phenomena such as scratching, wear, indentation, detection of material transfer and boundary lubrication, to mention a few (an extensive list of references can be found in Bhushan, 1999a). As a result, the AFM is also now labeled a scanning probe microscope (SPM). The AFM/FFM is used to provide a model asperity contact with a solid or lubricated surface and AFM-based experiments can reveal much about nanoscale nature of friction and intimate contact during wear and indentation.

The AFM is therefore an ideal tool to study tribological phenomena and evaluate mechanical properties of MEMS materials and components. All the studies performed as part of this research utilized an AFM. Two different commercial AFMs were used. A small sample MultiMode AFM and a large sample Dimension 3000 AFM, both from Digital Instruments/Veeco, Santa Barbara, CA. Details of the operation of an AFM as well as applications can be found from various sources (Wiesendanger, 1994; Bhushan, 1999a; Bonnell, 2001). A brief description is also given in Appendix A, along with

details of the various probes used in this study. Also given in Appendix A are brief descriptions of the techniques used in this study that were developed previously by former researchers at Ohio State.

1.4 Objectives of Research and Overview of Research Efforts

The objectives of this research are (a) to obtain a better understanding of the nanoscale tribological phenomena in MEMS that adversely affect the operation of the devices and to identify viable solutions to minimize or possibly eliminate the effects of these phenomena and (b) to evaluate mechanical properties of nanoscale structures in order to see how the properties compare to values from conventional macro-scale tests and to see how MEMS materials fail at the nanoscale. Figure 1.9 shows an outline of the studies conducted as part of this research effort.

A large part of the research efforts involved the development of techniques using an AFM to achieve the objectives. During the course of the research with the AFM, some contradictions were seen in results of standard measurements with those reported by other groups regarding the effects of surface topography on the measured friction signal. Since friction measurements are a major part of AFM-based research, a study was conducted to explain the effects seen and is described in Chapter 2.

Friction/stiction and wear are the major tribological phenomena that undermine the performance of MEMS. To address the problem of friction, a component level study of the static friction of micromotors was performed, which is described in Chapter 3. This study included development of a technique to measure static friction forces in the devices and identification of a lubrication technique to reduce the friction forces seen. The mechanisms of the friction phenomena observed are also discussed.

To address the problem of wear, ultra-thin hard coatings are viable candidates for use in MEMS as protective coatings, based on their success in magnetic storage systems. The candidate coatings selected were diamond-like carbon coatings. A study to identify the optimal deposition method and thickness for these coatings was conducted. Failure

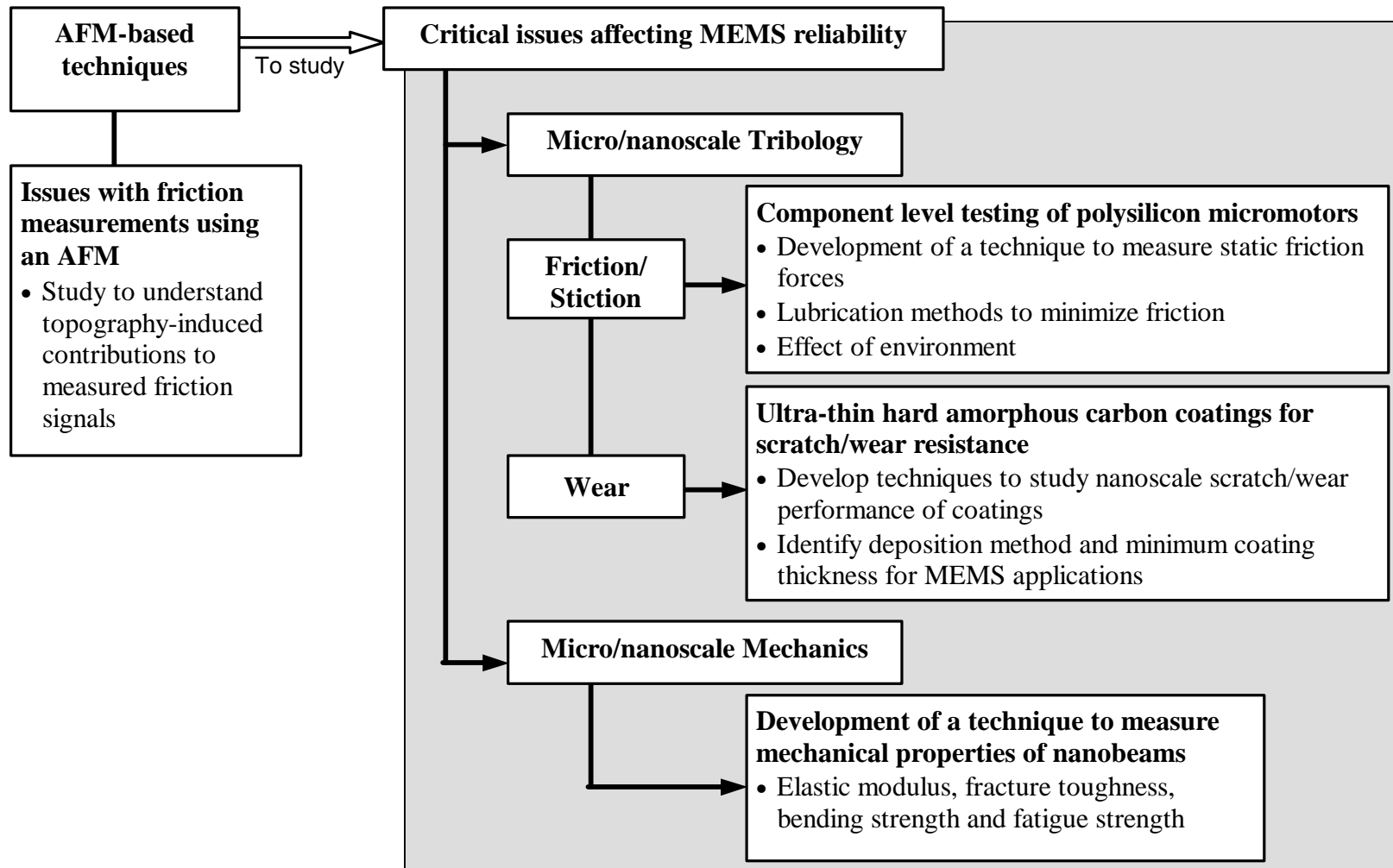


Figure 1.9: Outline of research efforts

mechanisms of such coatings under scratching and wear on the nanoscale are discussed. This work is described in Chapter 4.

Chapter 5 describes the studies to evaluate mechanical properties of nanometer-sized beams. Techniques to measure elastic modulus, fracture strength, fracture toughness and fatigue properties of the beams were developed and failure mechanisms under static and dynamic loading were identified.

The conclusions of the various studies are summarized in Chapter 6.

CHAPTER 2

TOPOGRAPHY-INDUCED CONTRIBUTIONS TO FRICTION FORCES MEASURED USING AN ATOMIC FORCE/FRICTION FORCE MICROSCOPE

2.1 Introduction and Literature Review

Today atomic force/friction force microscopy (AFM/FFM) is extensively used to study friction of various samples at ultra-low loads and scales ranging from micro- down to the atomic scales (Bhushan, 1999a). While scanning direction is perpendicular to the long axis of the cantilever, the lateral forces between the tip and the sample (believed to be representative of friction forces) results in twisting (torsion) of the cantilever. This twisting of the cantilever can be detected by the laser deflection system that is part of the AFM's electronics. This signal is often referred to as 'lateral force signal' or 'friction signal'. This capability of the AFM is ideal to study friction of materials and components on the scale pertinent to MEMS. However, the question of whether this type of measurement yields the true friction properties of the sample material has not been clearly answered. Hence a study to answer this question would be extremely beneficial to nanoscale science as the AFM is a key component in many studies in this field.

It is well known that when an AFM tip is scanned across a sample surface, the measured lateral forces are generated by both material effects (friction) as well as topography-induced effects. However, friction studies in the past, while concentrating on material-induced effects, often present users with conflicting and confusing interpretations of topography-induced friction forces (Overney and Meyer, 1993; Grafstrom et al., 1994; Bluhm et al., 1995; Muller et al., 1997). During friction measurements, the friction signal from both the forward and backward scans (friction loop as shown in Fig. 2.1) are needed in order to understand the origins of the observed

friction forces. It has been reported that topography-induced effects are independent of scanning direction and are hence eliminated when subtracting the friction data of the backward scan from that of the forward scan, leaving only material-induced effects. Other studies have attributed correlations between surface topography and friction forces in scanning probe microscopy to variation of van der Waals forces between high and low points on a surface (Mate, 1993), to influence of local slope of the sample or ‘ratchet mechanism’ (Bhushan and Ruan, 1994; Koinkar and Bhushan, 1997) and to torsion of the cantilever generated by reaction forces and friction forces at locations involving significant surface height change (Haugstad and Gladfelter, 1993).

These reported effects do explain the variations of friction as a function of topography but appear to be independent of the scan direction and agree with the previous suggestion that the subtraction process will eliminate the topography-induced effects. In this chapter, friction studies on samples with well-defined topography variations are presented and it will be shown that the subtraction process does not generally remove the topography-induced effects. The goal of the study (Sundararajan and Bhushan, 2000) presented in this chapter was to study the effect of topography on

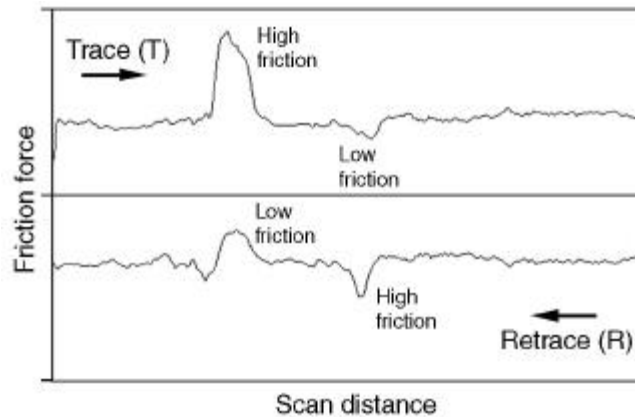


Figure 2.1: Typical friction loop representing friction forces between the AFM tip and sample in the forward (Trace) and backward (Retrace) scanning directions. Note that the sign of the friction forces for the Retrace portion is reversed with respect to the Trace portion due to the reversal of the torque applied to the end of the tip when the scanning direction is reversed.

the measured lateral forces using an AFM/FFM and to identify means to differentiate such effects from the friction effects. It will be seen that at surface locations involving significant changes in topography, the topography-induced contributions to the measured friction forces are found to be different between forward and backward scanning directions. In order to explain these observations, the physical processes involved with topography-induced friction variations are discussed and dynamic effects are considered in addition to static effects in analyzing these variations. Methods to identify topography-induced effects are identified and differences between these effects and material-induced effects are highlighted.

2.2 Experimental

The AFMs used in this study allowed the simultaneous measurement of topography and friction forces. Standard V-shaped silicon nitride cantilevers (see Appendix A for a description of tips) with integrated square-pyramidal tips were used. The height of the tip is 4 μm and the cantilever length is 115 μm , with a spring constant of about 0.6 N/m, all the numbers being the manufacturer's specifications. All scanning was performed in a direction perpendicular to the long axis of the cantilever beam, which is the norm for friction measurements. The normal load used was 25 ± 5 nN.

Two samples with distinct topographical features were utilized in this study. The first was a silicon sample with 5 μm square pits of depth 180 nm and a pitch of 10 μm , commonly used as a calibration grid for the AFM piezos. The second was a gold-coated ruling with a somewhat rectangular grid with a pitch of 1 μm and a ruler step height of about 70 nm. Each sample was composed of homogeneous material and any lateral force (friction) variations seen during measurements would be purely topography-induced.

2.3 Results and Discussion

Figure 2.1 shows a typical friction loop obtained with an AFM/FFM. In this study, we define left to right (forward) direction as *Trace* (T) and the right to left

(backward) direction as *Retrace* (R). It is important to note that the term ‘friction signal’ or ‘friction loop’ denotes the lateral deflection signal measured by the AFM. This is the signal that consists of both the true friction response of the material as well as topography-induced variations. From Fig. 2.1 it can be seen that the sign of the friction signal is reversed for the Retrace scan compared to that of the Trace scan. This is of course due to the reversal of the torque applied to the end of the tip when the scanning direction is reversed. As a consequence when friction data is presented, peaks in 2D friction profiles correspond to high friction for Trace data and low friction for Retrace. This also means that for grayscale images (to be presented shortly), lighter regions in the Trace friction image correspond to higher values of friction force while in the Retrace image, lighter regions correspond to lower friction force. This must be kept in mind when comparing Trace and Retrace friction data.

Figure 2.2 shows topography and friction data for the silicon grid obtained in scope mode with a Dimension 3000 (left column) AFM and Multimode (right column) AFM. Both the friction data show large variations at the edges of the pit where the topography changes sharply. In addition, the friction data obtained with the Dimension shows a large tilt. This is due to cross-talk between the vertical deflection signal and the horizontal deflection signal that arises from misalignment between the trajectory of the reflected laser beam on the photo detector and the photo detector axis (Ruan and Bhushan, 1994). This misalignment is negligible in the case of the Multimode whose data shows no tilting of the friction signal. Hence cross-talk is machine dependent. Looking at the subtracted friction data (T-R), two points are clear. First, the subtraction process does not remove the topography-induced effects associated with the pit edges. Second, effect of detector crosstalk is effectively removed by the subtraction process. Figure 2.3 shows gray-scale and 2D cross sections of topography and friction data for the gold ruler over a 5 μm scan size. The changes in topography in this sample are less severe than that of the silicon grid. Again, it is clear that friction peaks occur at locations of topography variations. It is also clear the subtraction process does not eliminate these variations.

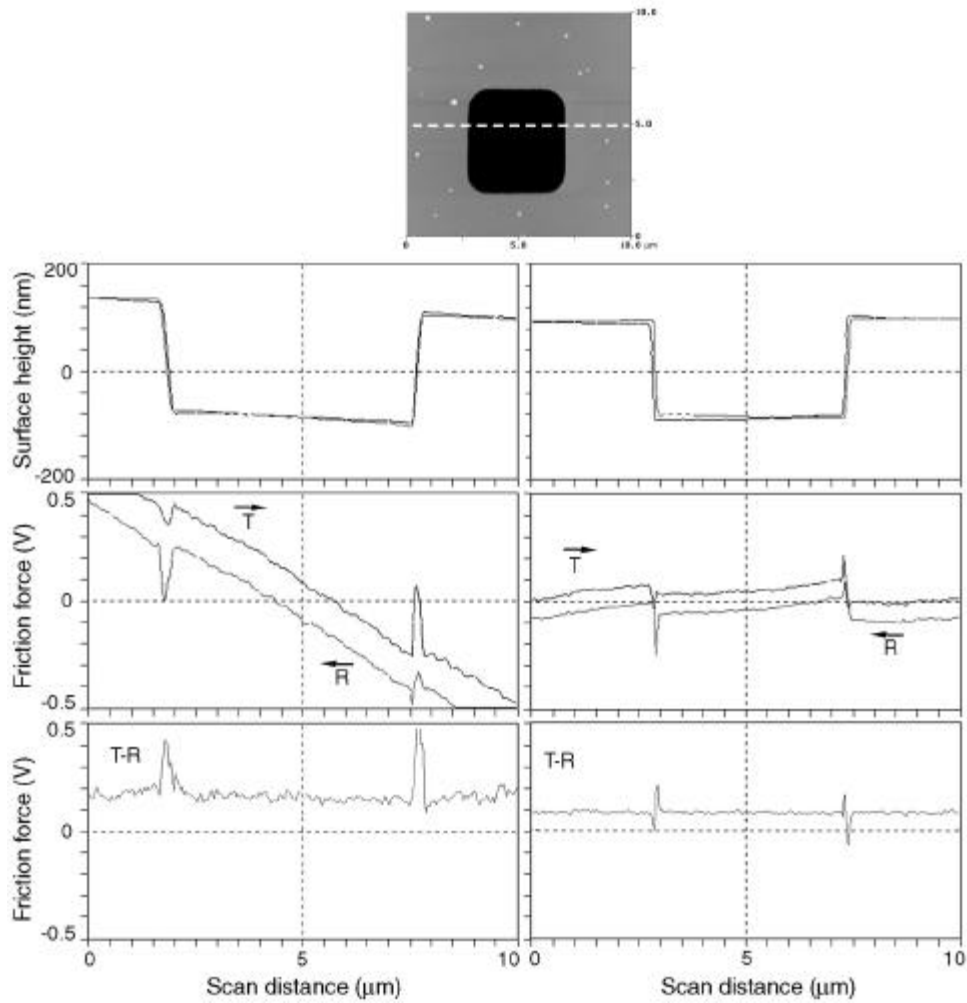


Figure 2.2: 2D profiles of surface height, friction force (loop) and subtracted friction force across a silicon grid pit obtained using a Dimension 3000 AFM (left) and Multimode AFM (right).

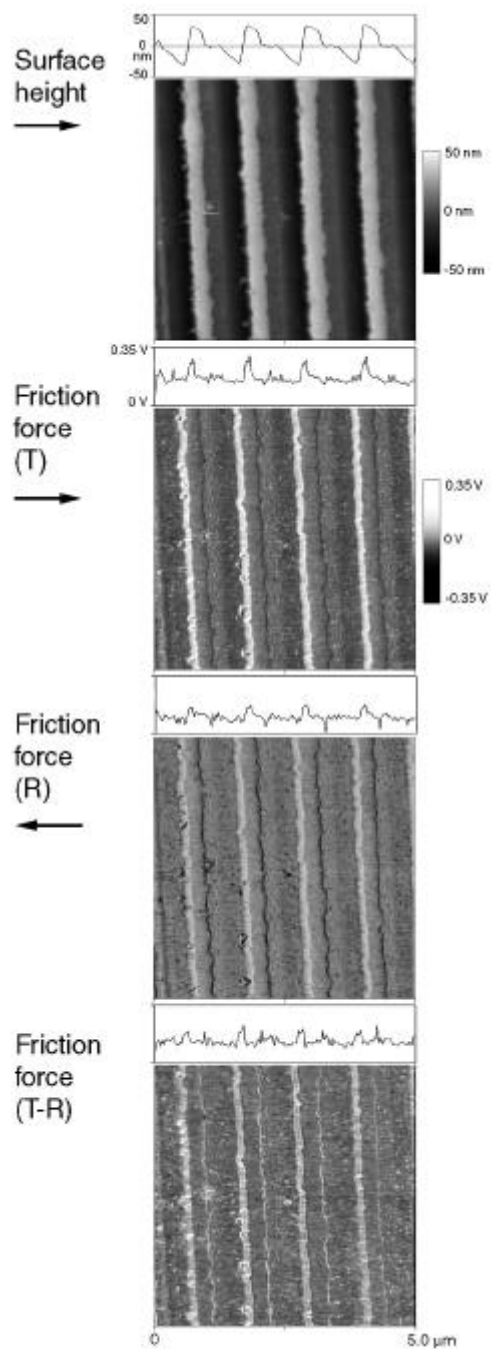


Figure 2.3: Grayscale images and representative 2D profile of surface height and friction forces of a gold ruler. Note that subtracting the friction force data (T-R) does not eliminate topography-induced effects.

Figure 2.4(a) shows topography and friction data for the silicon grid over a 1.5 μm scan size, encompassing a single ruling, obtained using the Multimode. From the 2D traces it is clear that high friction results when the tip traverses up a sharp rise in topography (point A) and low friction results when the tip traverses down a sharp fall in topography (point B). Due to the reversal of sign of the Retrace friction signal with respect to the Trace signal, the friction variations due to topography are in the same direction (peaks in Trace correspond to peaks in Retrace). However, the magnitudes of the peaks in Trace and Retrace corresponding to the same location are significantly different. Rather, the magnitude of the increase in friction force experienced by the tip when scanning up a sharp change in topography is larger than the magnitude of the decrease in friction force experienced when scanning down the same topography change. As a result, subtracting the friction signals (T -R) still yields a residual peak, which is a topography-induced variation. From the grayscale images, it can be seen that this effect occurs at all locations of significant topography change (for example the oval -shaped region at the bottom right of the images). Figure 2.4(b) shows the derivative (slope) of the topography for the corresponding scanning directions. Comparing the slope data to that of friction in Fig. 2.4(a), a clear correlation can be observed between transitions in slope and transitions in friction, which has been reported previously (Bhushan and Ruan, 1994). This effect has been attributed to the ratchet mechanism of friction (Makinson, 1948; Bhushan, 1999a), which has been used in previous studies to explain microscale friction. When a tip applying a constant normal load W , slides over an asperity making an angle θ with the horizontal plane, the lateral or friction force, F , experienced by the tip varies as a function of surface roughness according to the following equations:

$$F_u = W (\mu_0 + \tan \theta)/(1 - \mu_0 \tan \theta) \quad \text{sliding up} \quad (2.1)$$

$$F_d = W (\mu_0 - \tan \theta)/(1 + \mu_0 \tan \theta) \quad \text{sliding down} \quad (2.2)$$

where μ_0 is the coefficient of friction for the tip-sample material pair, F_u is the lateral force experienced by the tip when going up the slope and F_d is the force experienced when going down the same slope. A tip therefore experiences higher

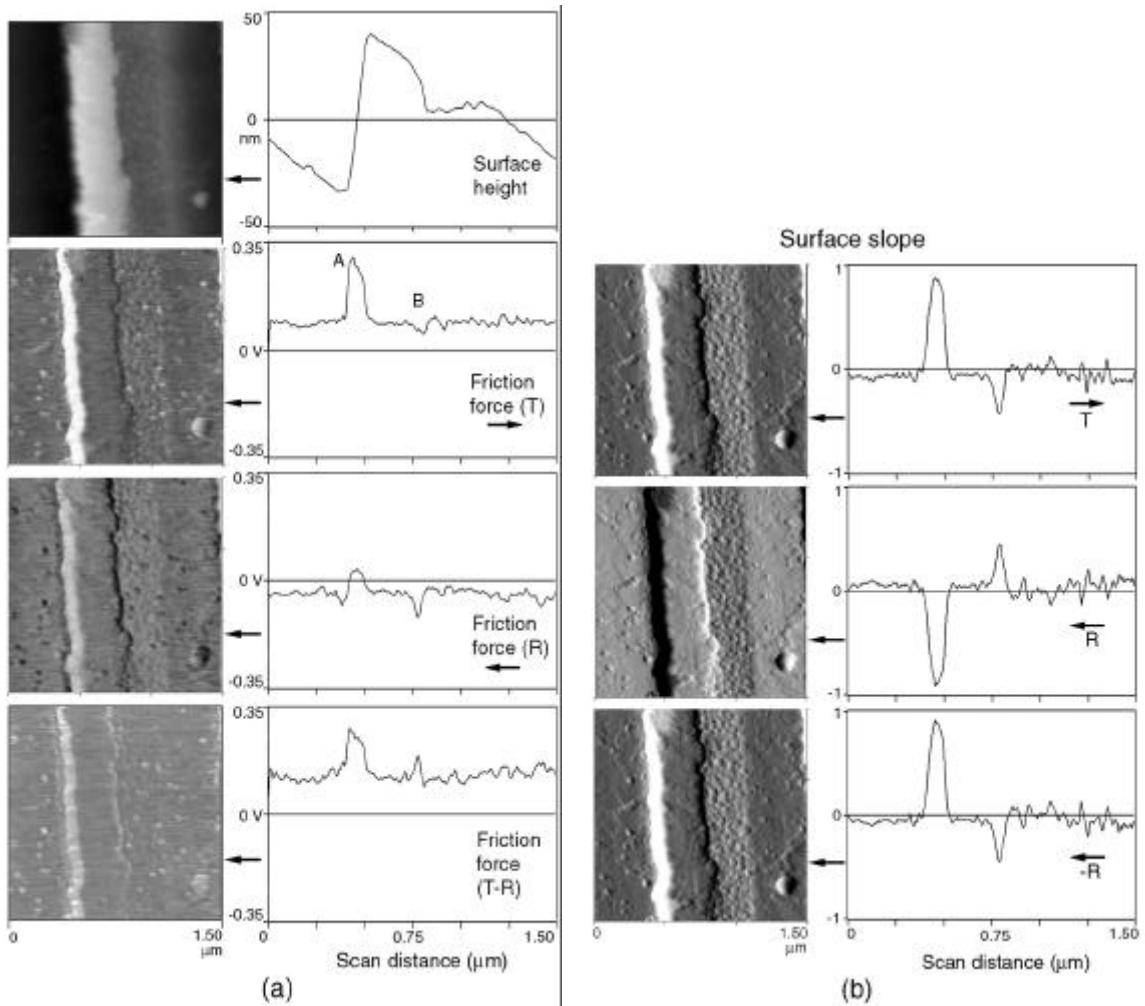


Figure 2.4: (a) Grayscale images and 2D profiles of surface height and friction forces and (b) grayscale images and 2D profiles of surface slope (dz/dx) across a single ruling of the gold ruler.

lateral force when going up a surface slope than when coming down the same slope, which is consistent with the experimental data shown here and elsewhere (Bhushan and Ruan, 1994; Koinkar and Bhushan, 1997; Tamayo et al., 1997; Behary et al., 2000). Associating F_u with the Trace direction and F_d with the Retrace direction, a negative sign will be added to F_d to account for the sign change associated with reversal of scan direction. Thus subtracting ($-F_d$) from F_u (from Eqs. 2.1 and 2.2) is equivalent to the operation of ‘Trace – Retrace’ and will result in

$$F_u - (-F_d) = 2W\mu_0(1 + \tan^2\theta)/[1-(\mu_0 \tan\theta)^2] \quad (2.3)$$

According to equation (2.3), subtraction of the Retrace friction data from the Trace friction data will not eliminate the topography contribution, namely the $\tan \theta$ (slope) term, when $\tan^2 \theta$ becomes comparable to 1. Typically, values of μ_0 on the microscale measured with an AFM range between 0.01 – 0.1. The measured values of $\tan \theta$ for the features studied in this paper, which were obtained from the AFM topography data (dz/dx), were about 0.9 ($\theta \cong 40^\circ$) for the steps in the gold ruler and about 1.5 ($\theta \cong 55^\circ$) for the steps in the silicon grid. The ratchet mechanism therefore accounts for a variation of about 200% of the material-based friction signal ($2W \mu_0$) for the features studied here. However, as mentioned before, performing ‘Trace – Retrace’ still yields a residual peak at the asperity located at the lower right of the grayscale images in Fig. 2.4. The slope here was found to be about 0.3 (corresponding to $\theta \cong 18^\circ$), which is closer to values found for steps and asperities found on engineering surfaces. For this value of slope, the subtraction process (Eq. 2.3) should almost entirely eliminate the ratchet mechanism effect on the measured friction forces. However, a residual peak is still seen at the edge of the asperity, which corresponds to a 30% - 40% variation in the friction signal. This suggests that the difference in lateral force experienced by a tip traversing up and down the same topography feature cannot be attributed solely to the ratchet mechanism.

It is proposed that in addition to the slope effect, the ‘collision’ or impact of a tip when encountering an increase in slope produces additional torsion of the tip leading to higher measured friction force. Consider a tip of finite radius traveling across a surface

with a given normal load and scanning velocity. When the tip encounters a surface feature with a considerable increase in slope such as a sharp asperity or surface step, a ‘collision’ or impact can occur between the leading edge of the tip and the surface feature that results in part of the linear momentum of the tip being converted to angular momentum that leads to torsion of the cantilever. This would be measured as an increase in the friction force signal. In addition, the impact can cause a momentary increase in the applied normal load of the cantilever due to the finite bandwidth of the microscope feedback controller. This would result in an increase in the real area of contact, thereby leading to increased friction force. In some cases, the edge of a step or asperity may come in contact with the side of the tip, which can create an additional torque as soon as the tip is pressed against the step or asperity. Including the term F_c for the lateral force generated by the above effects, Eq. (2.1) can be rewritten as

$$F_u^* = W (\mu_0 + \tan \theta)/(1 - \mu_0 \tan \theta) + F_c \quad \text{sliding up} \quad (2.4)$$

The magnitude of F_c would be a function of the tip radius, the applied normal load and the scanning velocity.

On the other hand, when the tip travels down the same feature, there is no event (certainly no ‘collision’) that can cause a decrease in the friction force that is equivalent to F_c in magnitude. Only the ratchet mechanism affects friction forces during the downward travel. Hence expression (2.2) remains the same. Performing the subtraction operation of ‘Trace – Retrace’ with F_u^* and $(-F_d)$ results in

$$F_u^* - (-F_d) = 2W\mu_0(1 + \tan^2 \theta)/[1 - (\mu_0 \tan \theta)^2] + F_c \quad (2.5)$$

This equation would account for the peaks that occur in a friction profile after subtraction and that are correlated to changes in surface slope. At locations with significant changes in slope ($\tan^2 \theta$ comparable to 1) the topography-induced contribution to the friction signal due to the ratchet effect becomes significant while at locations with small changes in slope, the contribution due to the collision effect becomes significant.

The differences in the magnitudes of the friction peaks when going up and down a sloped region may also be attributed to asymmetry in the tip shape. If this were the case, then the surface slope data for the opposite scan directions would also show differences.

Figure 2.4(b) shows the inverse of the Retrace slope (-R). Comparing this with the Trace slope shows that the two are almost identical, thus ruling out the possibility of tip shape asymmetry being a major cause in affecting friction signals.

Figure 2.5 shows a schematic of the friction loop that can be expected when scanning across a sample that presents both a change in material (with different friction properties) and a change in topography. During the Trace scan, the tip encounters higher friction force at region A due to higher friction of the material. Based on the data and discussion above, at region B, the tip encounters high friction when scanning up the feature and lower friction when scanning down the feature. In the Retrace scan, the same effects are seen. The change in friction force due to the material effect in Trace and Retrace will be in opposite directions (upwards or downwards). However, the changes in friction due to topography in Trace and Retrace will be towards the same direction. This is one difference between material-induced effects and topography-induced effects on the friction forces. The magnitudes of the friction change due to material effects will be the same in Trace and Retrace but the magnitudes of the topography induced friction forces at a given location will be different as was discussed before. As a result, subtracting the Trace and Retrace friction profiles does not eliminate the topography-induced contributions to the friction forces. However, these contributions can be identified by comparing the friction profiles to the slope profiles. As was shown before, topography-induced transitions in friction correspond to transitions in slope. Material effects in friction forces are independent of transitions in slope. This is another difference between material-induced effects and topography-induced effects in friction forces.

When comparing Trace and Retrace friction signals, it is important to take into account the sign change in the Retrace friction signal. Figures 2.6(a) and 2.6(b) show topography, slope and friction data for the silicon grid and gold ruler respectively. The correlations between surface slope and friction forces are clear. The third column shows retrace slope and friction data, which have been inverted (hence labeled as -Retrace). In order to correctly compare directionality effects in friction, the Trace and -Retrace (not raw Retrace) profiles should be compared. From Fig. 2.6 it is clear that the friction experienced by the tip is quite different when scanned across the sample in different

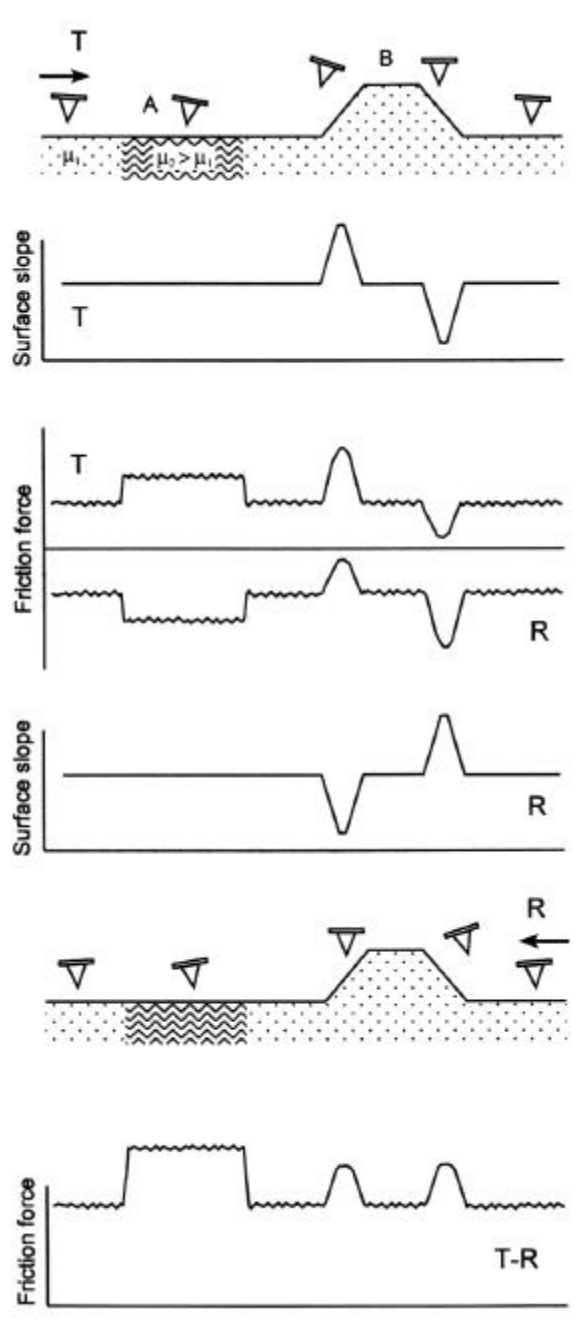
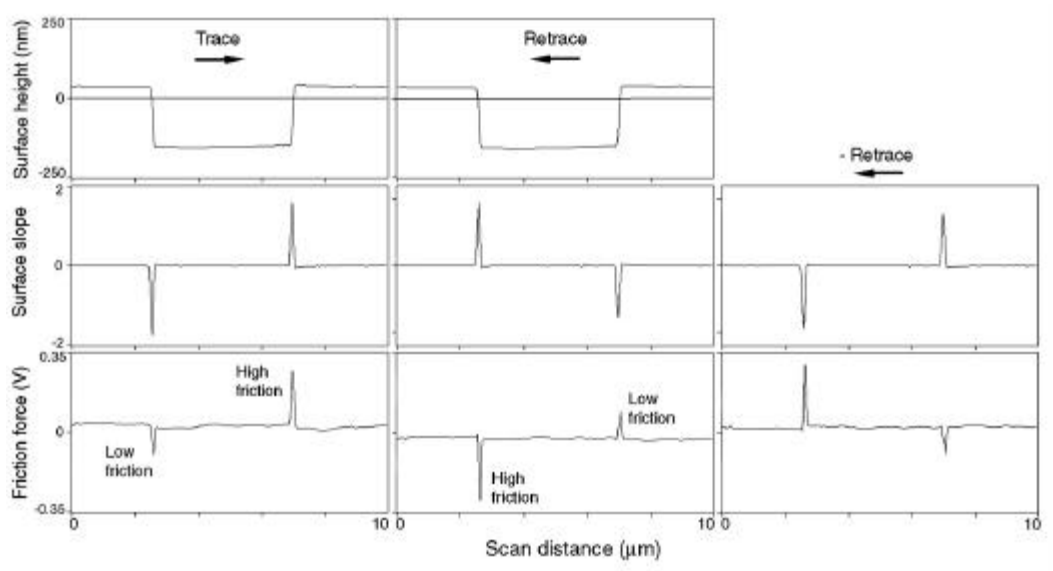
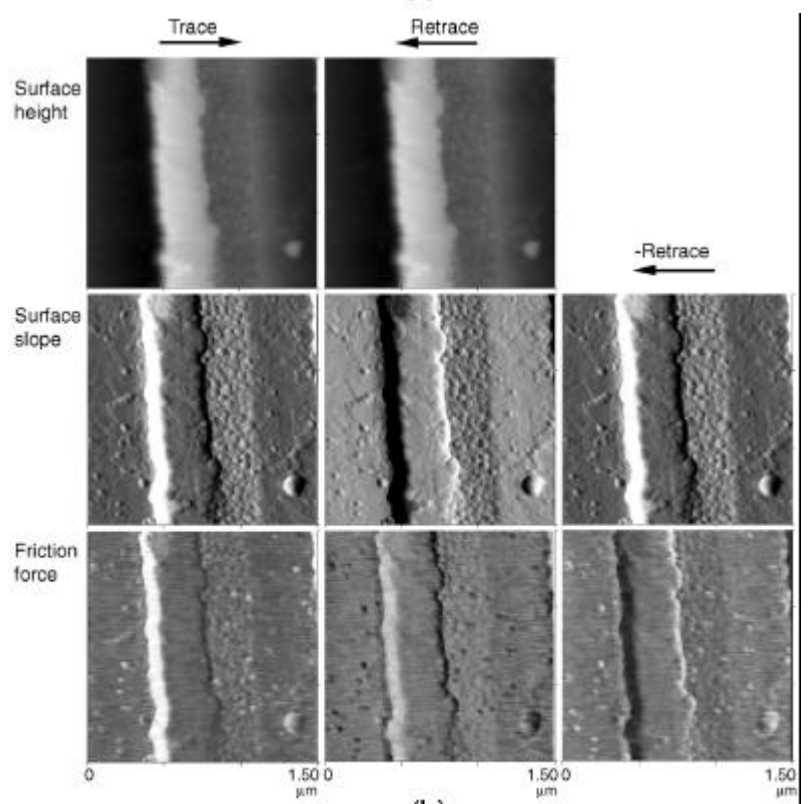


Figure 2.5: Schematic of friction forces expected when a tip traverses a sample that is composed of different materials and sharp changes in topography. A schematic of surface slope is also shown.



(a)



(b)

Figure 2.6: (a) 2D profiles of surface height, surface slope and friction force for a scan across the silicon grid pit.

directions, in this case due to the influence of topography. Comparison of Trace and (–Retrace) slope profiles will also reveal information of tip shape asymmetry.

2.4 Summary

This study focused on understanding topography-induced effects in the friction forces measured using an AFM/FFM. The following points can be made regarding these effects:

- The changes in the friction force due to topography-induced effects will be of the same sign in both Trace and Retrace friction profiles (peaks in Trace correspond to peaks in Retrace) of the friction loop whereas changes due to material effects will be in opposite directions.
- Topography-induced friction transitions always correspond to transitions in surface slope.
- The magnitude of the increase in friction force experienced by a tip when traversing up an asperity, step or similar topography feature is greater than the magnitude of the decrease in friction force experienced by the tip when traversing down the same feature. This is attributed to the ratchet mechanism of friction and to the ‘collision’ force encountered by the tip during the upward movement, which is absent during the downward movement.
- As a result, subtraction of Trace and Retrace friction profiles will not eliminate topography-induced friction forces. This subtraction operation will, however, remove the effect of any detector cross talk on the measured friction forces.

These characteristics of the topography-induced contributions to measured friction forces in an AFM will be useful when attempting to differentiate these effects from material in samples with numerous topographical features (e.g. high roughness). In addition, they aid in understanding the forces experienced by an asperity (AFM tip) when moving over other asperities and similar surface features.

CHAPTER 3

STATIC FRICTION AND SURFACE ROUGHNESS STUDIES OF SURFACE MICROMACHINED ELECTROSTATIC MICROMOTORS

3.1 Introduction and Literature Review

Tribological issues in MEMS were explained in detail in Chapter 1. One of the objectives of this research was to study the tribological phenomena that adversely affect MEMS devices in order to understand the mechanisms and if possible identify ways to minimize or eliminate such problems. In MEMS devices involving parts in relative motion to each other, large friction forces become the limiting factor to the successful operation and reliability of the device. The micromotor is a classic example of a MEMS device where friction is a major concern. This chapter presents a study to measure friction forces of micromotors, to identify lubrication methods to minimize friction forces and to understand mechanisms responsible for the friction properties seen for lubricated and unlubricated motors.

The micromotor was one of the earliest MEMS devices fabricated at MIT and Berkeley (Tai et al., 1989). Figure 3.1 shows an SEM micrograph of this motor. The motor has 12 stators and a 4-pole rotor and is electrostatically driven. Constant contact occurs between the bottom of the rotor and the hub flange while intermittent contact may occur between the rotor and the stator and the rotor and hub circumference during motor operation. It is generally known that most micromotors cannot be rotated as manufactured and require some form of lubrication. It is therefore critical to determine the friction forces present in such MEMS devices. Table 3.1 presents static friction

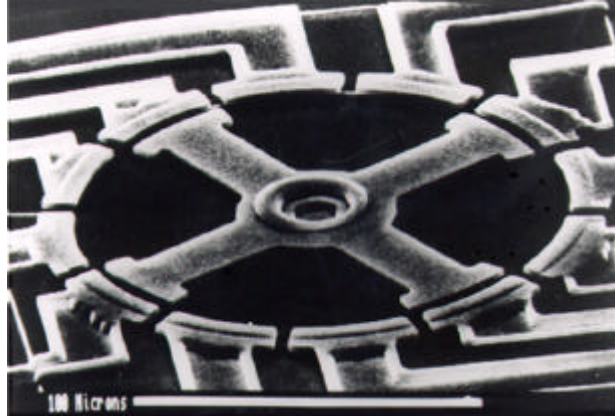


Figure 3.1: One of the first electrostatically actuated polysilicon micromotors (Tai et al., 1989).

Reference	Test method	Device/structure	Material pairs	Environment	Coefficient of static friction
Tai and Muller (1990)	Starting voltage	IC-processed micromotor	PolySi/Si ₃ N ₄	Air	0.20 - 0.40
Lim et al. (1990)	Electrostatic loading	Comb-drive microstructure	PolySi/PolySi PolySi/Si ₃ N ₄	Air	4.9 ± 1.0 2.5 ± 0.5
Maboudian (1992)	Pull-off force	Silicon microbeams	SiO ₂ /SiO ₂	Air	2.1 ± 0.8
Matheison et al. (1996)	Cantilever/fiber deflection rig	LIGA micromotors	Ni/Alumina	Air	0.6 - 1.2

Table 3.1: Data in the literature on coefficient of static friction measurements of MEMS devices and structures.

coefficients of various MEMS devices evaluated by various researchers (Tai and Mueller, 1990; Lim et al., 1990; Maboudian, 1998; Matheison et al., 1996). To measure in-situ the static friction of a rotor-bearing interface in a micromotor, Tai and Muller (1990) measured the starting torque (voltage) and pausing position for different starting positions under a constant-bias voltage. A friction-torque model was used to obtain the coefficient of static friction. To measure the in-situ kinetic friction of the turbine and gear structures, Gabriel et al. (1990) used a laser-based measurement system to monitor the steady-state spins and decelerations. Lim et al. (1990) designed and fabricated a polysilicon microstructure to in-situ measure the static friction of various films. The microstructure consisted of shuttle suspended above the underlying electrode by a folded beam suspension. A known normal force was applied and lateral force was measured to obtain the coefficient of static friction. Beerschwinger et al. developed a cantilever-deflection rig to measure friction of LIGA-processed micromotors (Beerschwinger et al., 1994; Matheison et al., 1996). Most of these techniques employ indirect methods to determine the friction forces or involve fabrication of complex structures. A direct method to measure friction forces in MEMS is needed. The effects of environmental conditions on these forces must also be understood. Effective lubrication methods for these devices need to be determined.

The atomic force/friction force microscope (AFM/FFM) is an ideal instrument for direct measurements of surface phenomena on MEMS devices, components and their surfaces. Here, a novel technique to measure the static friction force (stiction) encountered in surface micromachined polysilicon electrostatic micromotors using an AFM (Sundararajan and Bhushan, 2001a) is presented. In this study, the use of perfluoropolyether (PFPE) liquid lubricants to reduce friction/stiction for micromotors is investigated and the effect of humidity on the friction forces of unlubricated and lubricated devices is studied as well. Mechanisms for the observed friction phenomena are discussed. Also, surface roughness of micromotor components is measured and effect of fabrication steps on surface roughness is discussed, which is a study that appears to be lacking in the literature.

3.2 Micromotor Samples and Lubricants

3.2.1 Polysilicon electrostatic micromotors

Figure 3.2 shows an optical micrograph of the polysilicon electrostatic micromotors used in this study. These motors were fabricated via surface micromachining by Dr. Camon's group at LAAS-CNRS, Toulouse, France (see acknowledgments). Surface micromachining, explained in Chapter 1 as the fabrication of microstructures from deposited thin films, involves deposition and etching sacrificial thin films to produce a freestanding structure. Figure 3.3(a) describes the various steps involved in the surface micromachining of the micromotors used in this study. A brief description is given below, while more details can be found in Conedera et al. (1995).

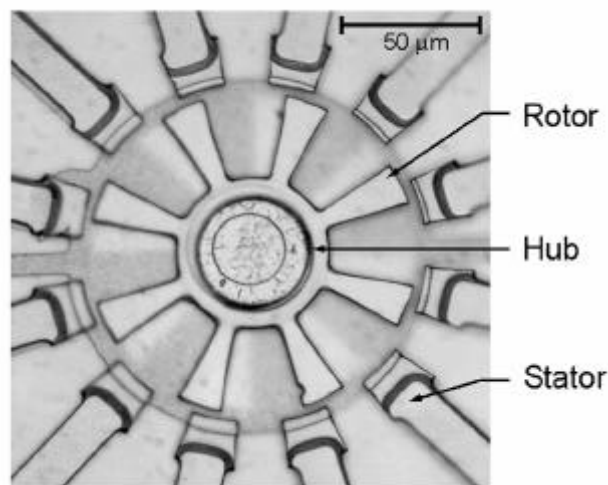


Figure 3.2: Optical micrograph of a typical surface micromachined polysilicon micromotor used in this study.

The first step involves deposition of isolation layers that isolate the micromotor components electrically up to 300 V and avoid mechanical deformation of the substrate. These consist of a 600 nm-thick layer of thermal oxide (produced at 1100 °C in oxygen atmosphere for 1-2 h) followed by a 500nm-thick silicon nitride layer deposited by low - pressure chemical vapor deposition (LPCVD). A 2 μm-thick polysilicon layer is then

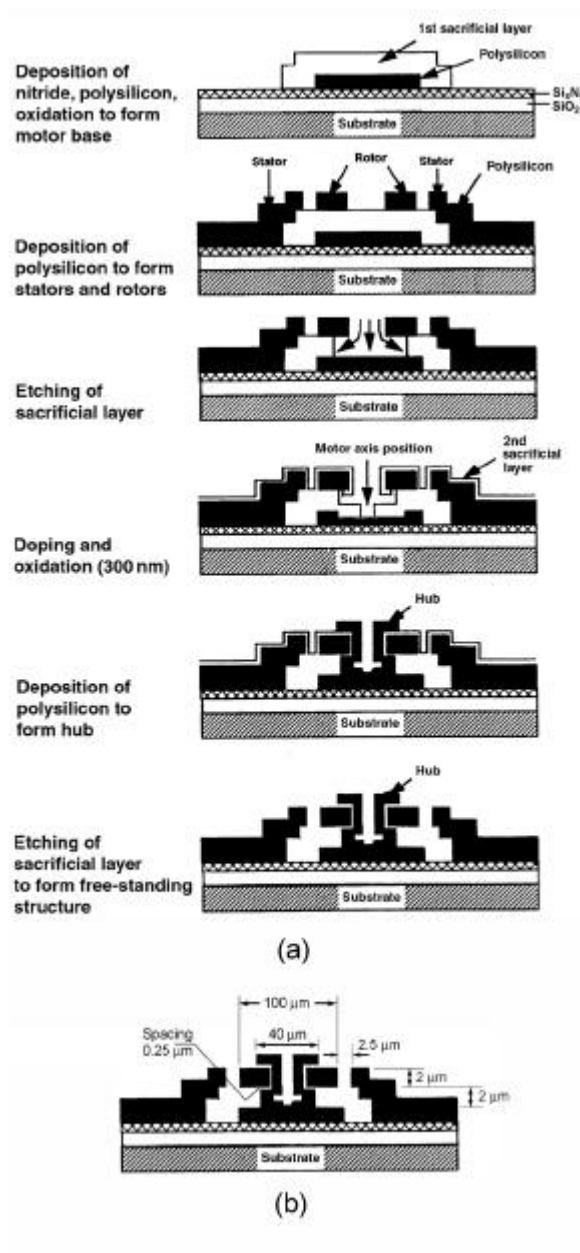


Figure 3.3: (a) Fabrication process sequence of surface micromachined polysilicon micromotors. (b) Dimensions of the micromotor; the clearance between the rotor and the hub is about 250 nm. The figures are not to scale.

deposited at 605°C by LPCVD followed by deposition of thermal oxide, which forms the first sacrificial layer. A second polysilicon layer is then deposited which is subsequently patterned and vertically etched by SF₆ plasma etching to form the rotor and stator electrodes. The first sacrificial layer is then opened up by isotropic wet chemical etching with buffer HF down to the polysilicon layer in the center of the micromotor where the motor hub will be deposited. This geometry allows the rotor to be supported near the hub axis in an attempt to reduce the friction torque. Conductivity of the polysilicon rotor and stator electrodes is then achieved by thermal diffusion of POCl₃ at 1050°C. The second sacrificial layer is deposited at 1000 °C in the presence of steam for 45 min. The advantage of the oxidation is two-fold; first, the sacrificial layer conforms to the shape of the rotor and second; the thickness of the layer can be effectively controlled and minimized (420 nm). The motor hub is then deposited at the center (polysilicon). The last step involves the release of the micromotor by selective wet chemical etching of the sacrificial layer by HF (50%). In this study, motors from two batches (M1 to M4 and M6 to M8 from one batch and M5 from another batch) were used. The difference between the two batches was that the first sacrificial layer was deposited by different deposition systems.

Figure 3.3(b) shows typical dimensions of a micromotor. Constant contact occurs between the bottom of the rotor and the hub flange while intermittent contact may occur between the rotor and the stator and the rotor and hub circumference during motor operation.

3.2.2 Lubricants and lubrication of micromotors

In MEMS, since the tolerances are very small, the most likely mode of lubrication will be boundary lubrication (elastic and plastic deformation of contacting surfaces occur). Using an AFM, boundary lubrication properties of perfluoropolyether (PFPE) lubricants (Koinkar and Bhushan, 1996b) and self-assembled monolayer lubricants (Bhushan et al., 1995b) have been conducted previously. It was decided to use PFPE lubricants to lubricate the micromotors based on the success of such lubricants in the

magnetic storage industry (Chapter 14 in Bhushan, 1999a). While few studies (Deng et al., 1995; Srinivasan et al., 1998) exist on the use of self-assembled monolayer lubricants for MEMS, this is the first study to have attempted to use PFPE lubricants for MEMS devices.

Several types of PFPE lubricants are available (Zhao and Bhushan, 1996), such as Z-15 and Z-DOL. Z-15 is PFPE lubricant with non-reactive $-CF_3$ end groups that make it a mobile lubricant. Z-DOL has $-OH$ end groups that allow it to form chemical bonds with the sample surface when heated to sufficient temperatures. Figure 3.4 shows friction force data of unlubricated silicon and silicon samples lubricated with Z-15 and Z-DOL (Koinkar and Bhushan, 1996a) as an AFM tip slides back and forth repeatedly at a constant normal load. The initial friction force for the Z-15 lubricated sample is lower than that of unlubricated silicon and increases gradually to a friction force value comparable to that of unlubricated silicon after 20 cycles. This suggests depletion of the Z-15 lubricant in the wear track. In the case of the Z-DOL-coated sample (the Z-DOL is chemically bonded), the friction force starts out to be low and remains low during the cycle of 100 tests. It suggests that Z-DOL does not get displaced or depleted as readily as Z-15. Koinkar and Bhushan also showed that Z-DOL is more durable at higher normal loads as well. Based on these results, Z-DOL was chosen for lubricating the micromotors.

Lubrication of a wafer of unlubricated motors with perfluoropolyether lubricant (Z-DOL) was accomplished via a dip-coating technique (Zhao and Bhushan, 1996). The sample was vertically submerged in a bath containing a dilute solution of 0.2% Z-DOL lubricant in hydrocarbon solvent (HT-70) for 10 minutes. The sample was then vertically pulled up from the solution at constant speed and allowed to dry naturally. This resulted in a lubricated sample with a 2 nm-thick coating of as-is Z-DOL. In order to obtain a bonded layer of lubricant (termed Z-DOL BW), the lubricated sample was then baked at $150^\circ C$ for an hour and allowed to cool naturally. Finally, the unbonded portions of the lubricant were removed by dipping the sample in perfluorocarbon liquid (FC-72) for 5 minutes. This resulted in a bonded film thickness of about 1 nm.

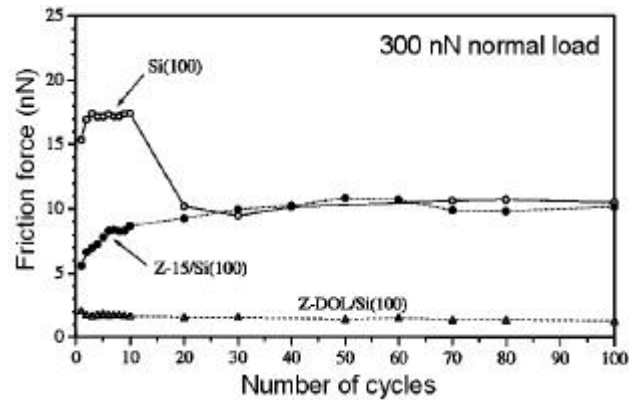


Figure 3.4: Friction force as a function of number of cycles using an Si_3N_4 tip at 300 nN normal load for unlubricated and PFPE-lubricated silicon samples (Koinkar and Bhushan, 1996a).

3.3 Technique to Measure Static Friction Force of the Micromotor

The large sample Dimension 3000 AFM (see Appendix A for description of AFMs) was used in this study. This AFM is equipped with a high magnification video camera and a motorized stage, which facilitate easy location of the area of interest on a micromotor wafer. Topography measurements were made in tapping mode using a standard silicon probe (tip radius of about 10 nm). Microscale friction measurements were conducted using a Si_3N_4 probe (tip radius of about 50 nm, V-shaped cantilever with normal stiffness of 0.6 N/m). For measurement of the static friction forces of the micromotors, a similar Si_3N_4 probe of lower normal stiffness (0.38 N/m) was used for higher lateral deflection sensitivity.

Continuous physical contact occurs during rotor movement (rotation) in the micromotors between the rotor and lower hub flange. In addition, contact occurs at other locations between the rotor and the hub surface and between the rotor and the stator. Friction forces will be present at these contact regions during motor operation. Although the actual distribution of these forces is not known, they can be expected to be concentrated near the hub where there is continuous contact. If we therefore represent

the static friction force of the micromotor as a single force F_s acting at point P_1 (as shown in Fig. 3.5a), then the magnitude of the frictional torque about the center of the motor (O) that must be overcome before rotor movement can be initiated is

$$T_s = F_s l_1 \quad (3.1)$$

where, l_1 is the distance OP_1 , which is assumed to be the average distance from the center at which the friction force F_s occurs. Now consider an AFM tip moving against a rotor arm in a direction perpendicular to the long -axis of the cantilever beam (the rotor arm edge closest to the tip is parallel to the long axis of the cantilever beam), as shown in Fig. 3.5(a). When the tip encounters the rotor at point P_2 , the tip will twist generating a lateral force between the tip and the rotor (event A in Fig. 3.5b). This reaction force will generate a torque about the center of the motor. Since the tip is trying to move further in the direction shown, the tip will continue to twist to a maximum value at which the lateral force between the tip and the rotor becomes high enough such that the resultant torque T_f about the center of the motor equals the static friction torque T_s . At this point, the rotor will begin to rotate and the twist of the cantilever decreases sharply (event B in Fig. 3.5b). The twist of the cantilever is measured in the AFM as a change in the lateral deflection signal (in Volts), which is the underlying concept of friction force microscopy (FFM) as discussed in the previous chapter. The change in the lateral deflection signal corresponding to the above events as the tip approaches the rotor is shown schematically in Fig. 3.5(c). The value of the peak V_f is a measure of the force exerted on the rotor by the tip just before the static frictional torque is matched and the rotor begins to rotate.

The controlled tip movements necessary for this experiment is achieved using the lithography software module (NanoscriptTM) of the Nanoscope. This allows the user to write macros to control the movement of the tip with respect to the sample (Nanoscope Command Reference Manual). In this case, the tip is first made to lift off the polysilicon base so as to obtain a 100-200 nm height difference between the rotor top surface and the end of the tip. This is to ensure that the contact point between the tip and the rotor occurs as close to the end of the tip as possible. A single scan or pass is then made at a low

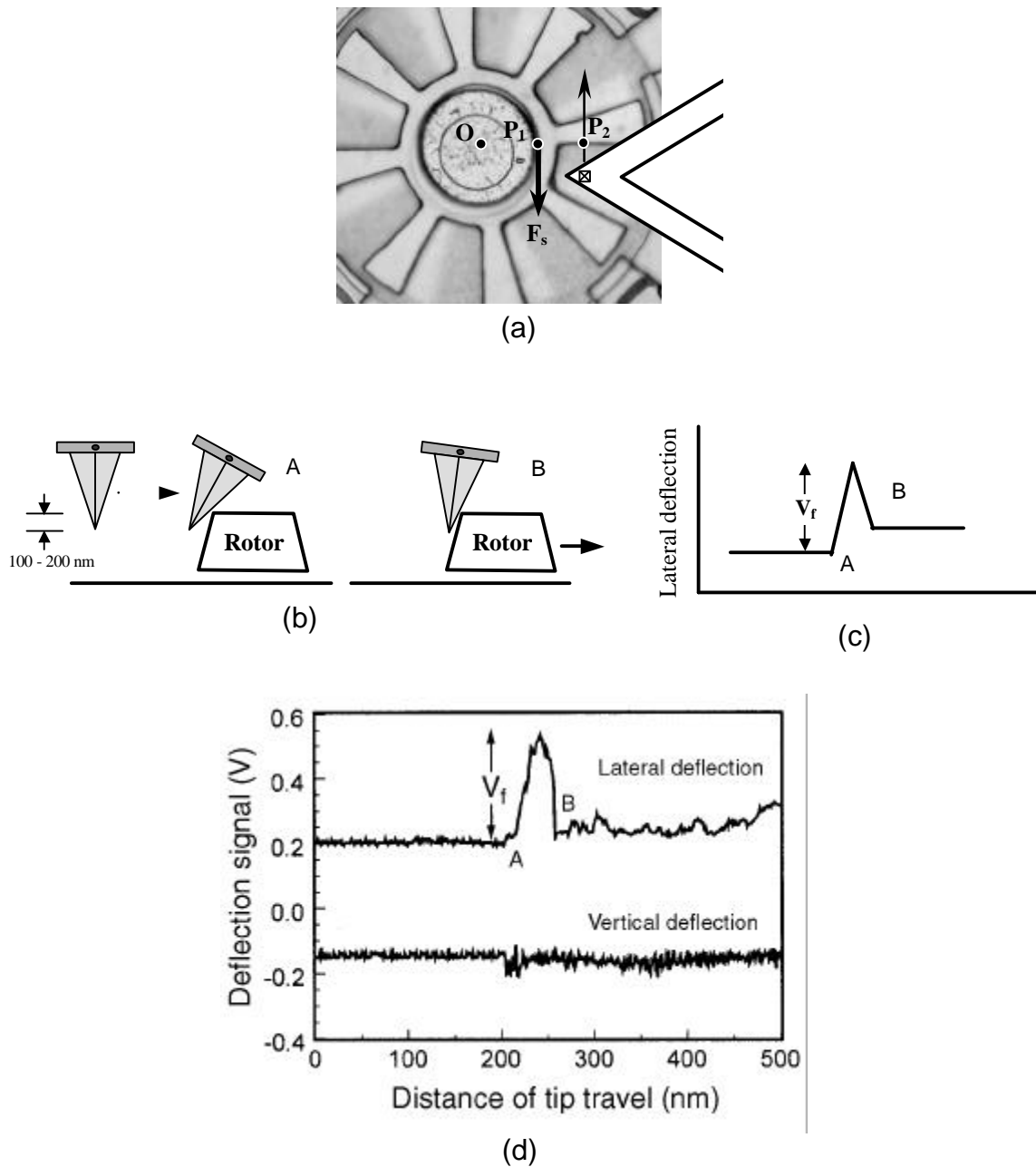


Figure 3.5: (a) Schematic of the technique used to measure the force, F_s , required to initiate rotor movement using an AFM/FFM. (b) As the tip is pushed against the rotor, the lateral deflection experienced by the rotor due to the twisting of the tip prior to rotor movement is a measure of static friction force, F_s , of the rotors. (c) Schematic of lateral deflection expected from the above experiment. The peak V_f is related to the static friction of the motor. (d) Raw lateral deflection and normal deflection data obtained using an AFM (Si_3N_4 tip) against a rotor.

speed of 100 nm/s towards the rotor for a fixed distance. During the execution of the lithography module, the regular user interface of the Nanoscope is disabled. Hence the lateral and normal deflection signals are measured via a breakout box and data acquisition computer equipped with a 12-bit A/D board.

Figure 3.5(d) shows typical lateral deflection and normal deflection data during an experimental run against a rotor. The lateral deflection signal shows the peak V_f associated with the lateral force required to generate rotor movement (F_f). The rotor movement (rotation about the center point O in Fig. 3.5a) can be visually verified during the experiment via the AFM video camera. The normal deflection signal does not change appreciably during this event, indicating that the tip undergoes twisting similar to the torsion encountered in a regular friction experiment using an AFM.

Equating the torques at this instance about the center of the motor gives an expression to determine the static friction force of the micromotor, F_s :

$$F_s = F_f \frac{l_2}{l_1} \quad (3.2)$$

where l_2 is the torque arm of the lateral force about the center of the motor (distance OP_2 in Fig. 3.5a).

To convert the lateral deflection signal V_f to friction force (F_f) a number of calibration experiments are performed. Details of this calibration technique are given in Appendix A. The value obtained for the conversion factor k_f using the above method for was 2.1 nN/V. The method used above assumes that the lateral forces acting on the tip act at the end of the tip. However in the experiment to measure the static friction force of the rotor, this is not the case. As seen in Fig 3.5 (b), a distance of 100-200 nm is maintained between the end of the tip and the top surface of the rotor. This results in the point of contact being 100 – 200 nm above the end of the tip (compared to a tip height of 5 μm). By performing a moment balance about the top of the tip for a force acting 200 nm above the end of the tip and an equivalent force acting at the end of the tip, we find that the actual force is about 2-4% greater than an equivalent force acting at the end of the tip for a given deflection signal. This difference can be considered to be negligible

and hence the conversion factor k_f can be used for the static friction force experiments. In addition the fact that the normal deflection signal does not change significantly (Fig 3.5d) also validates the assumption that the tip undergoes torsion of the cantilever similar to the case when the force acts at the end of the tip. The static friction force can therefore be calculated from Eq. (3.2), as follows:

$$F_s = k_f V_l \frac{l_2}{l_1} \quad (3.3)$$

where the distance l_1 is determined from Fig. 3.2 to be about 22 μm . The distance l_2 is maintained to be about $35 \pm 5 \mu\text{m}$ during the experiments. This was achieved with the aid of the high-magnification camera equipped with the AFM. The variations in l_2 result in a variation of 25% in the calculated value of F_s using this technique.

3.4 Results and Discussion

3.4.1 Static friction force measurements

Static friction force measurements were performed on five unlubricated micromotors (M1 – M5). After static friction force experiments, two of the unlubricated motors (M1 and M2) were lubricated with a 2 nm -thick coating of Z-DOL (as-is). Three different motors (M6 – M8) were directly lubricated with a 1 nm -thick bonded layer of Z-DOL before conducting experiments on them. Figure 3.6(a) presents the measured values of static friction force (as per Eq. 3.3) for various unlubricated and lubricated micromotors (at ambient conditions; RH = 45% and 23 °C). The solid symbols represent the static friction force measured on the very first experiment on a given motor. The open symbols represent values from subsequent experiments. Each open data point shown is an average of six measurements. The distribution of the data points was random. Figure 3.6(b) shows normalized static friction force, which is obtained by dividing the measured value of static friction force by the weight of the rotors, which was calculated to be 0.254 nN by multiplying the density of polysilicon (2500 kg/m³) by the

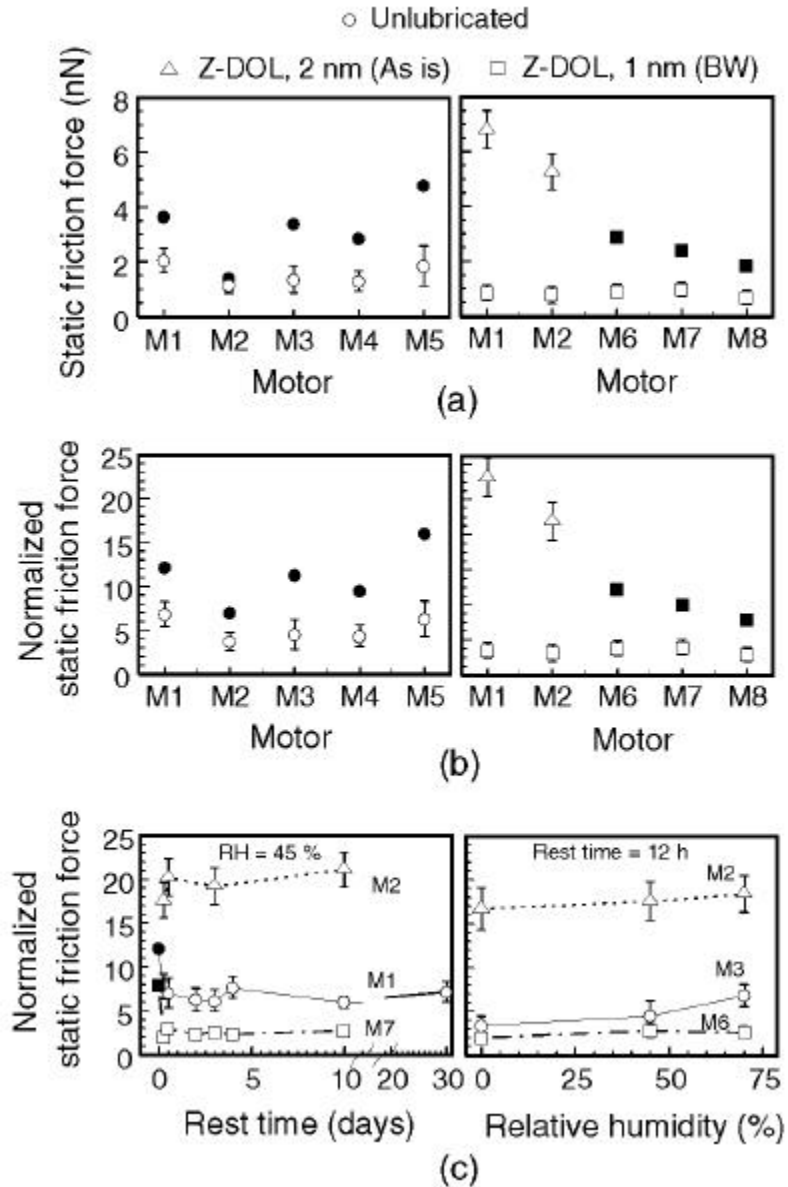


Figure 3.6: (a) Static friction force data (raw and normalized with the weight of the rotor) for unlubricated and lubricated micromotors. The solid points indicate the force obtained in the first experiment for a given rotor, while the open points indicate values obtained on subsequent runs. Motors M1 – M4 and M6 – M8 are from Batch 1 and M5 is from the Batch 2. (b) Normalized static friction force data for selected micromotors as a function of rest time and relative humidity. Rest time is defined as the time elapsed between a given experiment and the first experiment in which motor movement was recorded (time 0). The motors were allowed to sit at a particular humidity for 12 hours prior to measurements.

volume of the rotor calculated using the dimensions in Fig. 3.3(b). Electrostatic and meniscus forces are not included here in the normal force, which would result in the value of coefficient of static friction lower than the values of the normalized static friction force reported here.

Figure 3.6(a) shows that in all cases, the initial static friction force is the highest for a given rotor. Subsequent values, although exhibiting considerable variability, are substantially lower. The initial values of static friction force (solid symbols) for unlubricated and lubricated are comparable to each other, with normalized values being between 5 and 12, which are slightly higher than the values in Table 3.1 for polysilicon/polysilicon. However the effect of the bonded lubricant layer can be seen in the subsequent measurements. The values of normalized static friction force for M6 - M8 are a little lower (under 4) than that of the unlubricated motors and also show much less variability. A layer of as-is mobile lubricant produces disastrously high values of static friction force that are up to 3 to 5 times higher than that of unlubricated motors (M1 and M2). Upon subsequent bonding and washing, M1 and M2 show static friction forces comparable to M6 -M8 that appear to be lower than the unlubricated case. Thus a bonded layer of Z-DOL appears to result in some improvement in the static friction characteristics of the motors, while even a 2 nm thick mobile layer results in very high friction forces.

3.4.2 Effect of rest time and humidity

Figure 3.6(c) shows the normalized static friction forces for unlubricated and lubricated motors as a function of rest time. Rest time here is defined as the time elapsed between the first experiment conducted on a given motor (solid symbol at time zero) and subsequent experiments (open symbols). Each open symbol data point is an average of six measurements. It can be seen that for the unlubricated motor (M1) and the motor lubricated with a bonded layer of Z-DOL (M7), the static friction force is highest for the first experiment and then drops to an almost constant level. In the case of the motor with an as-is mobile layer of Z-DOL, the values remain very high up to 10 days after lubrication.

In order to study the effect of humidity on the static friction forces of the micromotors, the samples were housed for 12 hours at a given humidity in a control chamber with separate inlets for dry and humid air. The humidity was maintained to $\pm 3\%$ RH except for 0% which showed no variation. The sample was then taken out of the chamber and the static friction test was performed using the AFM, usually within 15 minutes. Figure 3.6(c) also shows normalized static friction forces on unlubricated and lubricated motors as a function of relative humidity. In all cases, there is negligible difference in the static friction force at 0% and 45% RH. This is probably due to the fact that the motors were stored in ambient (45% RH) for some period of time before the humidity tests and a 12-hour period of confinement at 0% RH would probably not eliminate all the water films on the sample surface. At 70% RH, the unlubricated motor (M3) exhibits a substantial increase in the static friction force, while the motor with bonded Z-DOL (M6) shows no increase in static friction force due to the hydrophobicity of the lubricant layer. The motor with an as-is mobile layer of the lubricant (M2) shows consistently high values of static friction force that varies little with humidity.

3.4.3 Surface roughness measurements

Most of the friction forces resisting motion in the micromotor are concentrated near the rotor-hub interface where continuous physical contact occurs. Surface roughness of the surfaces usually has a strong influence on the friction characteristics on the micro/nanoscale. Table 3.2 shows various surface roughness parameters obtained from 5 μm scans of the various component surfaces of several unlubricated micromotors using the AFM in tapping mode. A surface with a Gaussian height distribution should have a skewness of zero and kurtosis of three (See Appendix C for a description of surface roughness parameters). Although the rotor and stator top surfaces exhibit comparable roughness parameters, the underside of the rotors exhibits lower RMS roughness and peak-to-valley values. More importantly, the rotor underside shows negative skewness and lower kurtosis than the topsides, both of which are conducive to high real area of contact (Bhushan, 1999b) and hence high friction. The rotor underside also exhibits

higher microscale coefficient of friction than the rotor topside and stator. Surfaces for batch 1 show higher P-V, skewness and kurtosis values as compared to batch 2. The increased roughness is desirable for low friction. It was reported that batch 1 motors ran after lubrication whereas motors of batch 2 did not (Camon, personal communication, 2000).

	RMS Roughness ^a (nm)		Peak-to-Valley Distance ^a (nm)		Skewness ^a , Sk		Kurtosis ^a , K		Microscale coefficient of friction ^b (μ)	
	1 ^c	2 ^c	1	2	1	2	1	2	1	2
Rotor Topside	21 ± 0.6	20 ± 1	225 ± 23	210 ± 26	1.4 ± 0.30	0.90 ± 0.11	6.1 ± 1.7	5.3 ± 1.4	0.07 ± 0.02	0.08 ± 0.01
Rotor Underside	14 ± 2.4	-	80 ± 11	-	-1.0 ± 0.22	-	3.5 ± 0.50	-	0.11 ± 0.03	-
Stator Topside	19 ± 1	21 ± 0.7	246 ± 21	150 ± 10	1.4 ± 0.50	1.1 ± 0.10	6.6 ± 1.5	3.9 ± 0.30	0.08 ± 0.01	0.08 ± 0.01

^a Measured from a tapping mode AFM scan of size 5 μm x 5 μm using a standard Si tip scanning at 5 $\mu\text{m/s}$ in a direction orthogonal to the long axis of the cantilever.

^b Measured using an AFM in contact mode at 5 μm x 5 μm scan size using a standard Si₃N₄ tip scanning at 10 $\mu\text{m/s}$ in a direction parallel to the long axis of the cantilever.

^c 1 and 2 correspond to batches 1 (M1 – M4, M6 – M8) and 2 (M5).

Table 3.2: Surface roughness parameters and microscale coefficient of friction for various micromotor component surfaces measured using an AFM. Mean and $\pm 1\sigma$ values are given.

Figure 3.7 shows representative surface height maps of the various surfaces of a micromotor measured using the AFM in tapping mode. The rotor underside exhibits varying topography from the outer edge to the middle and inner edge. At the outer edges, the topography shows smaller circular asperities, similar to the topside. The middle and inner regions show deep pits with fine edges that may have been created by the first etching step (see Fig. 3.3). Previous studies have also shown that etching can affect the surface roughness of surfaces in surface micromachining (Maboudian and Howe, 1997). Figure 3.8 shows surface roughness of the surface beneath the rotors (the first polysilicon

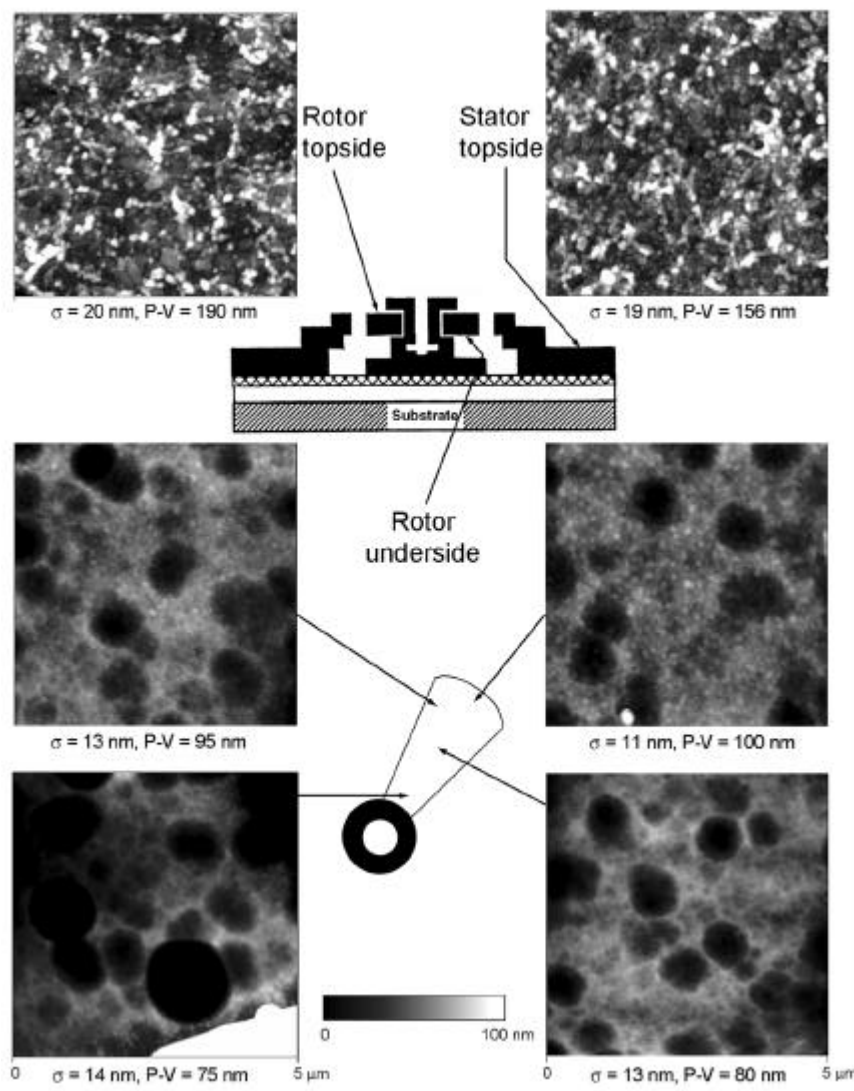


Figure 3.7: Representative AFM surface height images obtained in tapping mode ($5 \mu\text{m} \times 5 \mu\text{m}$ scan size) of various component surfaces of the micromotors (Images shown are that of motor M1). RMS roughness (σ) and peak-to-valley (P-V) values of the surfaces are given. The underside of the rotor exhibits drastically different topography from the topside.

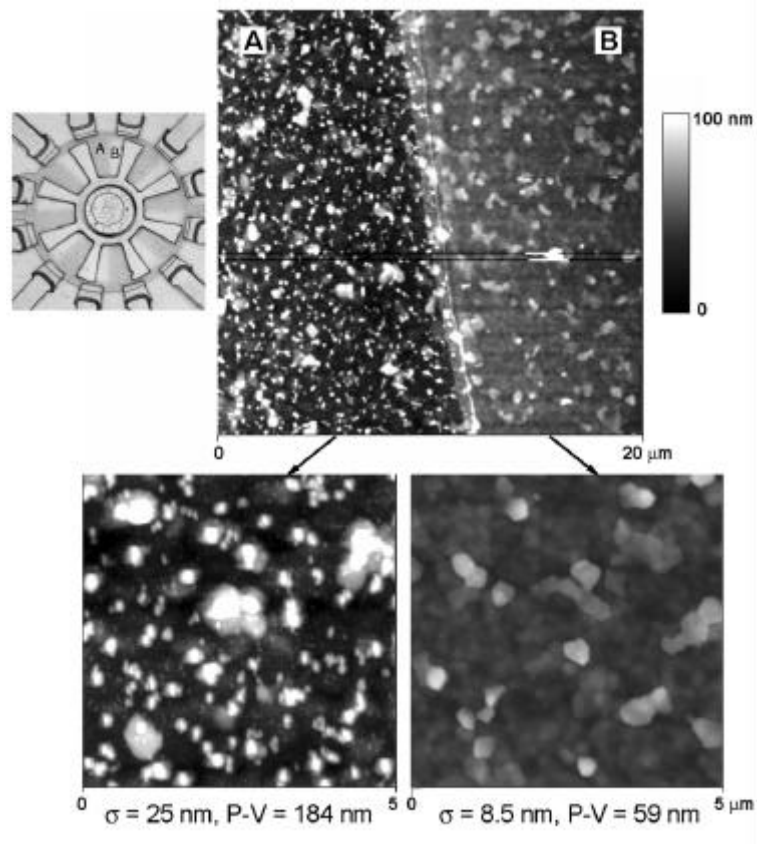


Figure 3.8: Surface height images of polysilicon regions directly below the rotor (for motor M1). Region A is away from the rotor while region B was initially covered by the rotor prior to the release etch of the rotor. During this step, slight rotation of the rotor caused region B to be exposed.

layer). There appears to be a difference in the roughness between the portion of this surface that was initially underneath the rotor (region B) during fabrication (right) and the portion that was away from the rotor and hence always exposed (region A). The former region shows lower roughness than the latter region. This suggests that the surfaces at the rotor-hub interface that come into contact at the end of the fabrication process exhibit large real areas of contact that result in high friction.

3.4.4 Discussion

Figure 3.9 summarizes static friction force data for motors M1 and M2 along with schematics of the meniscus effects for the unlubricated and lubricated surfaces. Capillary condensation of water vapor from the environment results in formation of meniscus bridges between contacting and near-contacting asperities of two surfaces in close proximity to each other as shown in Fig. 3.9. For unlubricated surfaces, more menisci are formed at higher humidity resulting in higher friction force between the surfaces (Bhushan and Sundararajan, 1998). The formation of meniscus forces is supported by the fact that the static friction force for unlubricated motors increases at high humidity (Fig. 3.6c). Solid bridging may occur near the rotor-hub interface due to silica residues after the first etching process (Maboudian and Howe, 1997). In addition, the drying process after the final etch can result in liquid bridging formed by the drying liquid due to capillary force at these areas (Mastrangelo and Hsu, 1993; Maboudian and Howe, 1997; Bhushan, 1999b). The initial static friction force therefore will be quite high as evidenced by the solid data points in Fig. 3.6. Once the first movement of the rotor permanently breaks these solid and liquid bridges, the static friction force of the motors will drop (as seen in Fig. 3.6) to a value dictated predominantly by the adhesive energies of the rotor and hub surfaces, the real area of contact between these surfaces and meniscus forces due to water vapor in the air. At this point, effects of lubricant films can be observed.

Lubrication with a mobile layer, even a thin one, results in very high static friction forces due to meniscus effects of the lubricant liquid itself at and near the contact regions.

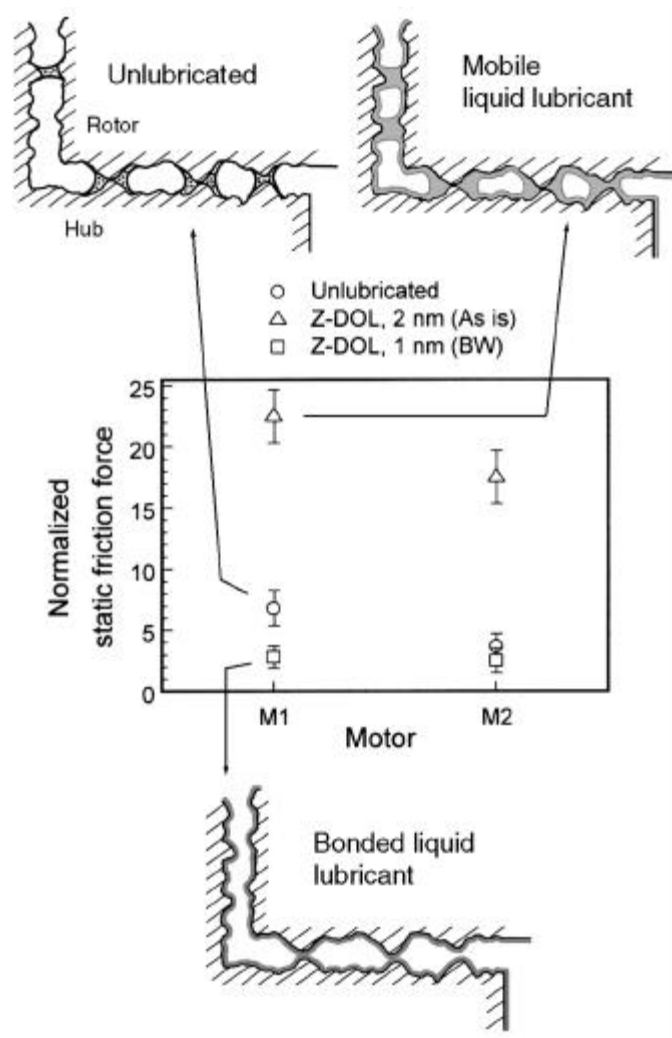


Figure 3.9: Summary of effect of liquid and solid lubricants on static friction force of micromotors. Despite the hydrophobicity of the lubricant used (Z-DOL), a mobile liquid lubricant (Z-DOL as is) leads to very high static friction force due to increased meniscus forces whereas a solid-like lubricant (bonded Z-DOL) appears to provide some amount of reduction in static friction force.

It should be noted that a motor submerged in a liquid lubricant would result in a fully flooded lubrication regime (Bhushan, 1999b). In this case there is no meniscus contribution and only the viscous contribution to the friction forces would be relevant. A motor submerged in silicon oil did run (Camon, personal communication, 2000). However, this may not be a practical method of lubricating and/or packaging motors. A solid-like hydrophobic lubricant layer (such as bonded Z-DOL) results in favorable friction characteristics of the motor. The hydrophobic nature of the lubricant inhibits meniscus formation between the contact surfaces and maintains low friction even at high humidity (Fig. 3.6c). This suggests that solid-like hydrophobic lubricants are ideal for lubrication of MEMS while mobile lubricants result in increased values of static friction force.

3.5 Summary

A novel technique to measure the static friction force of surface micromachined polysilicon micromotors using an AFM was developed. This technique was used to study the friction characteristics of unlubricated and lubricated motors.

- Static friction forces normalized to the rotor weight for a polysilicon-polysilicon contact were found to be in the range of 4 – 10 for unlubricated micromotors.
- A bonded layer of Z-DOL (PFPE) lubricant appeared to provide good lubrication to the micromotors by reducing the normalized static friction force to below 4. A thin mobile layer of lubricant resulted in static friction forces up to three times higher than the values obtained for unlubricated ones.
- A variation in the static friction forces with humidity was observed for the unlubricated motors, which was explained in terms of meniscus effects at the rotor-hub interface.
- The undersides of the rotors exhibited drastically different topography from the topsides due to contact with etchants and favored large real areas of contact and high friction forces.
- Solid-like hydrophobic lubricants appear to be ideal for lubrication of MEMS.

CHAPTER 4

MICRO/NANOTRIBOLOGICAL STUDIES OF ULTRA-THIN HARD AMORPHOUS CARBON COATINGS FOR SCRATCH AND WEAR RESISTANCE

4.1 Introduction

The problem of wear is another tribological issue affecting the performance of MEMS devices. One method to reduce or prevent wear is the use of hard protective coatings that have superior scratch and wear resistance compared to the substrate. For a coating to be used in MEMS, it must be very thin (less than a 100 nm) since the tolerances are very small; it must be chemically inert and there should be no mechanical finishing steps since the devices are small and can have complex geometries.

Hard amorphous carbon coatings, also called diamond-like carbon (DLC) coatings, are considered as good candidates as wear-resistant coatings for MEMS. These coatings have been the center of attention due to their interesting properties such as very high hardness and elastic modulus, high electrical resistivity, high thermal conductivity, high optical transparency and chemical inertness, which are close to that of diamond. Thin DLC coatings reproduce substrate topography, not requiring any post-finishing. DLC coatings already have wide range of uses including optical, electronic, thermal management (heat sinks), biomedical and tribological applications (Lettington, 1998).

The magnetic storage industry (MSI) also requires the use of such thin wear-resistant coatings where they are used as overcoats for magnetic heads and hard disks. The most recent coatings used are of thicknesses ranging from 100 nm down to 10 nm. Intensive research is underway to develop DLC coatings as thin as possible – down to 5 nm and less. These coatings would be ideal for MEMS as well. However, the important

questions are: will these ultra -thin coatings possess the necessary properties that they were designed for, will they perform their role satisfactorily, and if not why?

A systematic study of the effect of coating thickness of these DLC coatings on their scratch and wear resistance at light loads is necessary in order to understand how these coatings fail. It is important to carry out tests that simulate contact s and loads comparable to that experienced in MEMS. Using an AFM, loads in the range of micronewtons, contact situations very similar to those occurring in head -disk interfaces and MEMS device interfaces are created and under which performance of the DLC coatings can be studied. Few studies exist on the performance of such thin DLC coatings (Bhushan and Koinkar, 1995; Gupta and Bhushan, 1995a,b; Li and Bhushan, 1998).

The objectives of this study (Sundararajan and Bhushan, 1999; Sundararajan and Bhushan, 2001b) were to identify the to identify deposition processes that produce superior coatings for wear-resistance, the minimum coating that exhibits good wear -resistance, and to understand failure mechanisms of such ultra -thin coatings during scratching and wear. Coating thicknesses of 20, 10, 5 and for the first time, 3.5 nm of were studied. Microscale friction, scratch and wear experiments were conducted using an atomic force/friction force microscope.

4.2 DLC coating samples

Coatings on silicon substrate obtained from four different deposition techniques namely, filtered cathodic arc (FCA), direct ion beam (IB), RF -biased electron cyclotron resonance plasma chemical vapor deposition (ECR -CVD) and RF sputter deposition (SP) were studied. Table 4.1 lists these techniques, the coating labels employed in this chapter, a brief description of each deposition process as well as typical values of kinetic energy of the depositing species and deposition rates. The coatings have been listed in decreasing order of $sp^3:sp^2$ ratio (Gupta and Bhushan, 1995a). Coatings of 20, 10 and 5 nm thicknesses obtained from each deposition method were studied. In addition 3.5 nm coatings obtained via FCA, IB and ECR-CVD processes were also studied. Detailed descriptions of the filtered cathodic arc, ion beam and sputter deposition processes are

given in Gupta and Bhushan (1995a). Details of the ECR -CVD process can be found in Suzuki and Okada (1995).

Coating Name	Deposition Technique	Process	Kinetic Energy (eV)	Deposition Rate (nm s ⁻¹)
FCA	Filtered Cathodic Arc	Arc Plasma generates energetic ions from graphite cathode	100-2500	0.1-1
IB	Direct Ion Beam	Carbon ions produced from methane gas in an ion source and accelerated towards a substrate	50-500	0.1-1
ECR-CVD	Electron Cyclotron Resonance Plasma Chemical Vapor Deposition	Hydrocarbon ions generated from ethylene gas in the presence of a plasma in electron cyclotron resonance (ECR) condition are accelerated towards an RF-biased substrate	10-50	1-10
SP	RF Sputtering	Sputtering of graphite target by argon ion plasma	1-10	1-10

Table 4.1: List of coatings studied and their selected parameters.

The common feature of these techniques is that the deposition is energetic, i.e. the carbon species arrive with an energy significantly greater than that represented by the substrate temperature. The resultant coatings are amorphous, low in hydrogen content and display a high degree of sp³ character. In general, these coatings consist of a mixture of sp³ and sp² bonding and higher fraction of sp³ bonding results in higher hardness (Gupta and Bhushan, 1995a; Bull, 1995). Table 4.2 lists the hardness and elastic modulus of 100 nm thick coatings deposited by the various techniques as measured using a commercial Nanoindenter (Nanoindenter II from MTS, Oak Ridge, TN). A three-sided pyramidal diamond (Berkovich) indenter with a radius of about 100 nm was used. The hardness and elastic modulus values were obtained at a peak load of 0.2 mN and at peak indentation depths ranging from 18 -23 nm, which is about 20% of the coating thickness. All coatings showed comparable surface roughness values with typical RMS values of 0.5 – 0.9 nm and peak-to-valley distance of 3.8 – 5.1 nm. Bare Si(100) exhibited an

RMS of about 0.1 nm and peak-to-valley distance of 0.9 nm. An Si interlayer was used for the SP coatings; a 2 nm interlayer in the case of the 5 nm coating and a 3.5 nm interlayer in the case of 10 and 20 nm coatings. No interlayer was used in the case of FCA, IB and ECR-CVD coatings. The vendors primarily deposit these coatings on non-silicon substrates (such as Al₂O₃-TiC for magnetic recording applications). For these samples, the SP process requires a Si interlayer to enhance adhesion of the carbon layer by the formation of SiC at the interface. Both the Si interlayer and carbon layer are

Coating	Hardness ^a (GPa)	Elastic modulus ^a (GPa)	Fracture toughness ^b K _{IC} (MPa m ^{1/2})
FCA	24	280	11.8
IB	19	140	4.9
ECR-CVD	22	180	6.4
SP	15	140	2.8
Bare Si(100)	11	165	0.95

^a Measured on 100 nm thick coatings using Nanoindenter at peak load of 0.2 mN. Peak indentation depths were about 20% of the coating thickness.

^b Measured using a Nanoindenter on 100 nm thick coatings at peak indentation load of 100 mN, 50 mN and 20 mN for FCA, ECR-CVD and SP coatings respectively. Data for Si(100) is the handbook value.

Table 4.2: Hardness, elastic modulus and fracture toughness of various 100 nm thick coatings.

deposited by sputtering. The Si interlayer is not required on a silicon substrate. However, the interlayer was used to conform to their standard deposition process. The other deposition methods were developed in a manner that eliminated the need for an interlayer. The mechanical and tribological properties of a DLC coating depend on the sp³:sp² –bonded carbon ratio, the amount of hydrogen in the coating and the adhesion of the coating to the substrate. These various factors in turn are influenced by the precursor material, energy of the carbon species prior to deposition, deposition rate, substrate temperature and biasing (Gupta and Bhushan, 1995a).

4.3 Experimental techniques

Two sets of tests were performed. The first was using existing scratch and wear techniques, which require multiple scan cycles. The second was using a technique developed as part of the research effort; a continuous microscale scratch test.

The continuous microscratch test is a scratch test in which a normal load is applied to a scratch tip and is gradually increased during scratching. This has been widely used to measure adhesion and scratch resistance of coatings for some time (Mittal, 1978). Such 'continuous scratch' tests are used to identify the minimum normal load or critical load at which a failure event occurs (such as detachment of the coating or sudden increase in damage to the sample), which is used as a basis for comparing scratch resistance or adhesion of coatings. Methods to determine critical load during scratching include monitoring acoustic emission or AE (Perry, 1981; Valli, 1986, Steinmann et al., 1987; Wu, 1991) and monitoring of tangential or friction force during scratching (Jacobson et al., 1983; Valli, 1986; Wu, 1991; Bhushan et al., 1995a). In the latter method, the normal load at which a sharp increase in the friction force encountered by the tip occurs is usually considered to be the critical load. This method has been employed to study microscratch resistance and adhesion of thin coatings by several researchers using a commercial Nanoindenter as well as other instruments. In such cases post-scratch imaging is done with a separate instrument such as a scanning electron or optical microscope, which is inconvenient and may also result in loss of damage event information during sample handling between the instruments.

The continuous scratch test (at increasing loads) is not possible on most commercial AFMs unless substantial modifications are made to the instrument at high cost. Even then, such modifications allow post-scratch imaging only in contact mode. This can often result in misleading images since some debris may be swept away by the sliding tip, even at low loads, which is disadvantageous when trying to correlate measured data (such as friction force) with any damage events observed in the scratch image. Here, a method is presented to implement a continuous microscratch technique in a commercial AFM without the need for separate instrumentation or modification to the

microscope. An additional advantage of this technique is that post-scratch imaging can be performed 'in-situ' with the AFM in tapping mode, which minimizes loss of debris and other damage indicators in the scanned region as compared to contact mode.

Information regarding critical loads and failure mechanisms at and above these loads can be obtained using this type of test for the DLC coatings.

4.3.1 Scratch and wear tests using multiple cycles

A diamond tip (radius ~ 70 nm)/stainless steel cantilever (stiffness = 40 N/m) was used for these scratch and wear experiments. Scratch and wear tests were performed using existing techniques developed previously in this laboratory. A description of the techniques and tips are given in Appendix A.3 and A.4 respectively. 'Evolution of wear' type tests were performed to study the failure mechanisms of the coatings during wear. However, during these wear tests, in addition to surface height, the friction signal was also obtained to study the relationship between the ploughing forces and onset of wear, which is a novel concept. These signals were converted into force units using the method outlined in Appendix A.2.

Due to the large number of cycles involved in scratch and wear tests on numerous hard coatings, the diamond tip may undergo some wear. This wear must be accounted for when measuring scratch depths and when comparing loads during wear tests. During these tests, the diamond tip did show signs of wear as shown in Fig. 4.1, where the scratch depths obtained on uncoated Si(100) at different times during the course of our experiments are shown. The consistently decreasing scratch depth values clearly indicate that the tip becomes blunt. Hence the scratch depths obtained on DLC samples, say after 6 tests, are not accurate since by now the tip has become blunt as indicated by the scratch depths in Fig. 4.1(a). We chose to account for this problem by calibrating the scratch depths obtained on the DLC samples by applying a linear scaling factor to the scratch data based on the difference in scratch depths seen on uncoated Si(100) (Fig. 4.1a). The magnitude of the correction factors, as a function of number of tests conducted, are given in Fig. 4.1(b). These factors were obtained by dividing the initial scratch data on Si(100) by the corresponding scratch depths after the given number of tests. These scaling

factors were then applied to the raw data obtained on the DLC samples. For example, for the data on the samples in tests 3-6, the scaling factor of 1.5 was used and so on.

In the case of wear tests, we applied a similar scaling factor to the normal loads instead of the wear depths. That is, we calculated a scaling factor based on the applied load rather than obtained wear depth and the magnitudes of the correction factor were in the range of 1.5 – 2.5. This was because the wear tests were at a given constant normal load rather than as a function of normal load. It was generally seen that wear of the tip was not a concern at loads below 30 μN . All data presented in this chapter are inclusive of scaling factors. Although this is not a foolproof method, it helps to avoid gross errors in data interpretation due wear of the tip.

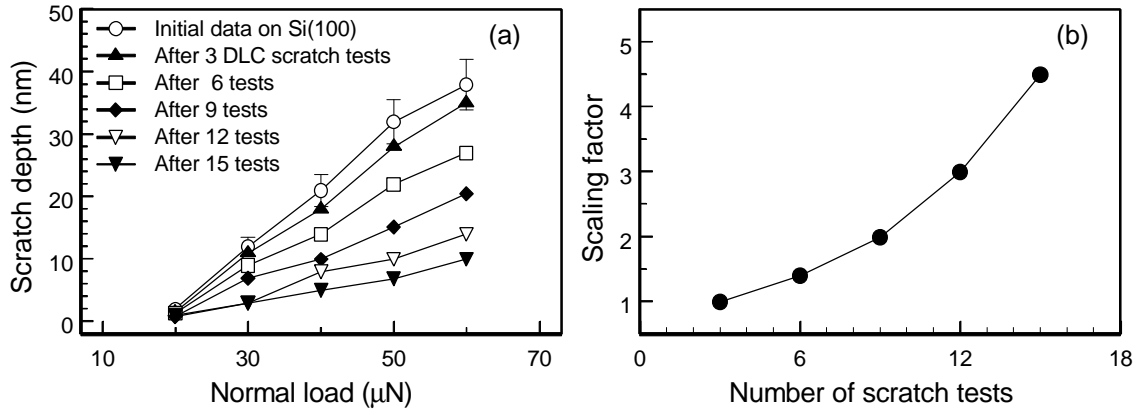


Figure 4.1: (a) An example of scratch depths obtained on uncoated Si(100) during the course of the scratch tests, illustrating the effect of blunting of the diamond tip. (b) Magnitudes of the scaling factors used for the scratch data.

4.3.2 Development of a continuous microscratch technique to study scratch resistance using an AFM

The details of the continuous microscratch technique developed for the AFM without the need for separate instrumentation or modification to the microscope are given here. A diamond tip (radius ~ 100 nm)/stainless steel cantilever (stiffness = 36 N/m) was used for these experiments.

4.3.2.1 Generation of a scratch at increasing normal load

A perfectly linear increase in the normal load can be achieved by supplying the z -piezo of the AFM with a continuously varying voltage input from an external source according to the non-linear characteristics of the piezo. But by doing so, the feedback that controls the applied normal load will no longer function, which would result in loss of control of the applied normal load. An alternate method is presented in which the linear increase in normal load is approximated by a large number of normal load increments, where each increment is of small magnitude. This can be achieved by utilizing a software module that allows controlled movement of the tip. In the Nanoscope III, the lithography module (Nanoscript™) allows the user to write macros to control the movement of the tip with respect to the sample. Using this module, the user can make the tip describe a variety of movements ranging from a simple straight line to complex patterns. The range of this movement is restricted by the maximum scan size of the piezo. During the execution of these movements, the feedback is still in effect thus allowing the normal load to be controlled.

Using the Nanoscript module, a program has been written to simulate a continuous scratch test as a series of normal load increments each of a small magnitude as shown in Fig. 4.2 (the program code is given in Appendix B). The scratch is generated by moving the tip with respect to the sample in a direction perpendicular to the long-axis of the cantilever. This is the direction of tip travel required to measure the friction (lateral deflection) signal in an FFM. The number of normal load increments for the scratch test can be set to any value while the maximum speed of the tip with respect to

the sample is limited by the specifications of the piezo (on the order of 100 $\mu\text{m/s}$). For most of the experiments reported here, a speed of 0.5 $\mu\text{m/s}$ was used and the number of steps was usually taken to be 500.

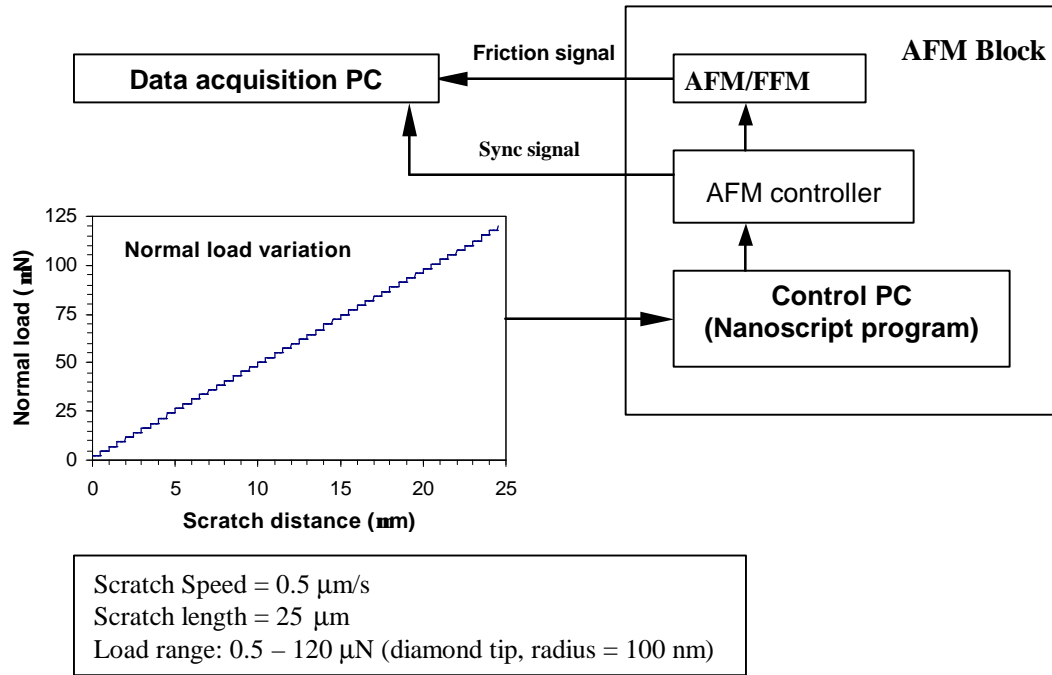


Figure 4.2: Schematic of continuous microscratch technique implemented in a commercial atomic force/friction force microscope (AFM/FFM).

4.3.2.2 Measuring friction force during scratching

A disadvantage of the lithography module is that when executed, the user interface is disabled. Hence any signals to be measured (in this case, the lateral deflection or friction force signal) must be tapped out of the microscope and collected separately. Here, the lateral deflection (friction) signal is obtained through a breakout box (Digital Instruments) and measured with a 12 bit A/D board.

To convert the lateral deflection signal to friction force units, a number of calibration experiments are performed based on Ruan and Bhushan (1994), which is

described in Appendix A.2. In this experiment, an Al₂O₃ sample was used to obtain the conversion factor of the cantilever. The value obtained for the conversion factor k_f using the above method was 14.9 $\mu\text{N/V}$.

Prior to the initiation of a scratch test, the initial lateral deflection signal or offset value, F_0 , (corresponding to zero normal load) is noted. The lateral deflection data obtained during scratch F is then converted to friction force as follows:

$$\text{Friction force} = [F - F_0] \times k_f \quad (4.3)$$

where k_f is the conversion factor of the cantilever as discussed before. Coefficient of friction during scratch is obtained by dividing the friction force by the corresponding normal load.

4.3.2.3 Effect of detector cross talk and topography on measured friction signal

Misalignment between the axis of vertical deflection of the cantilever and the vertical axis of the photodetector can cause a coupling between vertical deflection (normal load) and measured lateral deflection (friction) signals (as seen in Chapter 2). To determine the effect of this cross talk between the vertical and lateral deflection signals, a pure indentation test was performed and the lateral deflection signal was monitored (Hector and Schmid, 1998). The normal load in contact was varied over the entire range (1 - 150 μN) used for the scratch test. Figure 4.3(a) shows the results of such a test using the diamond tip cantilever assembly in the Multimode AFM on Si(100) where the normal load was varied from 1 – 150 μN in 50, 100 and 500 steps. The vertical scale shown is the typical range over which the friction signal varies for a scratch test performed on Si(100). From Fig. 4.3(a), the variation in the lateral deflection signal due to a pure change in vertical deflection is 7% of the maximum lateral signal encountered in a scratch experiment. Thus the effect of cross talk for the cantilever assembly used in the Multimode AFM for this study can be considered to be negligible.

Another effect to be considered when studying lateral deflection signals is the effect of topography. The study in Chapter 2 showed that at sharp changes in topography where there is considerable change in surface slope, sharp changes in lateral deflection

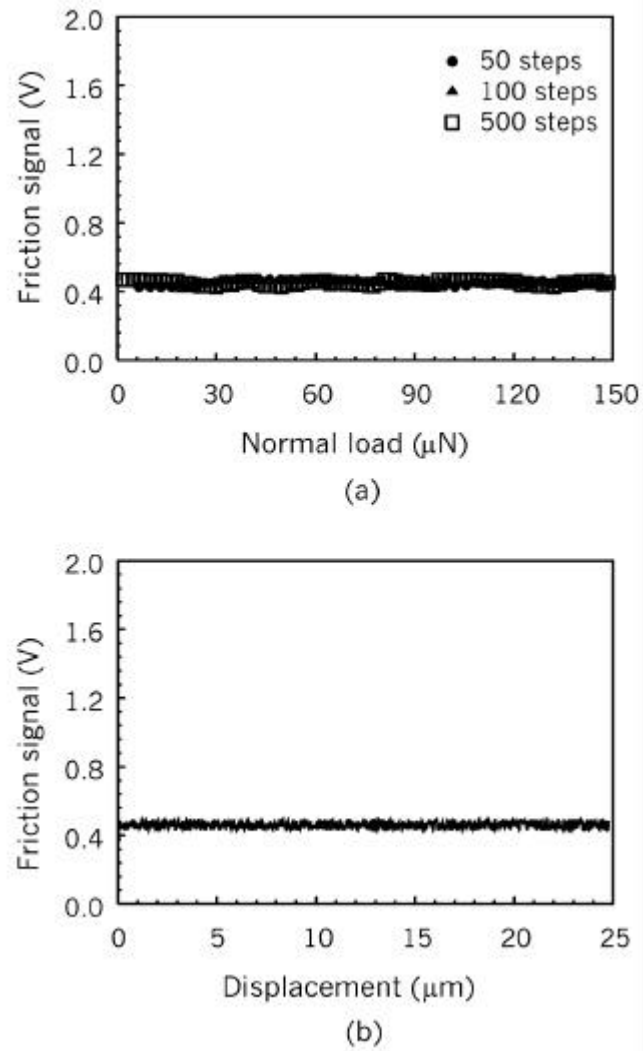


Figure 4.3: (a) Coupling effect between vertical (normal) and lateral deflection (friction) signals and (b) effect of topography on friction signal on Si(100). Both effects are negligible in this study.

(friction force) are observed when measured with an AFM. Since in the microscratch test, sharp changes in friction force are indicative of critical loads, it is important to be able to differentiate these variations in the signal from variations due to topography. Before a scratch test is performed on a sample, a dummy 'scratch' at constant normal load, low enough to avoid ploughing, is performed and the lateral deflection signal is monitored. The data for one such test on Si(100) is presented in Figure 4.3(b). The variation of the lateral deflection signal is 0.1 V, which is insignificant compared to the lateral deflection of about 2 V, encountered in a scratch test. This was found to be the case for smooth samples (RMS < 1 nm) such as Si(100) and the carbon coatings. The variation in the signal seen in Fig. 4.3(b) also shows the low noise level (low variation) present during the measurement of the lateral deflection signal for this technique.

Even though in this particular case, the effect of detector cross talk and topography was negligible, they are important factors to be considered when undertaking such scratch tests in an AFM/FM for a given sample. If there is any effect due to either of the above factors, they must be taken into account when analyzing the friction data.

4.4 Results and discussion

4.4.1 Scratch and wear tests using multiple cycles

The results of the scratch tests are shown in Fig. 4.4. The samples are grouped by deposition method in 4.4(a) and by coating thickness in 4.4(b). For comparison, scratch results of bare Si(100) are shown in each plot with error bars that are typical of these tests (about 8%). All the coatings provide better scratch resistance than bare silicon, although in different degrees. From the data, it is clear that for a given deposition method, the thicker the coating, the better the scratch resistance. This is true for all the deposition methods with the exception of the SP coatings, whose scratch resistance appears to be independent of coating thickness. Among 20 nm coatings, FCA and ECR -CVD coatings show negligible scratch depths. Among 10 nm coatings, ECR -CVD and IB appear to be better than the other two. 5 nm coatings do provide good scratch resistance compared to bare Si(100) and the IB coating appears to be a little better than the rest. In all cases, SP

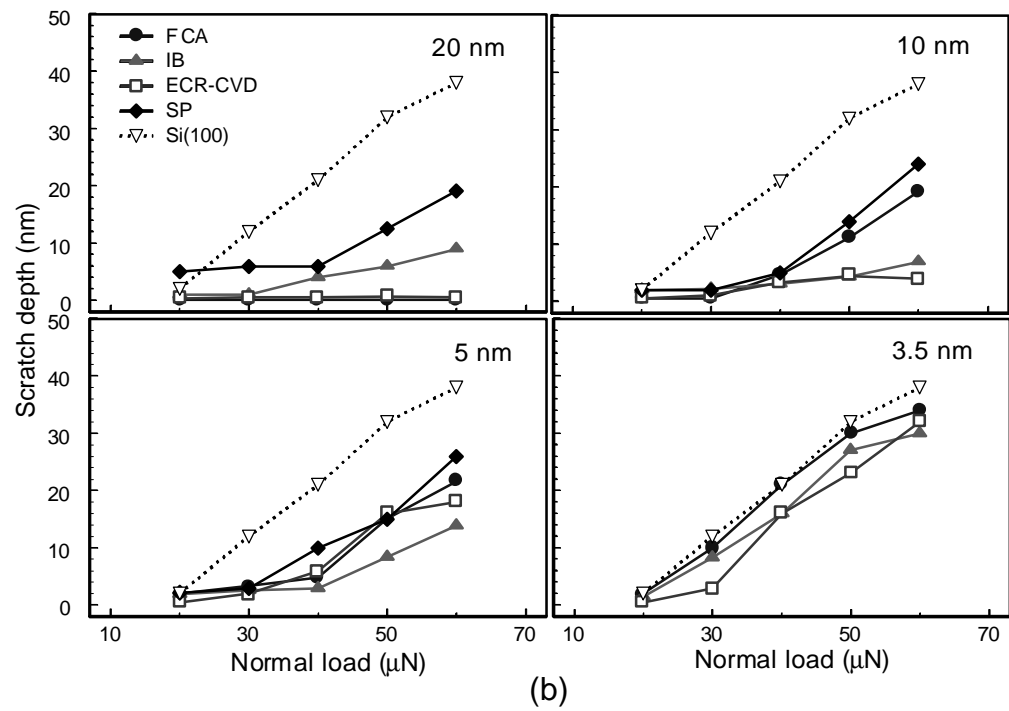
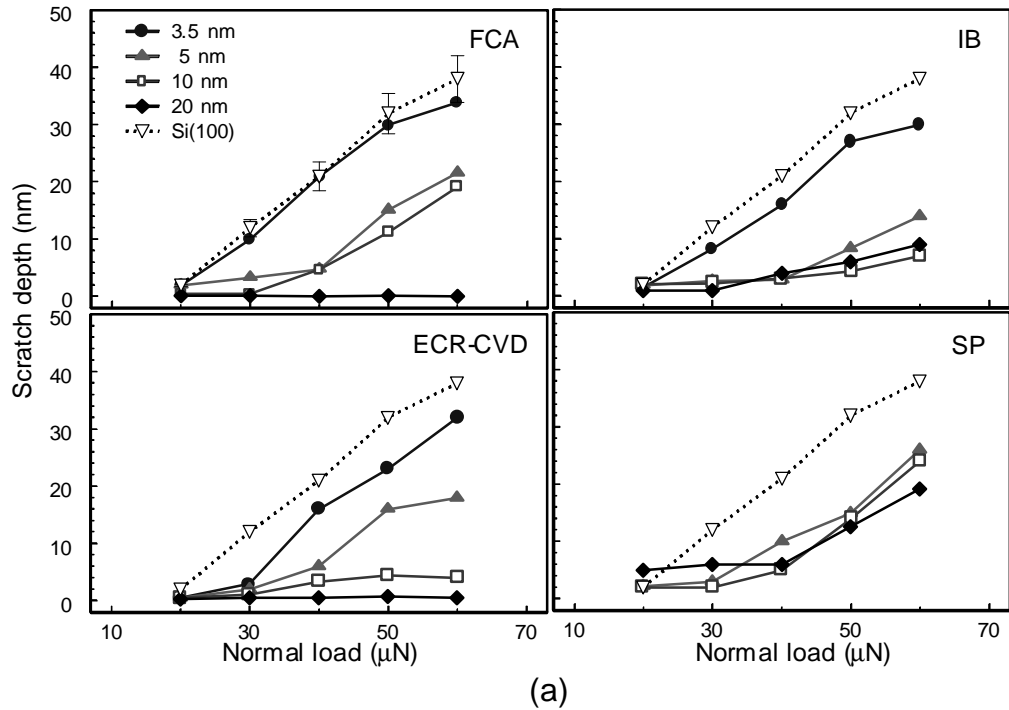


Figure 4.4: Scratch data of the coatings (a) grouped by deposition technique and (b) by coating thickness. FCA – Filtered Cathodic Arc, IB – Ion Beam, ECR-CVD – Electron Cyclotron Resonance Chemical Vapor Deposition, SP – Sputtered.

coating shows poor scratch resistance compared to the others. Also, as coating thickness decreases, FCA shows a distinct decrease in scratch resistance compared to the other coatings. The 3.5 nm coatings do not seem to provide adequate protection to the substrate, though the IB coating appears to be a little better than the rest. Figure 4.5 shows representative AFM images after scratch tests for 10 cycles on FCA and SP coatings. The scratch marks are barely visible on the 20 nm FCA coating, while the 3.5 nm coating shows an increase in scratch depth with normal load. Both IB and ECR-CVD coatings show scratch morphologies similar to the FCA coating. The SP coatings exhibit more debris on the scratch edges.

Figure 4.6(a) shows the wear performance of uncoated Si(100) at two different loads as a function of number of cycles. Figure 4.6(b) shows the wear data for all the DLC coatings. FCA and ECR-CVD 20 nm coatings show excellent wear resistance up to 80 μN , the load that is required for the IB 20 nm coating to fail. In these tests, 'failure' of a coating results when the wear depth exceeds the quoted coating thickness. The SP 20 nm coating fails at the much lower load of 35 μN . At 60 μN , the coating hardly provides any protection. Going on to the 10 nm coatings, ECR-CVD coating requires about 45 cycles at 60 μN to fail as compared to IB and FCA, which fail at 45 μN . The FCA coating exhibits slight roughening in the wear track after the first few cycles, which leads to an increase in the friction force. The SP coating continues to exhibit poor resistance, failing at 20 μN . For the 5 nm coatings, the load required to fail the coatings continues to decrease. But IB and ECR-CVD still provide adequate protection to bare Si(100) in that order, failing at 35 μN compared to FCA at 25 μN and SP at 20 μN . Almost all the 20, 10 and 5 nm coatings provide better wear resistance than bare silicon. At 3.5 nm, FCA coating provides no wear resistance, failing almost instantly at 20 μN . The IB and ECR-CVD coating show good wear resistance at 20 μN compared to bare Si(100). But IB lasts only about 10 cycles and ECR-CVD about 3 cycles at 25 μN .

The wear tests highlight the differences in the coatings more vividly than the scratch tests. At higher thicknesses (20 and 10 nm), the ECR-CVD and FCA coating appear to show the best wear resistance. This is probably due to higher hardness of the coatings (see Table 4.2). At 5 nm, IB coating appears to be the best. FCA coatings show

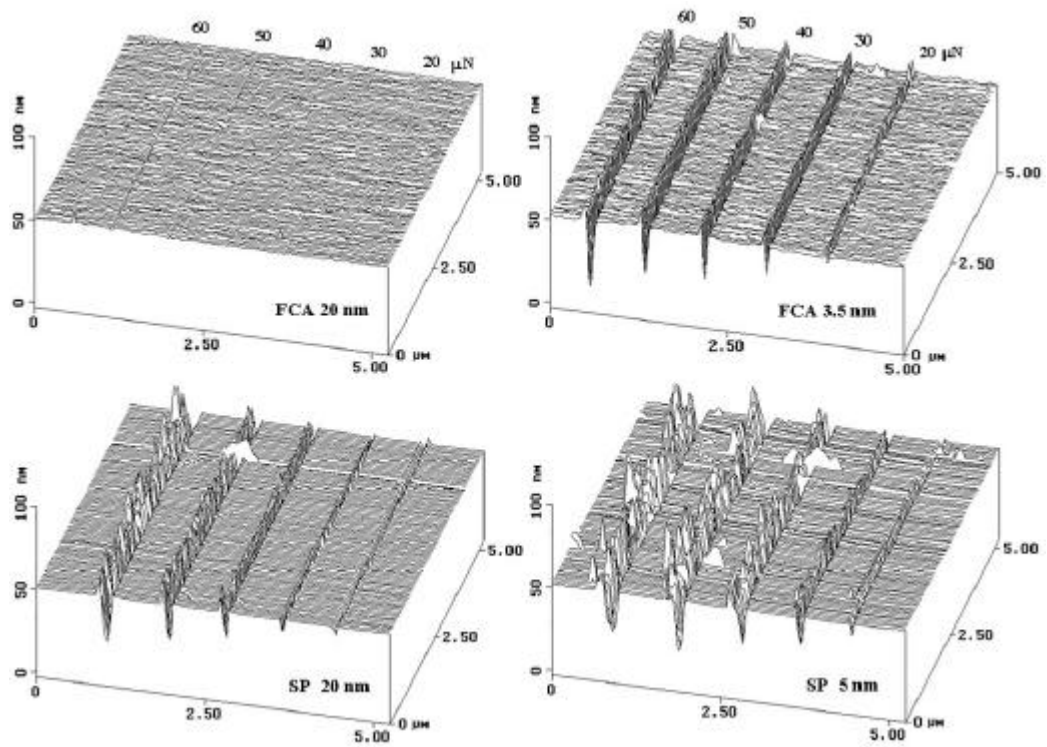


Figure 4.5: AFM 3D images of scratches on FCA and SP coatings.

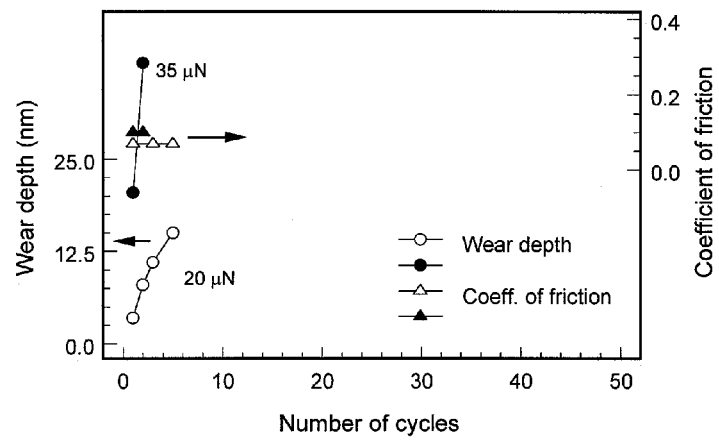


Figure 4.6: (a) Wear data on Si(100).

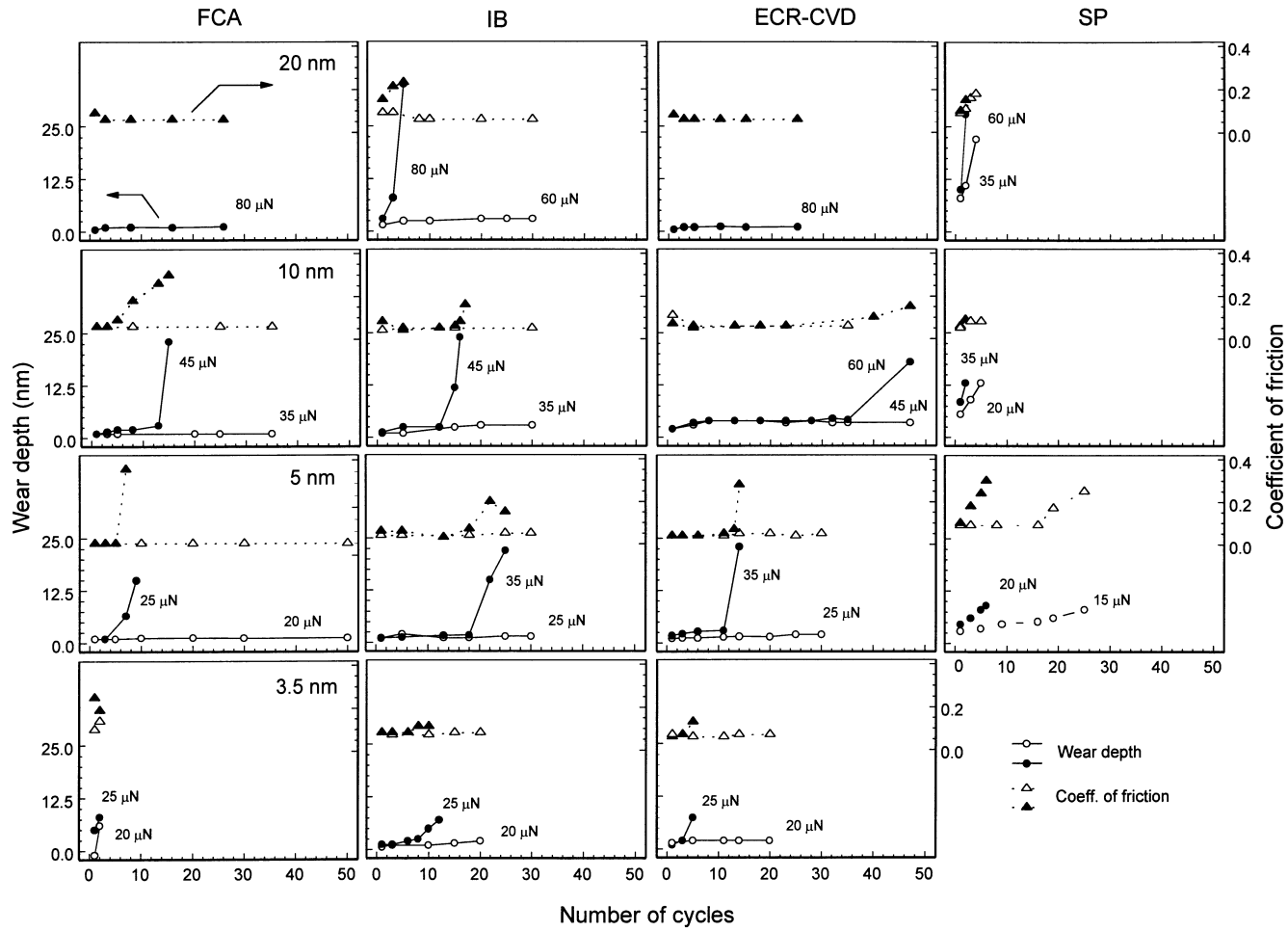


Figure 4.6: (b) Wear data for all DLC coating

poorer wear resistance with decreasing coating thickness. SP coatings showed consistently poor wear resistance at all thicknesses. The IB 3.5 nm coating does provide reasonable wear protection at low loads.

4.4.1.1 Coating failure mechanisms

Figure 4.7(a) shows a wear mark on uncoated Si(100) at 20 μN . Wear occurs uniformly and material is removed layer by layer via ploughing from the first cycle, resulting in the constant friction signal seen during the wear (Fig. 4.7a). Figure 4.7(b) shows AFM images of the wear marks on all 10 nm coatings. It can be seen that only the SP coating wears almost uniformly. This suggests that the SP coatings fail in a manner similar to uncoated Si. This may be due to the low hardness of the SP coating. In the SP coatings, the friction signal increases gradually when the wear depths approach values of the coating thickness. This may be due to the presence of the Si interlayer in the SP coatings.

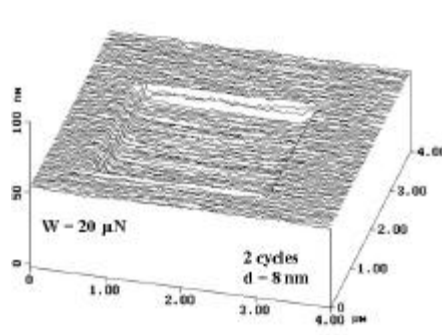


Figure 4.7: (a) AFM 3D image of a wear mark on Si(100).

For FCA, IB and ECR-CVD coatings, at 20, 10 and 5 nm thicknesses, coating failure is sudden and catastrophic and accompanied by a sudden rise in the friction force (Fig. 4.6b). Also, Fig. 4.7(b) indicates that they fail non-uniformly. Another interesting point is that although the coating fails locally and the substrate is exposed, the rest of the coating does not fail on the subsequent cycle. Rather it remains intact for a considerable

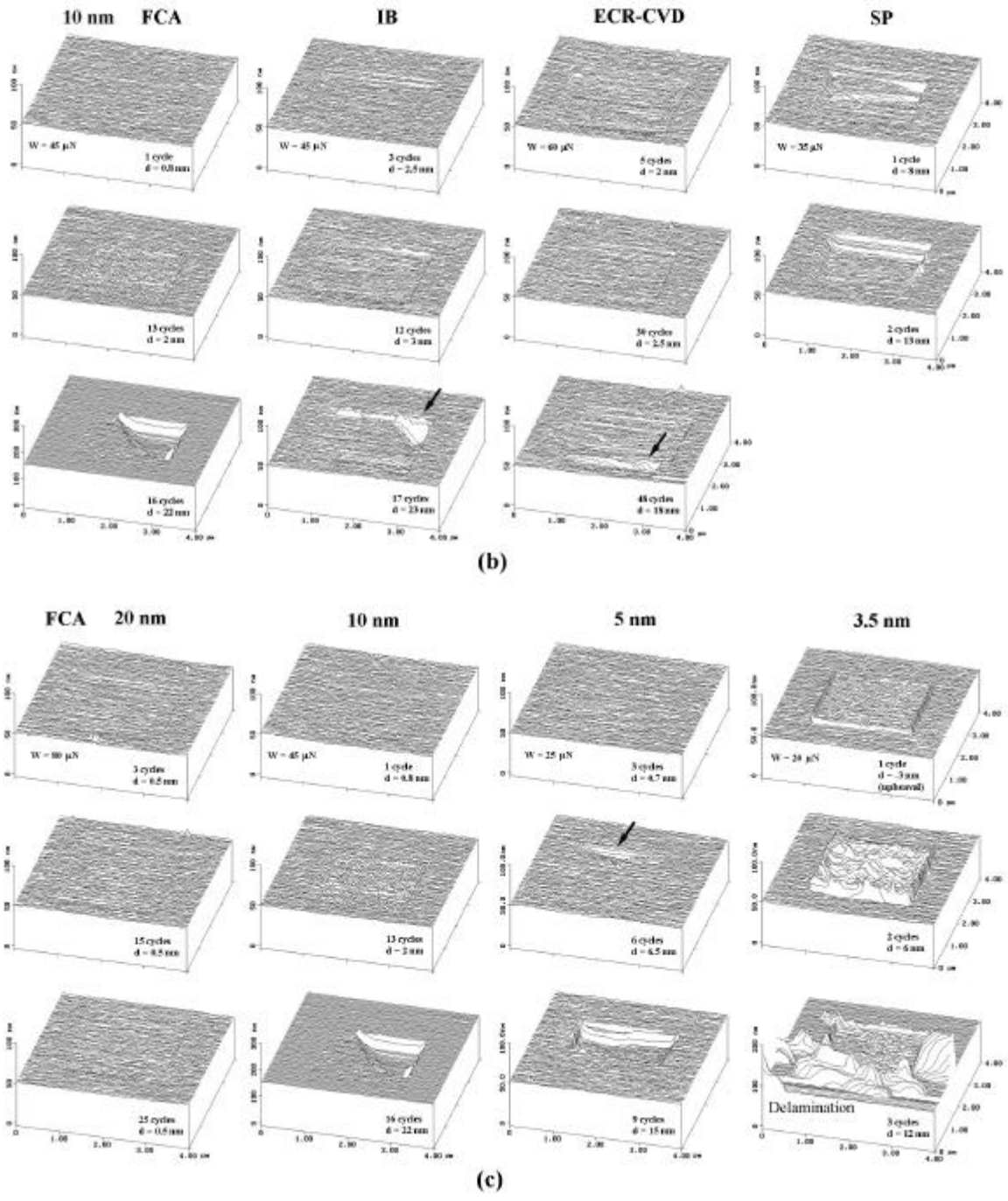


Figure 4.7: (b) AFM 3D images of wear marks for all 10 nm coatings and (c) for all FCA coatings. The arrows indicate regions of sudden failure.

number of cycles past initial failure before the failed region expands into previously intact regions. This shows that all these coatings possess very good adhesion. This is further evidenced by the absence of coating delamination in the vicinity of the wear scar. There are no cracks visible on the surface around the wear region. Prior to failure, negligible wear is seen. In some cases, a 'running in' of the coating surface occurs where any films present are worn away (as indicated by high friction force) and the friction signal settles to a constant value. The sudden failure of the coatings suggests a brittle and/or a fatigue type of failure. The sudden increase in friction force occurs only at the region that is failing, as shown in Fig. 4.8 (FCA coating). The arrow in the figure indicates the boundary between the failed and intact regions. The failed region appears to undergo excessive ploughing that removes the bulk of the coating so that the tip penetrates the substrate. The debris generated is loose since they appear to have been swept from the scan area by the scanning tip (Fig. 4.7b).

The failure mechanism could be similar to that illustrated in Fig. 4.9(a). In the initial cycles, cracks formed beneath the surface extend within the coating upon subsequent cycles (Holmberg and Mathews, 1994). Formation of these cracks depends upon the hardness and fracture toughness of the coating (Holmberg and Mathews, 1994; Kodali et al., 1997). These are controlled by the $sp^3:sp^2$ fraction. The non-uniform failure of the coating suggests that the above properties are not uniform within the coating, as shown in Fig. 4.9(a). Instead a spatial variation in these properties of the coating exists, with the length scales on the order of a fraction of a micron. The weaker regions (with lower fracture toughness) develop the cracks. As the cracks propagate, they are forced to expand within the weak region, as the neighboring strong regions inhibit extensive lateral crack growth, as seen in Fig. 4.9(a). Owing to this, the cracks propagate down to the interface, where aided by the interfacial stresses, they get diverted along the interface just enough to cause local delamination of the coating. When this happens, the weakened region of the coating experiences excessive ploughing, which causes the spike in the friction force (Fig. 4.6b, Fig. 4.8). At this point, the coating fails catastrophically and the tip penetrates the substrate as shown in Fig. 4.9(a). Thus regions with weaker properties fail while the regions with stronger properties remain

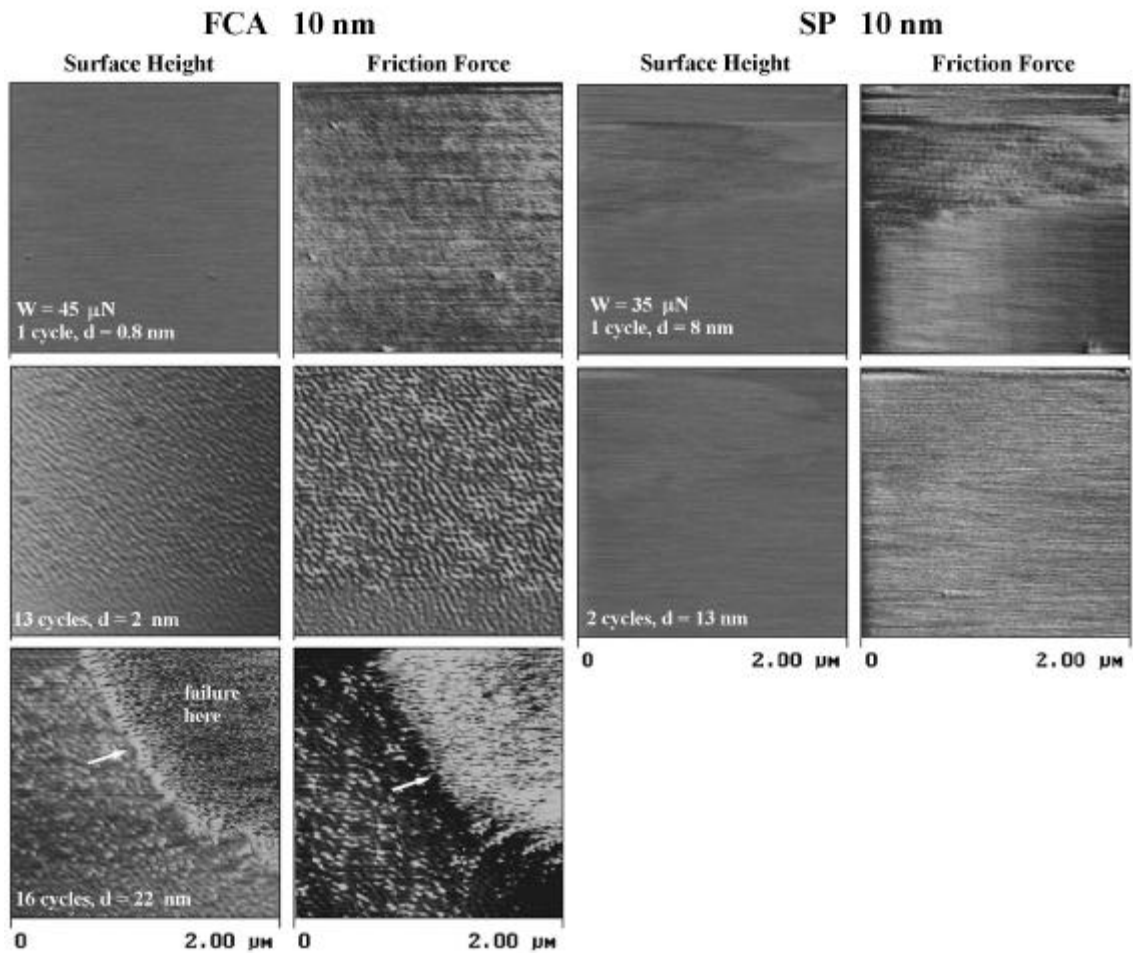


Figure 4.8: 2D Surface height and corresponding friction force maps of FCA and SP 10 nm coatings during wear showing the failure process. Brighter regions correspond to higher surface height and higher friction force in the surface height and friction force images, respectively.

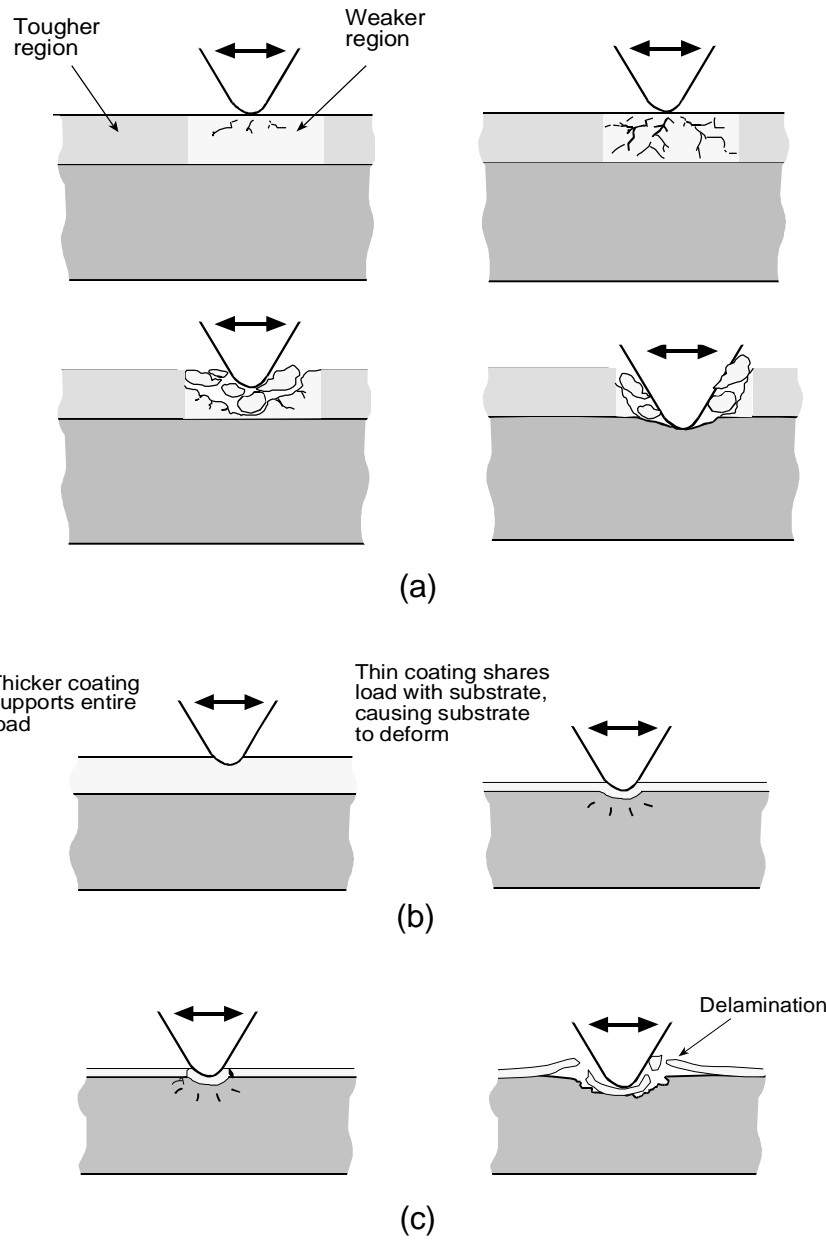


Figure 4.9: Schematics illustrating (a) the suggested failure mechanism of FCA, IB and ECR-CVD coatings at thicknesses of 5 to 20 nm (b) the difference in load -carrying capacities between thick and thin coatings and (c) the suggested failure mechanism of 3.5 nm coatings.

wear-resistant, which is the observed phenomenon. Propagation of cracks along the coating-substrate interface is suppressed due to the excellent adhesion of the coatings as otherwise coating delamination would be observed. The FCA coatings show more spreading of the failed region as compared to the other coatings (Fig. 4.7b,c) and the spread is more in the case of the 5 nm coatings than the 10 nm coating. This suggests that the higher interfacial stresses in the case of FCA coatings (Gupta and Bhushan, 1995a) aid propagation of cracks to some extent and facilitates spreading of the failed region as compared to the other coatings. Based on the trends in elastic modulus of the coatings in Table 4.2, the larger mismatch in elastic modulus between FCA coatings and the silicon substrate might also aid in crack propagation along the interface (Bull, 1995).

All the 3.5 nm coatings, irrespective of the deposition method, failed at low loads compared to the higher thickness coatings. It appears that these thin coatings have very low load-carrying capacity and therefore the substrate undergoes deformation almost immediately, as shown in Fig. 4.9(b). This generates stresses at the interface that weaken the coating adhesion and leads to delamination of the coating in the vicinity of the wear mark as illustrated in Fig. 4.9(c). This may be the reason why large amounts of sticky debris are seen in the 3.5 nm coating in Fig. 4.7(c). Both IB and ECR-CVD also exhibit similar debris, which are not seen in the case of higher thickness coatings. This suggests occurrence of delamination. In the case of the FCA coatings, the interfacial stresses are very high (Gupta and Bhushan, 1995b) and compound the problem of delamination. In addition the larger mismatch of elastic modulus values between the FCA coating and the silicon substrate (Table 4.2) is believed to aid in propagation of cracks along the interface resulting in poorer coatings as the thickness is reduced (Bull, 1995). The friction trace does not increase much during failure for all the 3.5 nm coatings. This indicates that delamination in these thin coatings does not require much energy. An interesting feature in the wear of the FCA coating can be seen in Fig. 4.7(c). After 1 cycle of wear at 20 μN , an upheaval of about 3 nm occurs, that is, it appears that the material has expanded rather than been removed. Similar occurrences have been reported on bare silicon at light loads (DeVecchio and Bhushan, 1998). It has been speculated that this occurs due to phase transformation of silicon under loading (Pharr et al., 1989) or due to the oxidation of

freshly exposed silicon due to rubbing of the AFM tip. The occurrence of this in the FCA coating indicates that the coating is probably not continuous on the microscale at such low thicknesses or that the underlying substrate is being deformed and hence expands to cause the upheaval. 3.5 nm may also be insufficient to produce a coating comprised of a DLC matrix and is instead made up of a matrix characteristic of the interface region where atomic mixing occurs with the substrate and/or any interlayers used. This would also result in poor wear resistance and silicon-like wear behavior of the coating, especially in the case of FCA coatings, which show the worst performance even at 20 μN . ECR-CVD also fails early on at 25 μN , while IB lasted the longest. Both IB and ECR-CVD coatings appeared to last long at 20 μN while FCA coatings fail even at 20 μN . IB and ECR-CVD 3.5 nm coatings, therefore, are able to provide some protection against wear at very low loads.

4.4.2 Continuous microscratch tests

Scratch tests were performed with the normal loads increasing from 1 to 120 μN in 500 increments. A scratch length of 25 μm was used and the speed of the sample relative to the tip was 0.5 $\mu\text{m/s}$. Figure 4.10 shows data from a scratch test on Si(100). The raw friction signal (V) measured at 20 samples per second and applied normal load are plotted as a function of the scratch distance in Fig. 4.10(a). Figure 4.10(b) shows the friction data plotted in the form of coefficient of friction during the scratch test as a function of applied normal load after averaging the friction force values for the corresponding normal load. At the beginning of the scratch, the coefficient of friction is low, around 0.04, which is typical of AFM-based friction measurements on Si(100). At about 35 μN , indicated by the arrow in Fig. 4.10(b), there is a sharp increase in the coefficient of friction. The normal load associated with this event is termed the critical load. The friction data obtained is comparable to results reported by others on silicon using the Nanoindenter (Gupta and Bhushan, 1995a; Bhushan and Li, 1997). Figure 4.10(c) shows the tapping mode AFM surface height image of the scratch. It can be seen that at the critical load, a clear groove starts to form. This implies that Si(100) was damaged by ploughing at the critical load, associated with the plastic flow of the material.

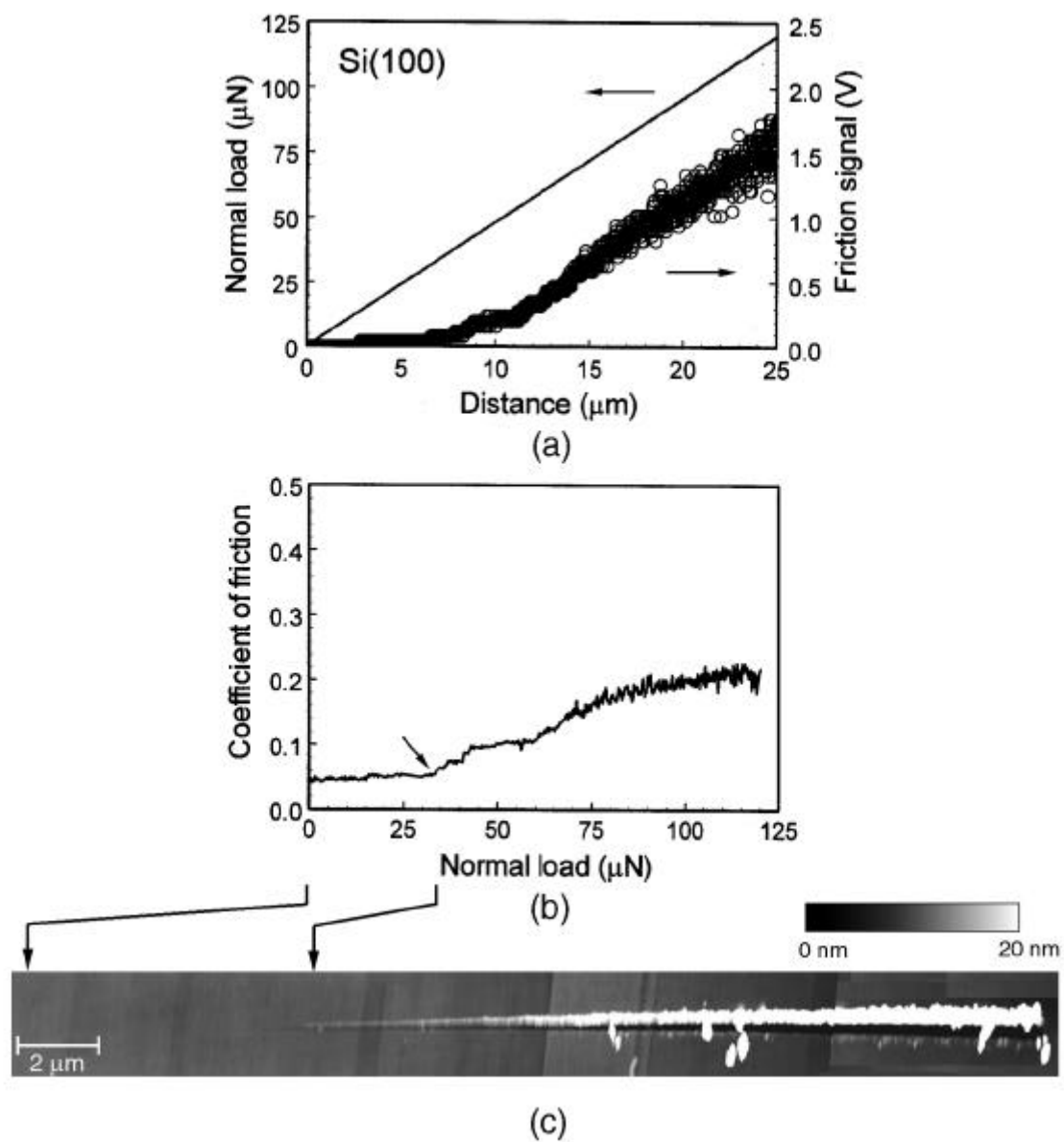


Figure 4.10: (a) Applied normal load and friction signal measured during a continuous microscratch experiment on Si(100) as a function of scratch distance. (b) Friction data averaged for a given normal load and plotted in the form of coefficient of friction as a function of normal load and (c) AFM surface height image of scratch obtained in tapping mode.

This is in agreement with the deformation mechanisms of silicon at similar loads reported previously (Zhao and Bhushan, 1998). At and after the critical load, small and uniform debris is observed and the amount of debris increases with increasing normal load. It can be seen in Fig. 4.10(c) that the debris is not symmetrically distributed about the scratch groove. This is due to the asymmetry of the tip shape about the scratch direction (Appendix A.4 shows gives details of the tips). The front side, which is at an angle of about 30° off long axis of the cantilever, pushed most of the cut materials and debris away onto the front side of the scratch. Contact mode images of the scratch resulted in large portions of the debris being swept out of the scanned region making it difficult to locate onset of debris generation. Tapping mode imaging minimizes loss of debris and other damage indicators compared to contact mode imaging.

In this study, scratches were generated along several different directions on the sample. No significant change in critical load was observed. It must be noted that a native silicon oxide layer is usually present (thickness ~ 1 nm) which may affect the occurrence of the observed critical load for silicon. This oxide layer can also undermine any dependence of critical load to the crystallographic direction of the scratch.

Figure 4.11 shows coefficient of friction profiles as a function of increasing normal load and corresponding AFM surface height images of the scratches made on the various DLC coatings. It can be seen that there exists a well-defined critical load for each coating (indicated by the arrows labeled 'A'). At the initial stages of the scratch, all the coatings exhibit a low coefficient of friction of 0.04 – 0.06 (comparable to that for silicon) indicating that the friction force is dominated by the shear component. This is in agreement with analysis of the AFM images, which shows negligible damage to the coating prior to the critical load. At the critical load, a clear groove is formed, which is accompanied by formation of material pile-up at the sides of the scratch. This suggests that initial coating damage that occurs at the critical load is due to increased ploughing associated with plastic deformation. The sudden increase in the ploughing component of the friction force causes the sharp rise in the coefficient of friction. Beyond the critical load, debris (chips) can be seen in addition to material pile-up at the sides of the scratch. This may be due to coating spallation or delamination. Further analysis of the AFM

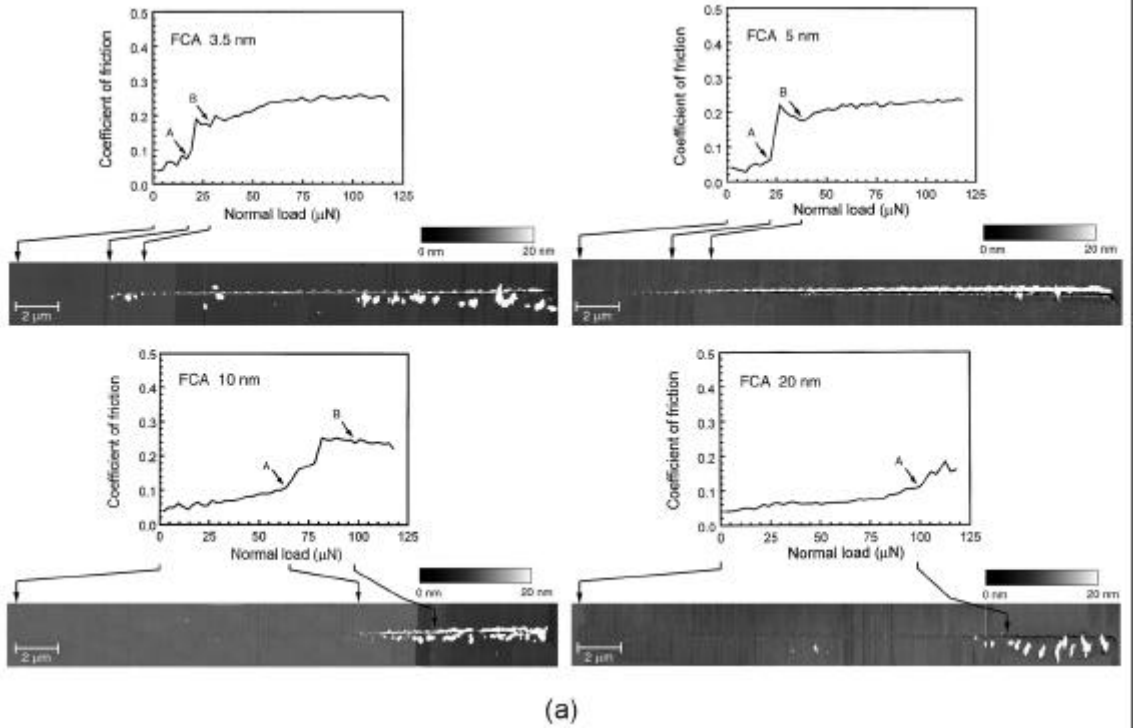
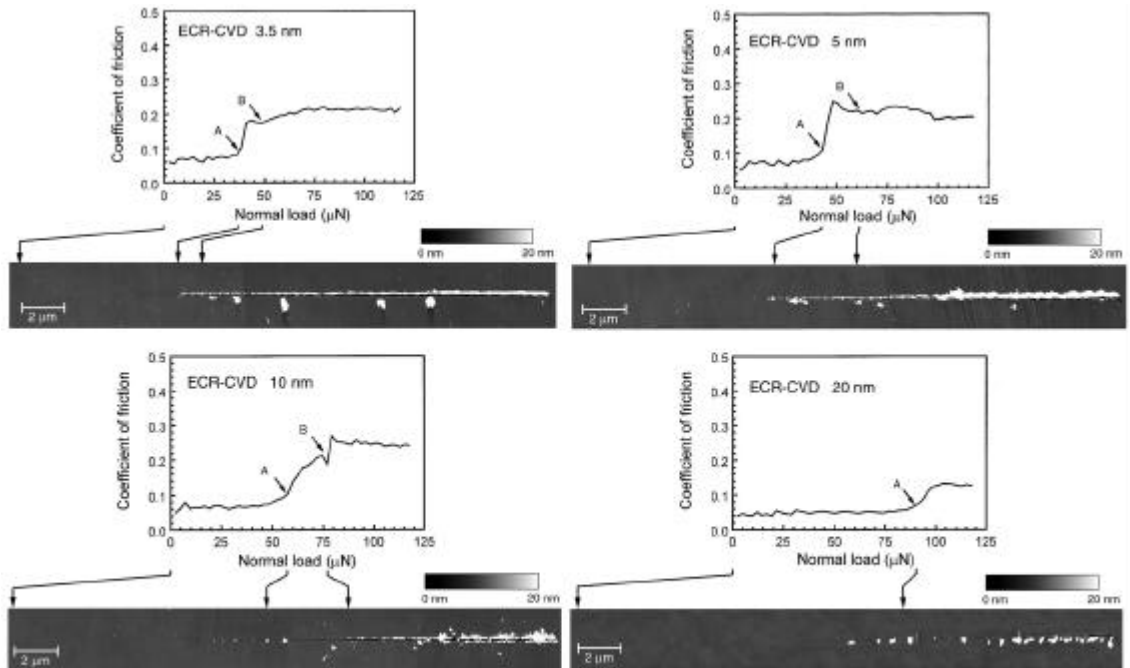
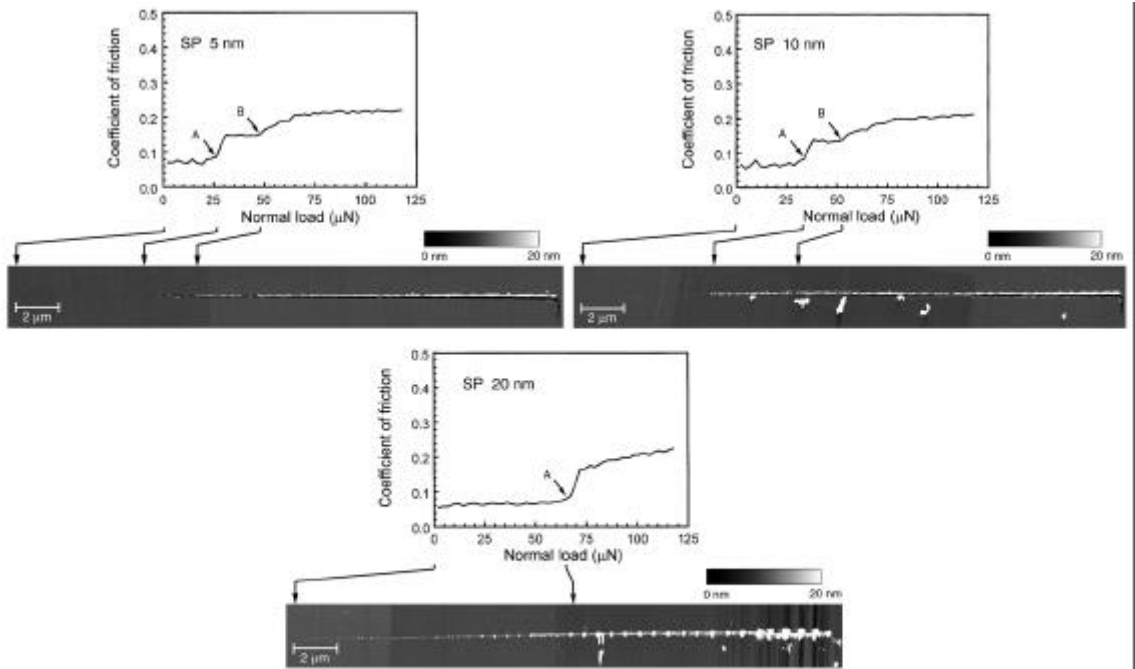


Figure 4.11: Coefficient of friction profiles during scratch as a function of normal load and corresponding AFM surface height images for (a) FCA, (b) ECR -CVD and (c) SP coatings.

Figure 4.11 (continued)



(b)



(c)

images reveals the location where the residual scratch depth first exceeds the coating thickness (indicated by the arrows marked 'B' in Fig. 4.11). In the case of the 20 nm coatings, the maximum scratch depth did not exceed the coating thickness indicating that at this thickness, the load-carrying capacity of the coatings is in excess of the range used. For the thinner coatings, this event occurs right after the occurrence of the critical load and is accompanied by a slight increase in the coefficient of friction.

In this study, wear of the diamond tip was monitored by periodically generating a scratch at 50 μN normal load on Si(100) and comparing scratch depths between successive tests. A significant variation in a scratch depth value from the previously measured scratch depth would indicate a significant wear of the tip. The variation of these scratch depths during the course of experiments remained under 3 nm (12%) compared to the initial scratch depth of about 20 nm. Hence the wear of the tip was not a major cause for concern in continuous microscratch study, in contrast with the previous studies with multiple cycles.

Figure 4.12(a) summarizes the critical loads for the various coatings obtained in this study. It is clear that for all deposition methods, the critical load increases with increasing coating thickness due to better load-carrying capacity of thicker coatings as compared to the thinner ones. For FCA and ECR-CVD coatings, 3.5 and 5 nm coatings do not show a large difference in the critical load and exhibit much lower values than for 10 and 20 nm thick coatings. In the case of SP coatings, 5 and 10 nm coatings show comparable critical loads that are much lower than that of the 20 nm coating. Comparing the different deposition methods, ECR-CVD and FCA coatings show superior scratch resistance at 20 and 10 nm thicknesses compared to SP coating. As the coating thickness reduces, ECR-CVD exhibits the best scratch resistance followed by FCA and SP coatings.

Figure 4.12(b) shows critical loads for the various coatings estimated from a microscratch technique performed using a Nanoindenter (Li and Bhushan, 1999) with a conical diamond tip (radius $\sim 1 \mu\text{m}$). It can be seen that in general, the trend in critical loads between the various coatings as measured by the two techniques are similar, although values of critical loads obtained with the sharper Berkovich tip

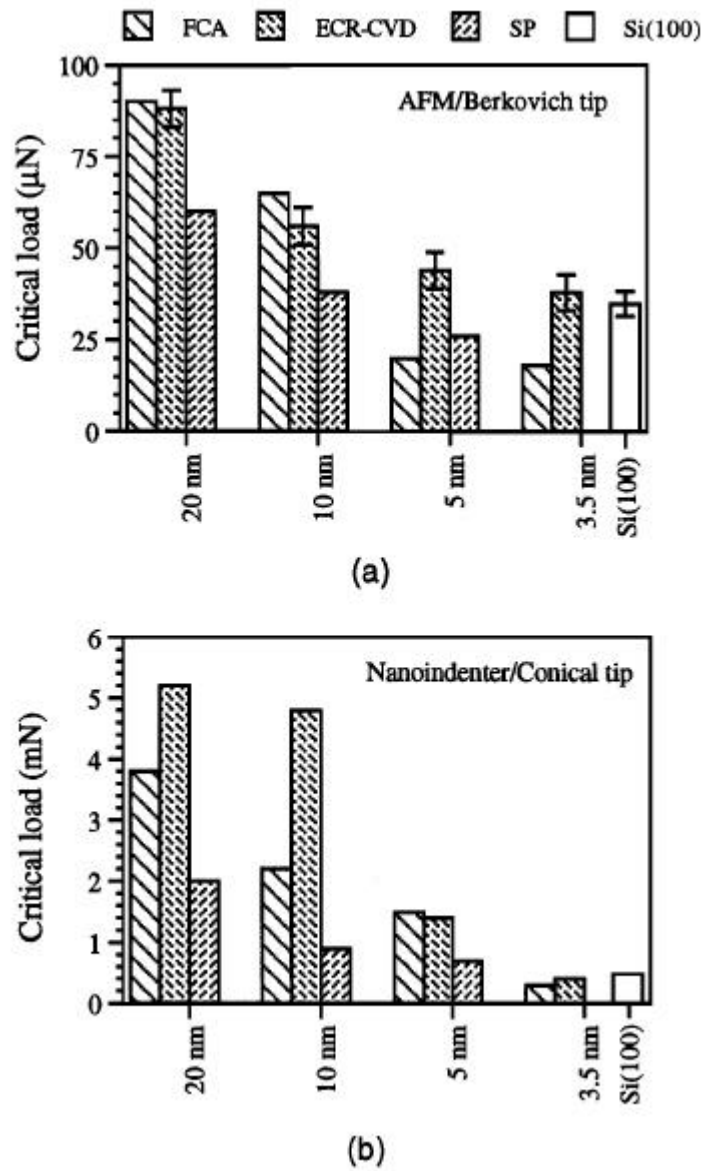


Figure 4.12: (a) Critical loads estimated from the coefficient of friction profiles and AFM images for the various coatings. (b) Critical loads estimated from continuous scratch tests using a Nanoindenter for the various coatings.

(radius ~ 100 nm) in the AFM are much lower than those obtained with the Nanoindenter. This is because the AFM tip has a sharp front edge, which generates a high stress concentration in the coating in the front of the tip, whereas the nanoindenter tip has a round side facing the coating, leading to a relatively uniform stress distribution in the coating in the front of the tip. During scratch, the AFM tip cut the coating whereas the nanoindenter tip pushed the coating. Consequently, the critical loads obtained with the AFM tip are lower than those with the nanoindenter tip. Considering the tip radius effect, the nanoindenter tip is ten times more blunt than the AFM tip and so the critical loads for the AFM tip should be much lower than that for the nanoindenter tip. Some differences are seen for the 10 and 20 nm ECR-CVD coatings, which are probably due to the difference in stress distribution caused by different tip geometry. Figure 4.12 demonstrates that the scratch technique described in this study yields comparable trends with that reported using a commonly used Nanoindenter.

Figure 4.13 shows the normal loads for the various coatings at which the residual depth as measured from the AFM images first exceeds the corresponding coatings thickness. It can be seen that this load increases with coating thickness, exhibiting the same trend as the critical loads. This is expected as a thicker coating in general will require a greater load before the coating is worn through.

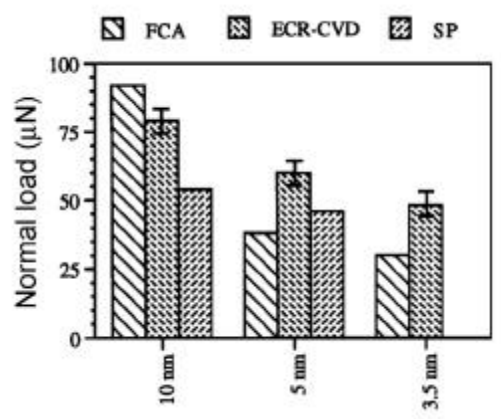


Figure 4.13: Normal loads at which the residual depth of the scratches as measured using the AFM first exceeds the coating thickness for the various coatings.

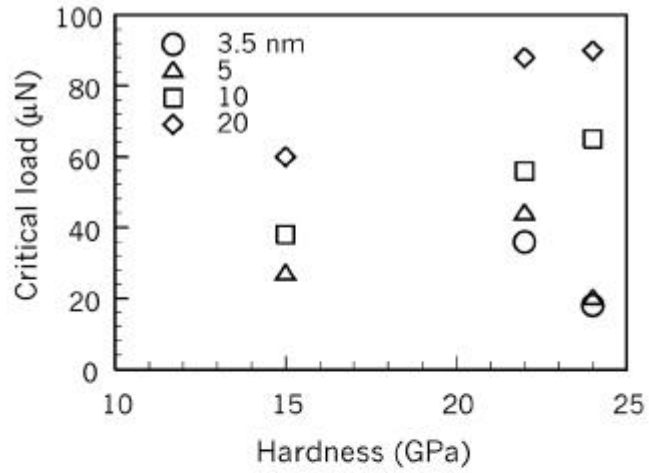
4.4.2.1 Coating failure mechanisms

Since at the critical load, the damage mechanism appears to be onset of ploughing, higher hardness and fracture toughness of a coating will therefore result in higher load required for deformation and hence higher critical load. Figure 4.14 shows critical loads of the various coatings as a function of the coating hardness and fracture toughness (from Table 4.2). It can be seen that in general, higher coating hardness and fracture toughness result in higher critical load. The only exceptions are the FCA coatings at 5 and 3.5 nm coating thickness, which show the lowest critical loads despite their high hardness and fracture toughness. The brittleness of the thinner FCA coatings may be one reason for their low critical loads. The mechanical properties of coatings that are less than 10 nm thick are unknown. The FCA process may result in coatings with low hardness at such low thickness due to differences in coating stoichiometry and structure as compared to the coatings of higher thickness. Also, at these thicknesses stresses at the coating-substrate interface may affect adhesion and load-carrying capacity of the coatings. Coatings with higher interfacial and residual stresses are more easily delaminated. A previous study shows that FCA coatings have much higher residual stresses compared to the other coatings (Gupta and Bhushan, 1995a). In addition, a large mismatch between the elastic modulus values of the FCA coating and the silicon substrate (Table 4.2) may result in high interfacial stresses (Sullivan and King, 1988; Gupta and Bhushan, 1995b). This may be why thinner FCA coatings show relatively lower critical loads compared to the other coatings. Differences in RMS roughness between the coatings are very small and can be considered to have no effect on the critical loads observed.

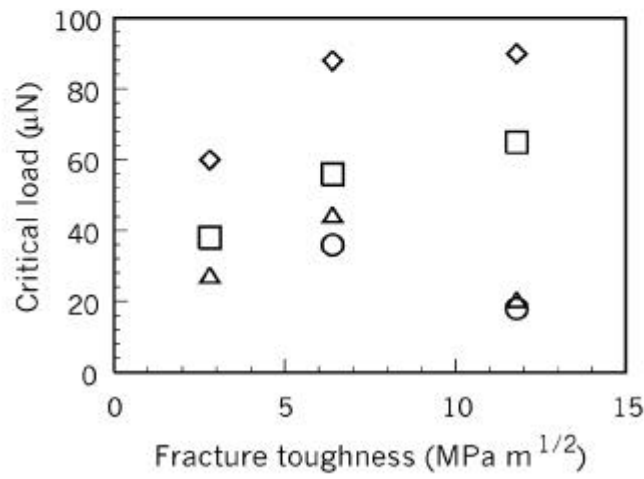
Hence a combination of high hardness, fracture toughness and a good match in elastic modulus values between coating and substrate appear to result in superior scratch resistance for ultra-thin coatings.

4.4.3 Surface analysis of coatings

One possible reason for the non-uniform failure of the coatings seen in Fig. 4.8 may be due to poor coverage of the coating on the substrate. Surface analysis of the



(a)



(b)

Figure 4.14: Variation of observed critical loads as a function of (a) coating hardness and (b) fracture toughness.

carbon coatings were conducted using X-ray photoelectron spectroscopy (XPS) using a VG Scientific ESCA LAB MARK II. A twin anode Mg anode was used as the X-Ray source at 280 W (14 keV and 0.02 A). Measurements were made at a single spot of 1300 μm diameter on three different locations of a sample at a sampling depth of 5 nm. The results of XPS analysis on all the coating surfaces are shown in Fig. 4.15 while representative XPS spectra of selected samples are shown in Fig. 4.16(a).

The poor SP coatings all show much less carbon content ($< 75\%$ atomic concentration) as did the poor 5 nm and 3.5 nm FCA coatings ($< 60\%$) as compared to the IB and ECR-CVD coatings. Silicon was detected in all 5 nm coatings. From the data it was hard to say if the Si is from the substrate or from exposed regions due to coating discontinuity. Based on the sampling depth any Si detected in 3.5 nm coatings would likely be from the substrate. The other interesting observation is that all the poor coatings (all SP and FCA 5 and 3.5 nm) show almost twice the oxygen content of the other coatings. Further investigations are required before any conclusions can be made regarding the difference in oxygen content.

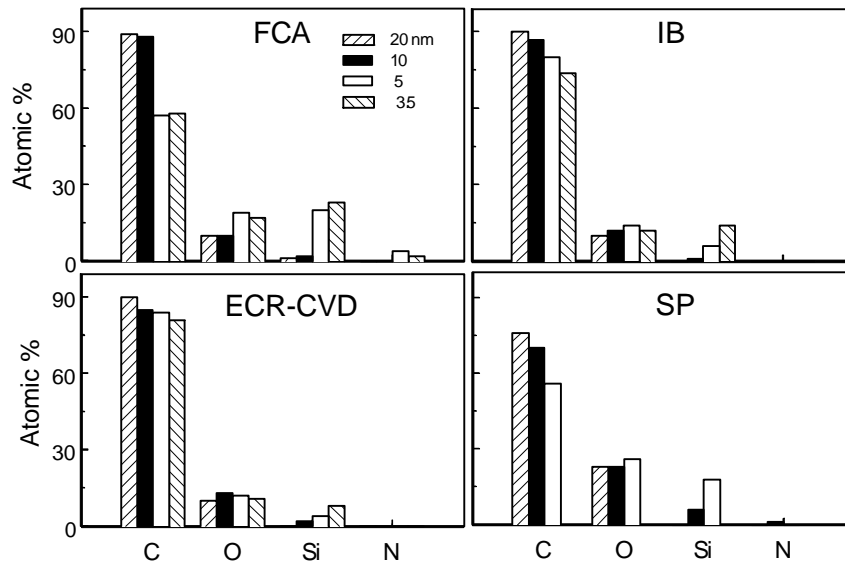
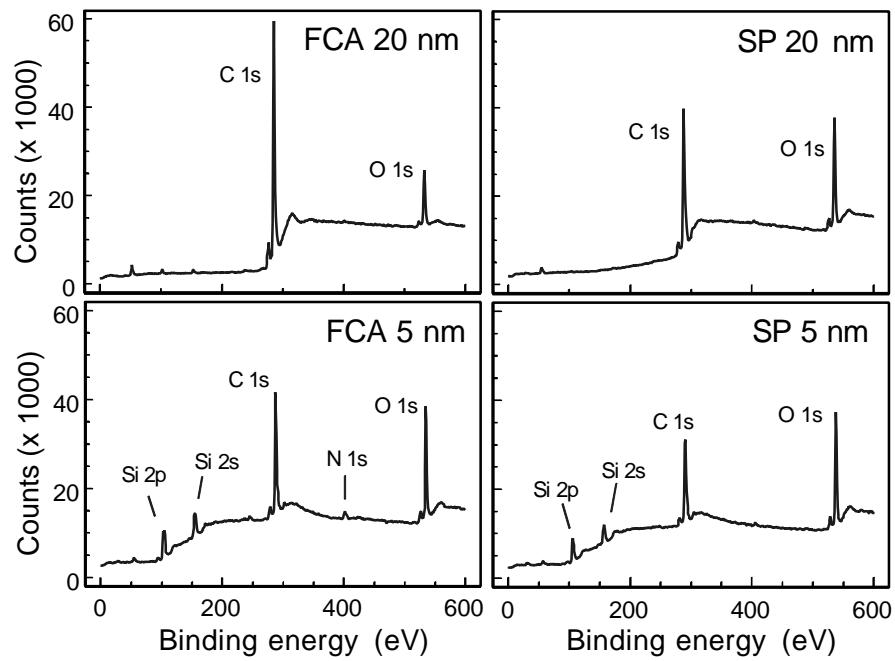
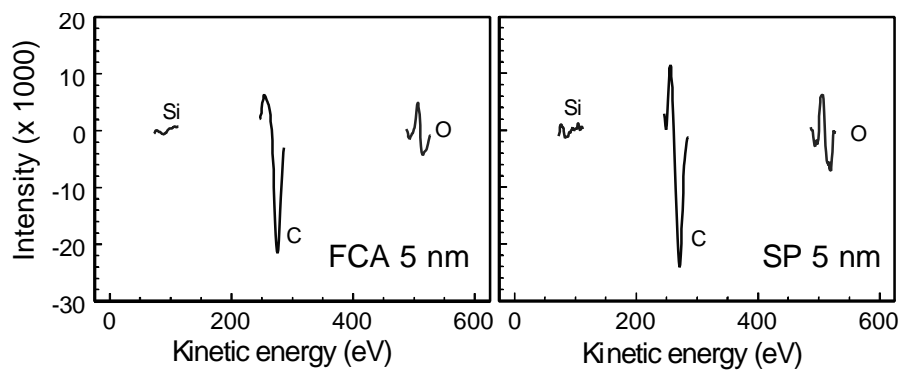


Figure 4.15: Quantified XPS data for all the coatings. Atomic concentrations are shown.



(a)



(b)

Figure 4.16: (a) XPS spectra for FCA and SP coatings at 5 nm and 20 nm coating thicknesses and (b) AES spectra for FCA and SP coatings at 5 nm thickness.

Auger electron spectroscopy (AES) was also performed on selected coatings using a Physical Electronics 680 scanning Auger nanoprobe. The analyses were performed at an accelerating voltage of 10 kV and a probe current of 10 nA. For each experiment, six random regions on the sample surface were selected for analysis. At each region a scan area of 30 μm x 30 μm was rastered with a beam diameter of about 25 nm while the analyzer averaged over the area. Representative spectra of selected samples are shown in Fig. 4.16(b). The results showed very little silicon and the detected peaks were characteristic of oxides. This is in contrast to the XPS measurements on a larger scale and suggests that the coating possesses discontinuities at isolated areas only and that the 5 nm coatings are generally continuous on the microscale.

4.5 Summary

The scratch and wear resistance properties of ultra-thin DLC coatings were studied using an AFM for use in MEMS and magnetic storage media. A continuous microscratch technique to study scratch resistance of such thin coatings using an AFM was also developed.

- The continuous microscratch technique developed using the AFM yielded useful information on critical loads and initial failure mechanisms of the coatings.
- For both bare silicon and the coatings, the onset of ploughing, associated with plastic deformation, was the failure mechanism at the critical load.
- Critical loads were found to be directly proportional to the hardness and fracture toughness of the coatings.
- For coatings less than 5 nm thick, the deformation zones extended into the substrate and a good match of elastic properties between the coating and substrate resulted in higher load carrying capacity.
- Some non-uniform failure of the coatings were observed suggesting non-uniformity in coating properties.
- Based on these studies, it was concluded that ECR-CVD coatings generally showed the best scratch/wear performance due to its high hardness, fracture toughness and

good matching of elastic modulus with the silicon substrate. SP coatings generally showed the poorest scratch/wear resistance because of their low hardness.

- A thickness of 5 nm appears adequate for scratch/wear resistance (especially ECR - CVD) while 3.5 nm is too thin to be used as protective overcoats.

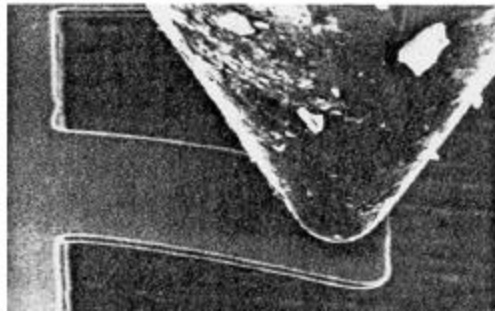
CHAPTER 5

MECHANICAL PROPERTIES OF NANOSCALE STRUCTURES

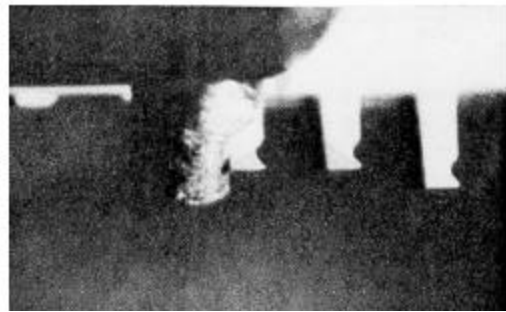
5.1 Introduction and literature review

As was mentioned in Chapter 1, it is essential for designers of MEMS/NEMS to have mechanical property information on the nanoscale, as most mechanical properties are known to exhibit a dependence on specimen size (Gane and Cox, 1970; Sargent, 1986; Bhushan et al., 1996). Mechanical property evaluation of nanometer -scale structures is therefore necessary to help design reliable MEMS/NEMS since good mechanical properties are of critical importance to such applications.

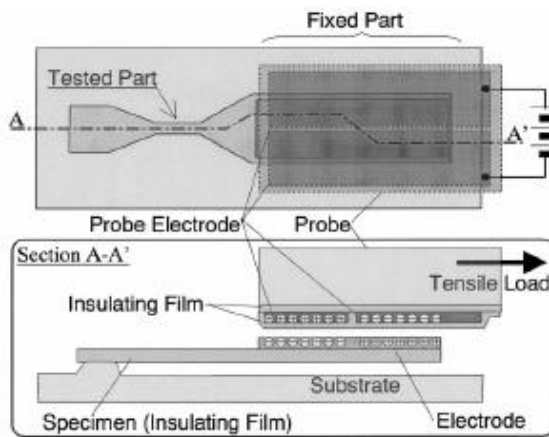
Single-crystal silicon and silicon -based materials are the most common materials used in MEMS. An early study showed silicon to be a mechanically resilient material in addition to its favorable electronic properties (Petersen, 1982). Several researchers have conducted studies to evaluate fracture strengths and elastic modulus of silicon and silicon-based millimeter to micrometer scale structures via tensile tests and bending tests (Johansson et al., 1988; Ericson and Schweitz, 1990; Wilson et al., 1996; Wilson and Beck, 1996; Sharpe et al., 1997; Sato et al., 1998; Greek et al., 1999; Tsuchiya et al., 1998, 2000). These techniques used a Nanoindenter or similar probe to bend microscale cantilever beams (Ericson and Schweitz, 1990; Wilson et al., 1996; Wilson and Beck, 1996) or utilized specially fabricated MEMS structures to apply an electrostatic load to microscale specimens that are integrated into the test structure (Tsuchiya et al., 1998) as shown in Fig. 5.1. Researchers have also studied effect of surface roughness and crystal orientation on the fracture strength of Si microbeams (Ericson and Schweitz, 1990; Wilson et al., 1996; Wilson and Beck, 1996).



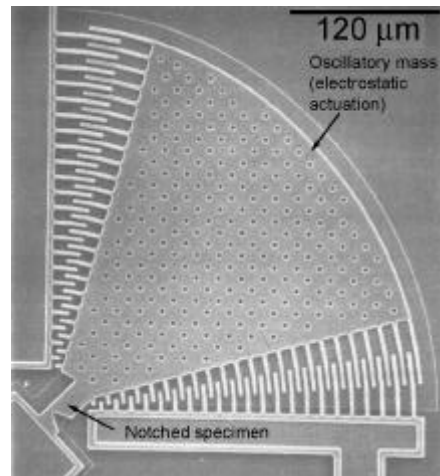
Bending of silicon microcantilevers using a nanoindenter (Ericson and Schweitz, 1990) to obtain fracture strength.



Instrument to apply side -loads to silicon microcantilevers (Wilson and Beck, 1996) to obtain fracture strength.



Microfabricated test structure to evaluate elastic modulus, tensile strength and fracture toughness of microscale parts 'on -chip' (Tsuchiya et al., 2000)



Microfabricated test structure with 'on-chip' specimen to evaluate fracture toughness and fatigue properties (Muhlstein and Brown, in Bhushan, 1998)

Figure 5.1: Techniques developed by other researchers to measure elastic modulus, fracture strength and fracture toughness of microscale specimens.

Fracture toughness is another important parameter for brittle materials such as silicon. Several studies have been conducted to measure fracture toughness of microscale silicon-based (Johansson et al., 1989; Ballarini et al., 1997; Kahn et al., 1999; Fitzgerald et al., 2000) and SiO₂ (Tsuchiya et al., 2000) structures (Fig. 5.1). These studies have shown values that are sometimes higher than, but mostly comparable to bulk values. The literature does not contain reports of fracture toughness of nanoscale structures. It would be of interest to see how fracture toughness on the nanoscale compares with the values obtained on the micro- and macroscales.

In addition to the properties mentioned so far, fatigue properties (such as fatigue strength) of nanostructures are also of interest. This is especially true for MEMS/NEMS involving vibrating structures such as oscillators and comb drives (Nguyen and Howe, 1999). Very few studies exist on fatigue studies of structures relevant to MEMS (Connally and Brown, 1993; Komai et al., 1998; Kahn et al., 1999) and these are on specimens larger than several hundred micrometers along one dimension.

Studies on nanoscale-sized structures are lacking primarily due to difficulties in fabrication of such small-scale test specimens and problems associated with measuring ultra-small physical phenomena in such experiments. Researchers have very recently utilized the atomic force microscope (AFM) for the purpose of measuring elastic modulus and bending strength of silicon nanostructures (Namazu et al., 2000). Building upon their study, the research efforts described in this chapter are aimed at characterizing various mechanical properties of *nanoscale* structures.

In this study, a method to conduct bending tests of fixed nanoscale beams (nanobeams) using an atomic force microscope was developed (Sundararajan et al., 2002). The nanoscale beams were fabricated by means of field-enhanced anodization, also using an AFM as part of a lithography-based process. The samples were fabricated by Prof. Isono's group at Ritsumeikan University in Japan (see acknowledgments). The bending test technique was used to determine elastic modulus and breaking stress (bending strength) of nanoscale beams made of single crystal silicon and SiO₂. These values were compared against the values obtained by other researchers on larger (microscale) specimens.

A method to estimate nanoscale fracture toughness of the beam materials was also developed (Sundararajan and Bhushan, 2002). In addition to bending tests, a technique to study the fatigue performance of nanobeams under monotonic cyclic loading was developed. Such studies to determine fracture toughness and fatigue characteristics of nanoscale structures do not exist in the literature and this study appears to be one of the first to do so. SEM observations of the fracture surfaces were utilized to help understand the failure of the beam materials under bending and fatigue.

5.2 Experimental Procedure

5.2.1 Fabrication of nanometer-scale specimens

Single-crystal silicon fixed nanobeams were fabricated by bulk micromachining incorporating enhanced-field anodization using an AFM (Seiko Instruments Inc., SPA - 300HV) on a (001) plane of an Si wafer separated by implanted oxygen (SIMOX). Figure 5.2 schematically describes the fabrication process of the Si nanobeams. The trench (width of 6 μm) is first etched from the underside after which the top SiO_2 layer is etched to expose the Si diaphragm. A line of silicon dioxide (SiO_2) film with a width of less than 1 μm is deposited by field-enhanced anodization (Snow and Campbell, 1994; Hattori et al., 1994) on the Si surface. This SiO_2 film was used as a high-precision mask pattern for anisotropic wet etching with a solution of 20% tetra-methyl ammonium hydroxide (TMAH). It was then possible to fabricate a nanometer scale Si structure after etching. The line pattern of SiO_2 film was drawn by applying a bias voltage between an Au-coated cantilever/tip and the Si diaphragm in air at room temperature. In this study, a bias voltage of 20 V and a cantilever speed of 0.4 $\mu\text{m/s}$ were selected, which resulted in smooth film lines as well as a film thickness higher than the 4 nm required for reliable TMAH wet etching of the Si interface on the (001) plane (Tabata et al., 1992). The Si diaphragm had an average thickness of 255 nm and hence this is the average thickness of the Si beams.

Once the Si beams are fabricated, subsequent thermal oxidation of the beam samples results in formation of an oxide layer that is about 1 μm thick. This results in the

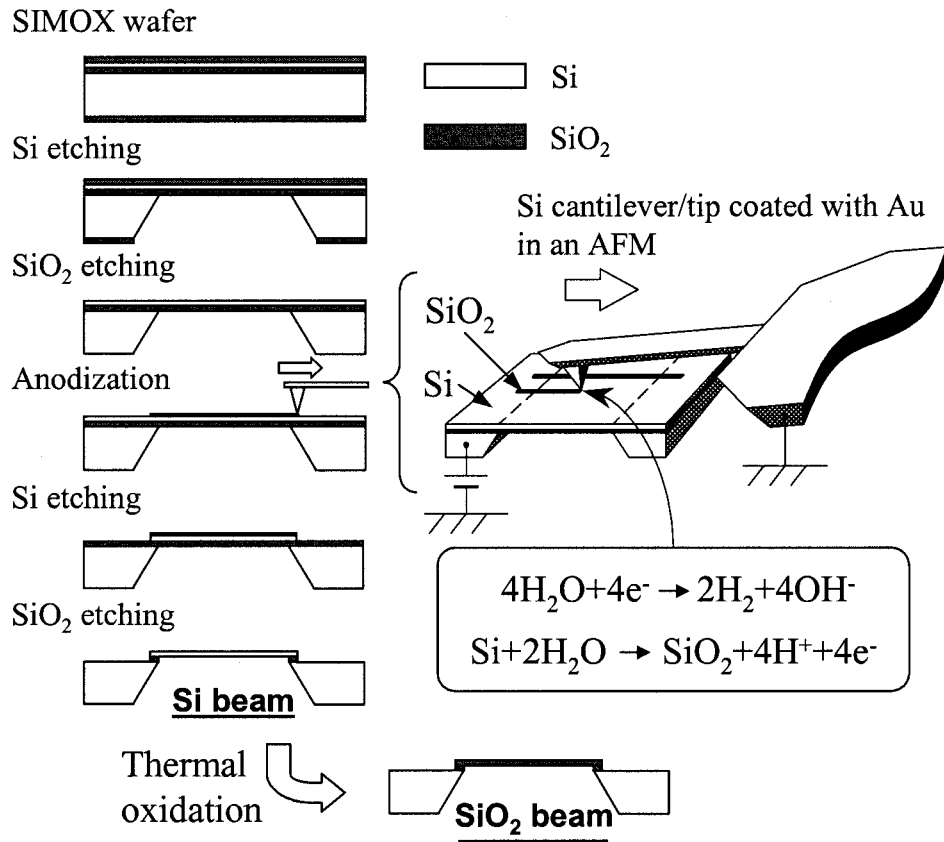
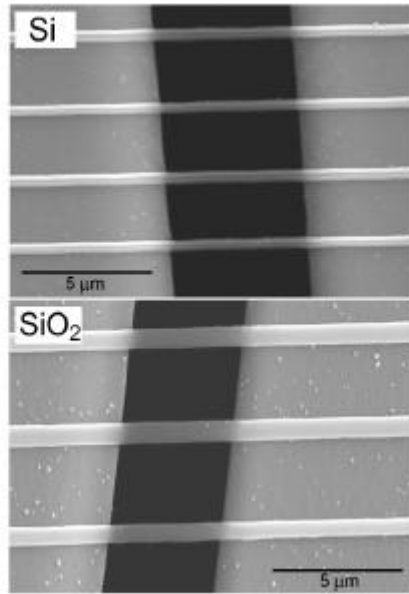
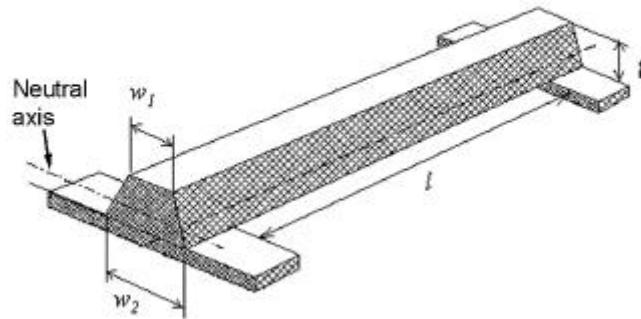


Figure 5.2: Schematic of fabrication process of nanoscale silicon beams. SiO₂ beams are fabricated from the silicon beams by thermal oxidation as indicated in the final step.



(a)



(b)

Figure 5.3: (a) SEM micrographs of nanobeam specimens and (b) a schematic of the shape of a typical nanobeam. The trapezoidal cross-section is due to the anisotropic wet etching during the fabrication. Typical dimensions are given in Table 5.1.

formation of SiO₂ beams. The average thickness of the SiO₂ beams is 425 nm. Figure 5.3 shows SEM images of Si and SiO₂ nanobeams as well as a schematic of a typical nanobeam. The Si beams are oriented along the [110] direction in the (001) plane. The cross section of the beams is trapezoidal owing to the anisotropic wet etching process. The cross section for the beams exhibits a small amount of curvature as compared to the relatively well-defined trapezoidal shape of the Si beams due to the oxidation process. In this study, we have approximated the cross-section of the SiO₂ beams to be trapezoidal as well. The SiO₂ beams also display a little curvature along the length due to thermal stresses generated during the oxidation process. The nominal dimensions of the nanobeams are listed in Table 5.1. The actual width, length and thickness values of the beams were measured using an AFM (within $\pm 5\%$ error) in tapping mode prior to the tests. Surface roughness measurements of the beam surfaces in tapping mode yielded a σ of 0.7 ± 0.2 nm and peak-to-valley (P-V) distance of 4 ± 1.2 nm for Si and a σ of 0.8 ± 0.3 nm and a P-V of 3.1 ± 0.8 nm for SiO₂. Prior to testing, the silicon samples were cleaned by immersing them in a ‘piranha etch’ solution (3:1 solution by volume of 98% sulphuric acid and 30% hydrogen peroxide) for 10 minutes to remove any organic contaminants.

Material	Upper width w_1 (nm)	Lower width w_2 (nm)	Thickness t (nm)	Length l (μm)
Silicon	200 – 600	385 – 785	255	6.0
SiO ₂	250 – 700	560 – 990	425	6.0

Table 5.1: Dimensions of nanobeams used in this study.

5.2.2 Nanometer-scale bending test using an AFM

Quasi-static bending tests of the fixed nanobeams were conducted using the Dimension 3000 AFM (see Appendix A for description of AFMs). A three-sided pyramidal diamond tip with a tip radius of 200 nm, mounted on a rectangular stainless steel cantilever was used for the bending tests (description of tips given in Appendix A).

The stiffness of cantilever beam used for the experiments reported here was 180 N/m. This value has a 10% error in it due to variations in thickness. The sensitivity, S , of the cantilever was calibrated prior to the bending tests as shown in Figure 5.4(a). The tip was pushed against a smooth diamond sample (root mean square roughness < 1.5 nm) by moving the z-piezo over a known distance and the vertical deflection signal (dV_{AFM} in Volts) of the tip from the photodiode is measured. Since diamond can be considered to be an infinitely hard material, the actual deflection of the tip is assumed to be the same as the z-piezo travel (D_{piezo}). Hence the photodetector sensitivity (S) for the cantilever setup is determined as

$$S = D_{piezo}/dV_{AFM} \text{ nm/V} \quad (5.1)$$

For the bending test of the nanobeams, the tip was brought over the nanobeam array with the help of the sample stage of the AFM and a built-in high magnification optical microscope (Fig. 5.4b). Fine positioning of the tip over a chosen beam was performed in contact mode at a contact load of about 2 to 4 μN , which resulted in negligible damage to the sample. To position the tip at the center of the beam span, the tip was located at one end of a chosen beam. The tip was moved to the other end of the beam by giving the x-piezo an offset voltage. The value of this offset was determined as an average from several such attempts in order to minimize effects of piezo drift. Half of this offset was then applied to the x-piezo after the tip was positioned at one end of the beam, which usually resulted in the tip being moved to the center of the span.

Once the tip was positioned over the center of the beam span, using a NanoscriptTM program (given in Appendix B), the tip was held stationary without scanning and the z-piezo was extended by a known distance, typically about 2.5 μm , at a rate of 10 nm/s, as shown in Fig. 5.4(b). During this time, the vertical deflection signal (dV_{AFM}), which is proportional to the deflection of the cantilever (D_{tip}), was monitored. The displacement of the piezo should be equal to the sum of the displacements of the cantilever and the nanobeam. Hence the displacement of the nanobeam (D_{beam}) under the point of load can be determined as

$$D_{beam} = D_{piezo} - D_{tip} = D_{piezo} - dV_{AFM} \times S \quad (5.2)$$

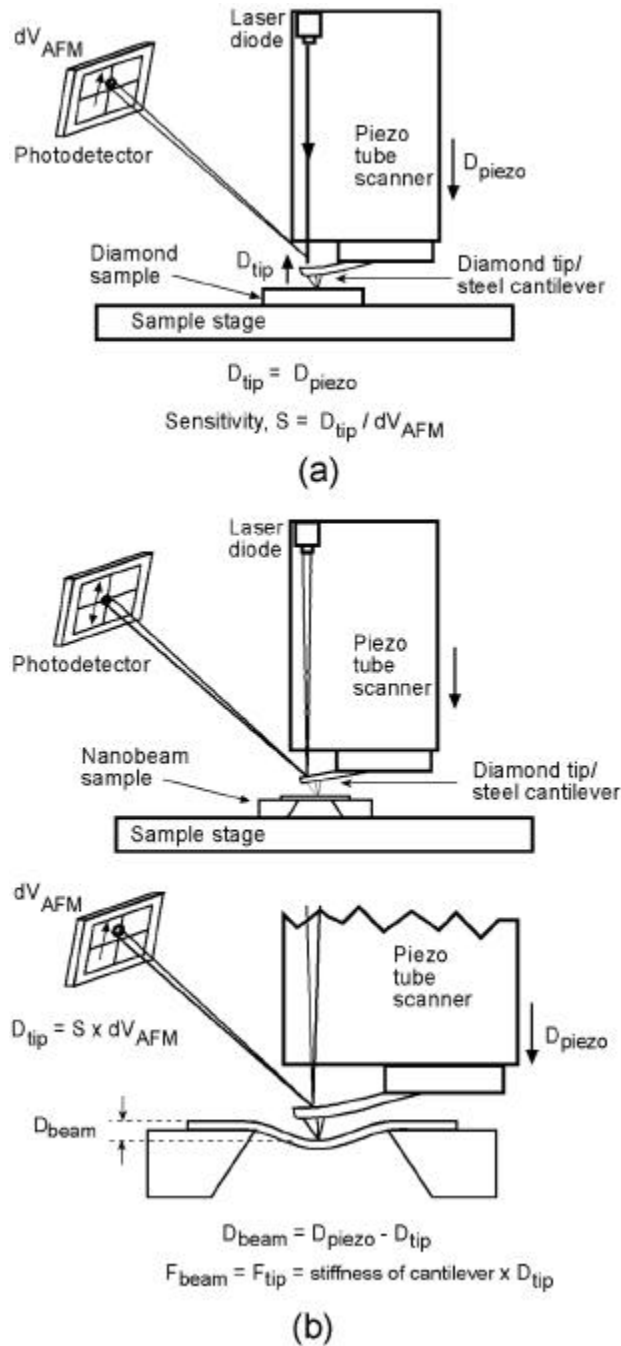


Figure 5.4: (a) Schematic of experiment to determine sensitivity of the photodetector for a diamond tip setup in the AFM. (b) The sensitivity is used in determining cantilever deflection in the nanoscale bending test technique. The AFM tip is brought to the center of the nanobeam and the piezo is extended over a known distance. By measuring the tip displacement, a load displacement curve of the nanobeam can be obtained.

The load (F_{beam}) on the nanobeam is the same as the load on the tip/cantilever (F_{tip}) and is given by

$$F_{beam} = F_{tip} = D_{tip} \times k \quad (5.3)$$

where k is the stiffness of the tip/cantilever (see Eq. A.2 in Appendix A). In this manner, a load displacement curve for each nanobeam was obtained. The diamond tip used was a worn one. Indentation experiments using this tip on a silicon substrate yielded a residual depth of less than 8 nm at a maximum load of 120 μ N, which is negligible compared to displacements of the beams (several hundred nanometers). Hence we can assume that negligible local indentation or damage is created during the bending process of the beams and that the displacement calculated from Eq. (5.2) is entirely that of the beam structure. The beam samples were fixed onto flat sample chucks using double-stick tape.

5.2.3 Determination of elastic modulus and bending strength

Elastic modulus and bending strength (fracture stress) of the beams can be estimated by equations based on the assumption that the beams follow linear elastic theory of an isotropic material. This is probably valid since the beams have high length-to-width and length-to-thickness ratios and also since the length direction is along the principal stress direction during the test. For a fixed elastic beam loaded at the center of the span, the elastic modulus is expressed as (Roark, 1965):

$$E = \frac{l^3}{192I} m \quad (5.4)$$

where l is the beam length, I is the area moment of inertia for the beam cross-section and m is the slope of the load-displacement curve during bending (Roark, 1965). The area moment of inertia is calculated from the following equation:

$$I = \frac{w_1^2 + 4w_1w_2 + w_2^2}{36(w_1 + w_2)} t^3, \quad (5.5)$$

where w_1 and w_2 are the upper and lower widths respectively and t is the thickness of the beam. According to linear elastic theory, for a centrally loaded beam, the moment

diagram is shown in Fig. 5.5. The maximum moments are generated at the ends (negative moment) and under the loading point (positive moment). The bending stresses generated in the beam are proportional to the moments and are compressive or tensile about the neutral axis (line of zero stress). The maximum tensile stress (σ_b , which is the fracture stress) is produced on the top surface at both the ends and is given by (Roark, 1965):

$$s_b = \frac{F_{max} l e_l}{8I}, \quad (5.6)$$

where F_{max} is the applied load at failure, l is the length of the beam and e_l is the distance of the top surface from the neutral plane of the beam cross-section and is given by:

$$e_l = \frac{t(w_1 + 2w_2)}{3(w_1 + w_2)} \quad (5.7)$$

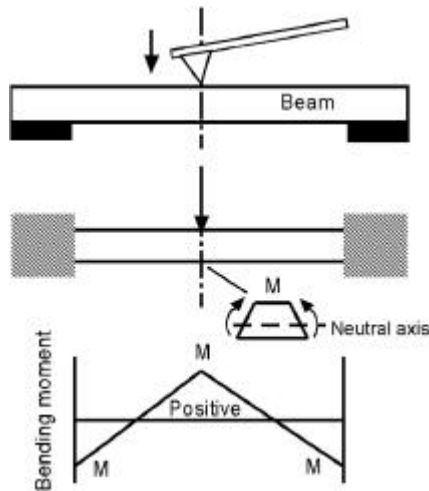


Figure 5.5: A schematic of the bending moments generated in the beam during a quasi - static bending experiment, with the load at the center of the span. The maximum moments occur under the load and at the fixed ends. Due to the trapezoidal cross section, the maximum tensile bending stresses occur at the top surfaces at the fixed ends.

Although the moment value at the center of the beam is the same as at the ends, the tensile stresses at the center (generated on the bottom surface) are less than those generated at the ends (per Eq. 5.6) because the distance from the neutral axis to the bottom surface is less than e_1 . This is because of the trapezoidal cross section of the beam, which results in the neutral axis being closer to the bottom surface than the top (Fig. 5.5).

5.2.4 Finite element model

In the preceding analysis, the beams were assumed to have ideal fixed ends. However, in reality, they are a little different. The underside of the beams is pinned over some distance on either side of the span as can be seen in Fig. 5.3. Hence a finite element model of the beams was created to see if the difference in the boundary conditions affected the stresses and displacements of the beams. The model was created using the commercial package ANSYS. The beam span was modeled using dimensions obtained from AFM measurements (Table 5.1) along with extensions of 1 μm on either side of the span. The element type used was 'SOLID 95', which is a 3-D, 8-node element defined by 20 nodes and having three degrees of freedom per node: translations in the nodal x, y, and z directions. The mesh was regular in most regions of the beam while a finer mesh was used near the constrained ends. The applied load was distributed over 15 nodes in the center of the beam span. The materials, namely Si and SiO_2 , were assumed to be linear elastic materials with the properties listed in Table 5.2. In order to verify the accuracy of the model, load displacement curves from a bending experiment was compared with the curve predicted by the model (for the same load). The comparison is given in Fig. 5.6(a). The curves are well correlated in indicating that the model can be used with confidence to predict stresses during bending. Results indicated that the maximum tensile bending stresses occurred near the ends as shown in Fig. 5.6(b). For a silicon beam with upper width 250 nm, a load of 75 μN resulted in a maximum tensile stress of 15.96 GPa according to Eq. (5.6) and a stress of 16.08 GPa from the model, the difference in the stresses being less than 1%. This indicates that the boundary

conditions near the ends of the actual beams are not that different from that of ideal fixed ends. All the bending strength values reported in this study were calculated from Eq. (5.7).

Material	Elastic (Young's) Modulus (GPa)	Poisson's ratio
Si	169 ¹	0.28 ²
SiO ₂	73 ³	0.17 ³

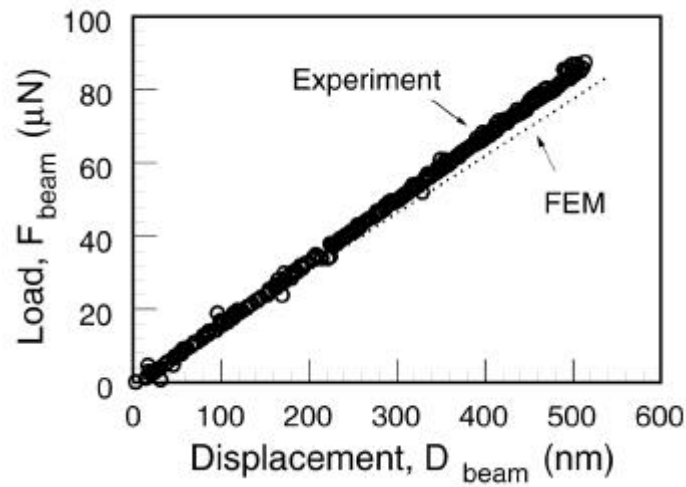
¹Si[110], Bhushan and Venkatesan, 1993; ²Anonymous, 1988; ³Bhushan and Gupta, 1991.

Table 5.2: Material properties used for finite element model

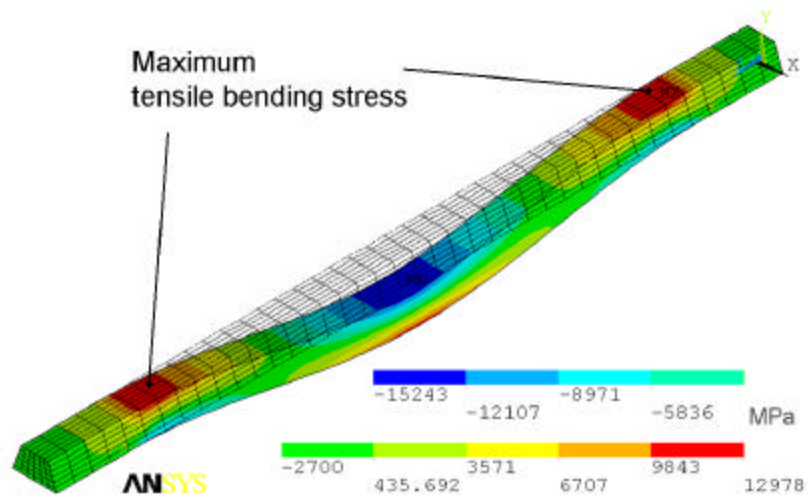
5.2.5 Method to estimate nanoscale fracture toughness

The nanobeam samples used in this study are not best suited for fracture toughness measurements because they do not possess regions of uniform stress during bending. Using these samples however, the following method is proposed to obtain an estimate of nanoscale fracture toughness. The steps in the method are outlined schematically in Fig. 5.7(a). First, a crack of known geometry is introduced in the region of maximum tensile bending stress, i.e. on the top surface near the ends of the beam. This is achieved by generating a scratch at high normal load across the width of the beam using a sharp diamond tip (radius < 100 nm). A typical scratch thus generated is shown in Fig. 5.7(b). By bending the beam as shown, a stress concentration will be formed under the scratch. This will lead to failure of the beam under the scratch once a critical load (fracture load) is attained. The fracture load and relevant dimensions of the scratch are input into the FEM model, which is used to generate the fracture stress. Figure 5.7(c) shows an FEM simulation of one such experiment, which reveals that the maximum stress does occur under the scratch.

If we assume that the scratch tip acts as a crack tip, a bending stress will tend to open the crack in Mode I. In this case, the stress field around the crack tip can be



(a)



(b)

Figure 5.6: (a) A comparison of load displacement curves of a nanobeam obtained from an AFM experiment and using the finite element model. The curves show good correlation indicating that the model can be confidently used to estimate stresses in the beams. (b) Bending stress distribution indicating that the maximum tensile stresses occur on the top surfaces near the fixed ends.

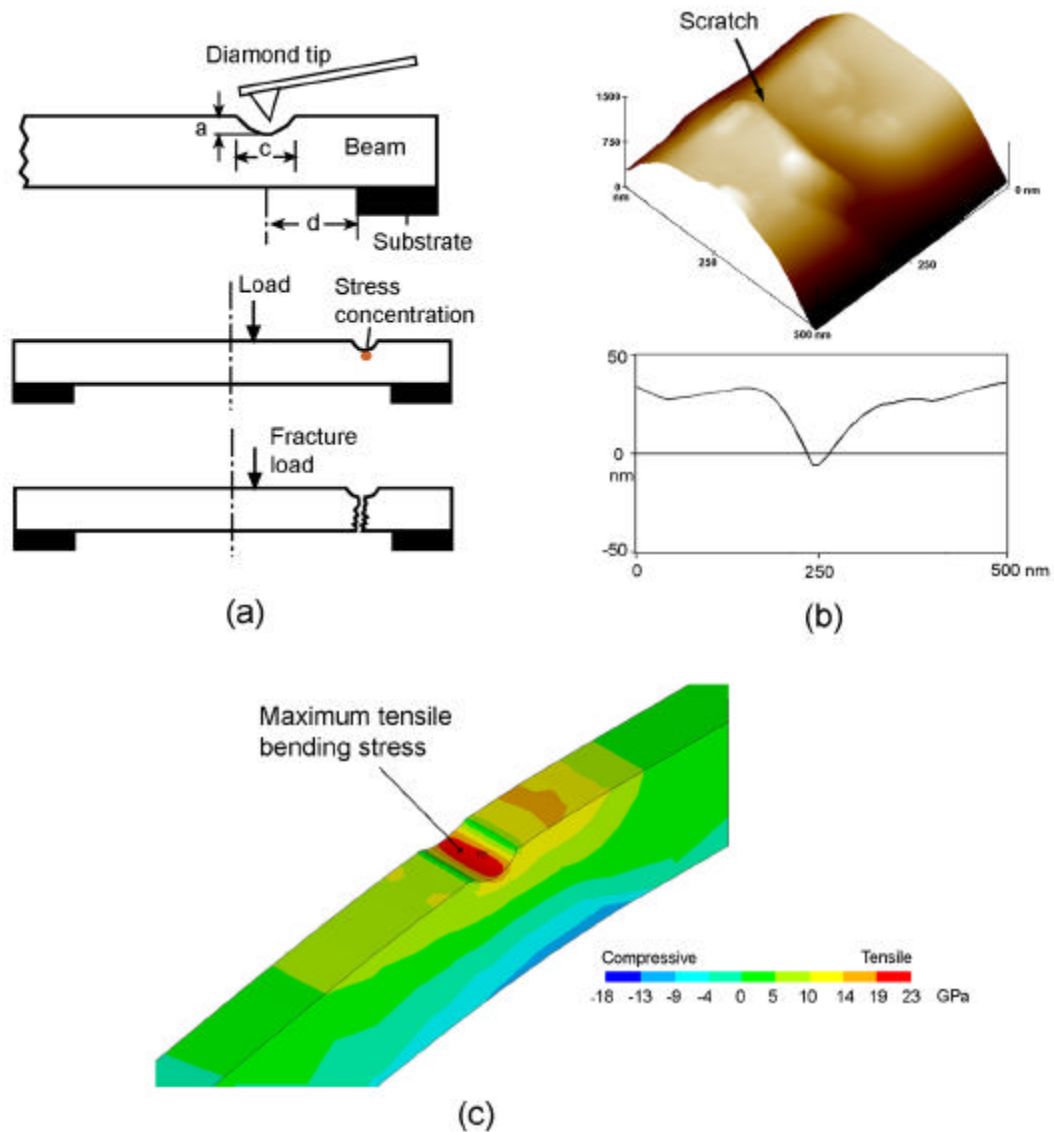


Figure 5.7: (a) Schematic of technique to generate a defect (crack) of known dimensions in order to estimate fracture toughness. A diamond tip is used to generate a scratch across the width of the beam. When the beam is loaded as shown, a stress concentration is formed at the bottom of the scratch. The fracture load is then used to evaluate the stresses using FEM. (b) AFM 3-D image and 2-D profile of a typical scratch. (c) Finite element model results verifying that the maximum bending stress occurs at the bottom of the scratch.

described by the stress intensity parameter K_I (for Mode I) for linear elastic materials (Hertzberg, 1989). In particular the stresses corresponding to the bending stresses are described by

$$\mathbf{s} = \frac{K_I}{\sqrt{2pr}} \cos\left(\frac{\mathbf{q}}{2}\right) \left[1 + \sin\left(\frac{\mathbf{q}}{2}\right) \sin\left(\frac{3\mathbf{q}}{2}\right) \right] \quad (5.8)$$

for every point $p(r, \mathbf{q})$ around the crack tip as shown in Fig. 5.8. If we substitute the fracture stress into the left hand side of Eq. (5.8), then the K_I value can be substituted by its critical value, which is the fracture toughness K_{IC} . Now, the fracture stress can be determined for the point ($r = 0$, $\mathbf{q} = 0$), i.e. right under the crack tip as explained above. However, we cannot substitute $r = 0$ in Eq. (5.8). The alternative is to substitute a value for r , which is as close to zero as possible. For silicon, a reasonable number is the distance between neighboring atoms in the (111) plane, the plane along which silicon exhibits the lowest fracture energy. This value was calculated from silicon unit cell dimensions of 0.5431 nm (Anonymous, 1988) to be 0.4 nm (half of the face diagonal). This assumes that Si displays no plastic zone around the crack tip, which is reasonable since in tension, silicon is not known to display plastic deformation at room temperature. We decided to use values $r = 0.4$ to 1.6 nm (i.e. distances up to 4 times the distance between the nearest neighboring atoms) to estimate the fracture toughness for both Si and SiO_2 according to the following equation

$$K_{IC} = \mathbf{s}_f \sqrt{2pr} \quad r = 0.4 \text{ to } 1.6 \text{ nm} \quad (5.9)$$

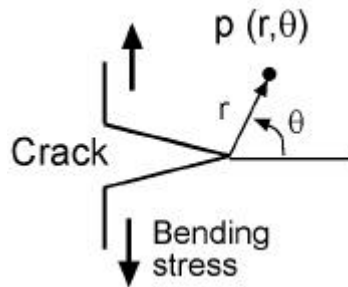


Figure 5.8: Schematic of crack tip and coordinate systems used in Eq. 5.9 to describe a stress field around the crack tip in terms of the stress intensity parameter, K_I .

5.2.6 Fatigue experiments of nanobeams

A technique to study the fatigue properties of the nanobeams via application of monotonic cyclic stresses using an AFM is described here. Figure 5.9(a) shows a schematic of the test method. Similar to the bending test, the diamond tip is first positioned at the center of the beam span. In order to ensure that the tip is always in contact with the beam (as opposed to impacting it), the piezo is first extended by a distance D_1 , which ensures a minimum stress on the beam. After this extension, a cyclic displacement of amplitude D_2 is applied continuously till failure of the beam occurs. This results in application of a cyclic load to the beam. These controlled movements of the piezo are achieved using a Nanoscript™ program (given in Appendix B). The maximum frequency of the cyclic load that could be attained using the AFM was 4.2 Hz. The vertical deflection signal of the tip is monitored throughout the experiment. The signal follows the pattern of the piezo input up to failure, which is indicated by a sudden drop in the signal. During initial runs, piezo drift was observed that caused the piezo to move gradually away from the beam (i.e. to retract), resulting in a continuous decrease in the applied normal load. In order to compensate for this, the piezo is given a finite extension of 75 nm every 300 seconds as shown in Fig. 5.9(a). This resulted in keeping the applied loads fairly constant. The normal load variation (calculated from the vertical deflection signal) from a fatigue test is shown in Fig. 5.9(b). The cyclic stress amplitudes (corresponding to D_2) and fatigue lives were recorded for every sample tested. Values for D_1 were set such that minimum stress levels were about 20% of the bending strengths.

5.3 Results and Discussion

5.3.1 Elastic modulus and bending strength

Figure 5.10 shows typical load displacement curves for Si and SiO₂ beams that were bent to failure. The upper width of the beams is indicated in the figure. Also indicated in the figure are the elastic modulus values obtained from the slope of the load displacement curve (Eq. 5.4). About 12 beams each of Si and SiO₂ were tested. All the

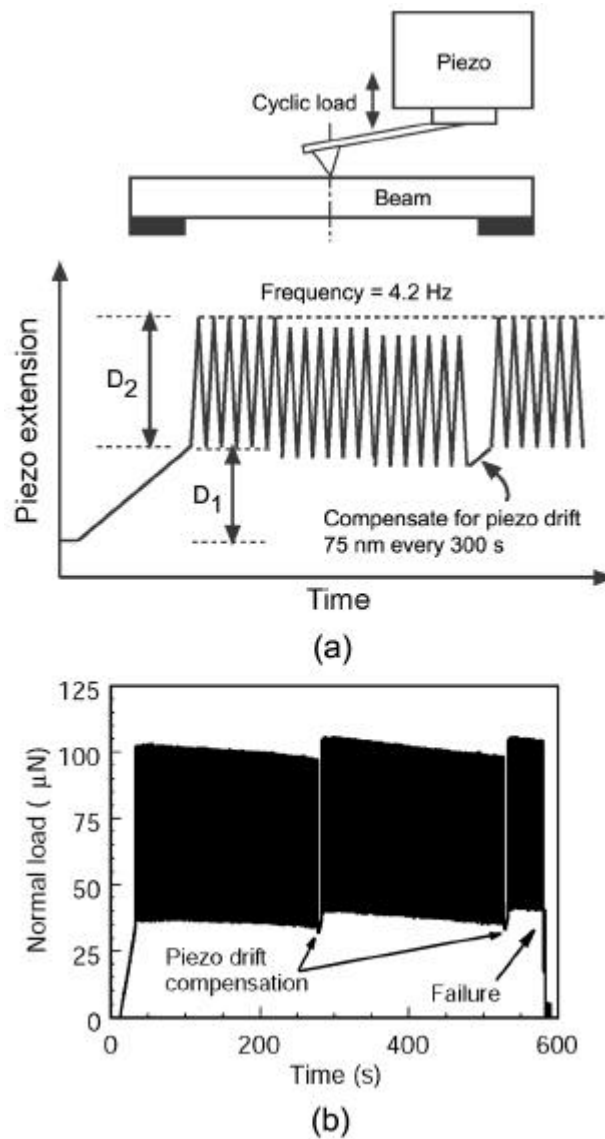


Figure 5.9: (a) Schematic showing the details of the technique to study fatigue behavior of the nanobeams. The diamond tip is located at the middle of the span and a cyclic load at 4.2 Hz is applied to the beam by forcing the piezo to move in the pattern shown. An extension is made every 300 s to compensate for the piezo drift to ensure that the load on the beam is kept fairly constant. (b) Data from a fatigue experiment on a nanobeam until failure. The normal load is computed from the raw vertical deflection signal. The compensations for piezo drift keep the load fairly constant.

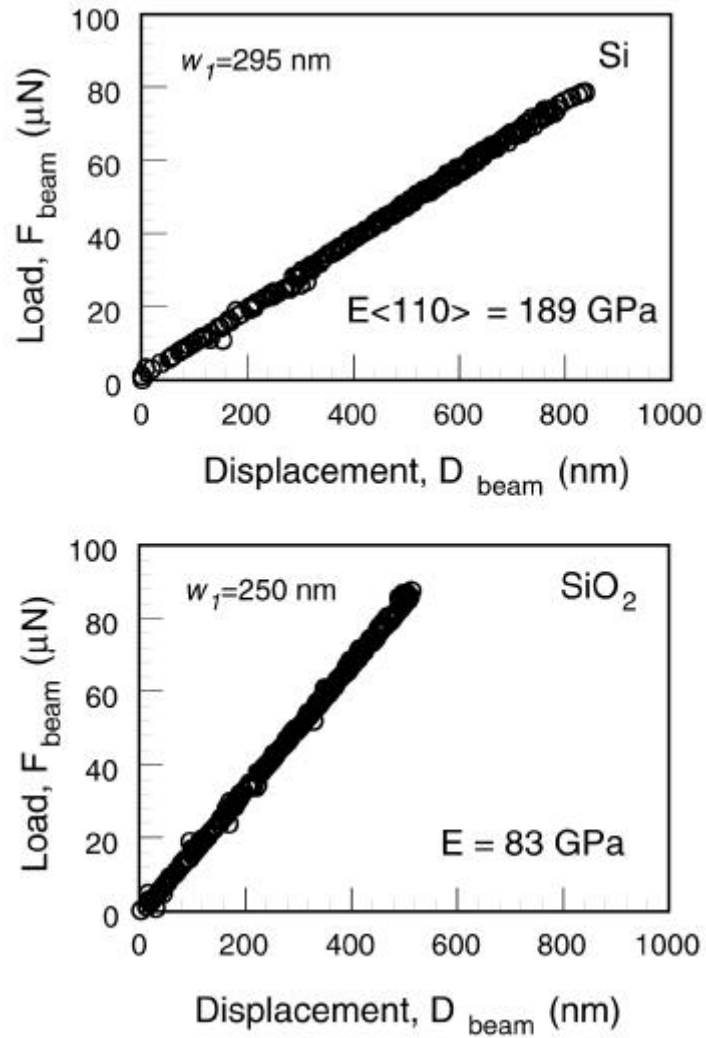


Figure 5.10: Typical load displacement curves of silicon and SiO_2 nanobeams. The curves are linear until sudden failure, indicative of brittle fracture of the beams. The elastic modulus (E) values calculated from the curves are shown.

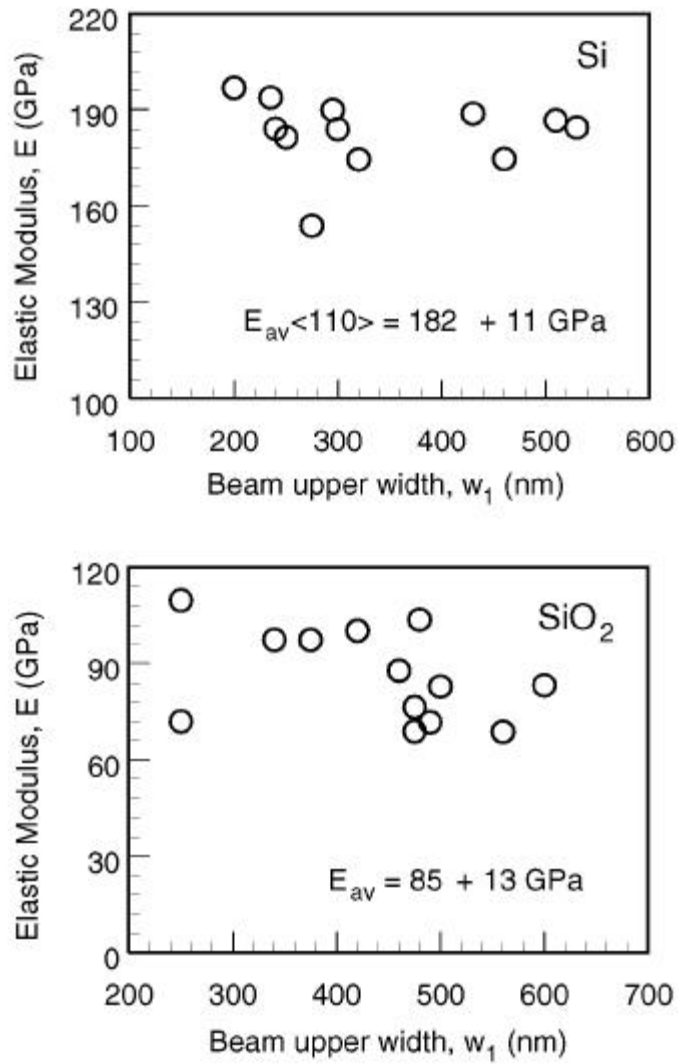


Figure 5.11: Elastic modulus values measured for Si and SiO₂. The average values are shown. These are comparable to bulk values, which shows that elastic modulus shows no specimen size dependence.

beams showed linear elastic behavior followed by abrupt failure, which is suggestive of brittle fracture. Figure 5.11 shows the scatter in the values of elastic modulus obtained for both Si and SiO₂ along with the average values (\pm standard deviation). The scatter in the values may be due to differences in orientation of the beams with respect to the trench and the loading point being a little off-center with respect to the beam span. The average values are a little higher than the bulk values (169 GPa for Si[110] and 73 GPa for SiO₂ in Table 5.2). However the values of E obtained from Eq. (5.4) have an error of about 20% due to the uncertainties in beam dimensions and spring constant of the tip/cantilever (which affects the measured load). Hence the elastic modulus values on the nanoscale can be considered to be comparable to bulk values. This is in agreement with E values obtained from microscale specimens as well (Sharpe et al., 1997; Sato et al., 1998; Namazu et al., 2000).

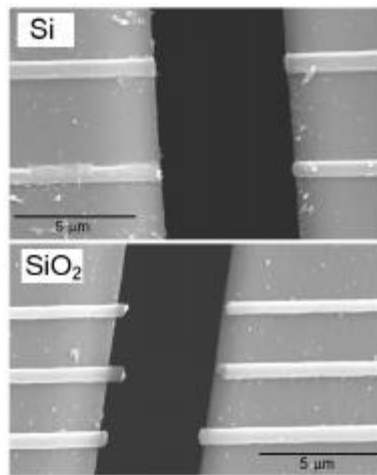


Figure 5.12: SEM micrographs of nanobeams that failed during quasi-static bending experiments. The beams failed at or near the ends, which is the location of maximum tensile bending stress.

Most of the beams when loaded quasi-statically at the center of the span broke at the ends as shown in Fig. 5.12, which is consistent with the fact that maximum tensile stresses occur on the top surfaces near the ends. Figure 5.13 shows the values of bending

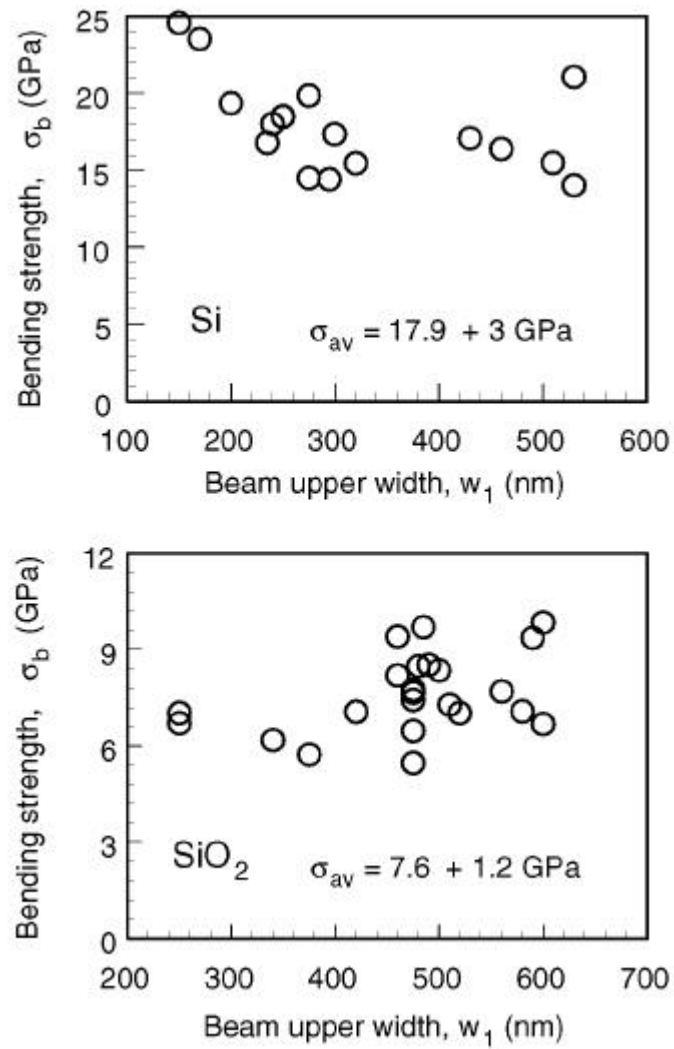


Figure 5.13: Bending strength values obtained from bending experiments. Average values are indicated. These values are much higher than values reported for microscale specimens, indicating that bending strength shows a specimen size effect.

strength obtained for different beams. There appears to be no trend in bending strength with the upper width of the beams. The large scatter is expected for strengths of brittle materials, since they are dependent on pre-existing flaw population in the material and hence are statistical in nature. Statistical analysis can be used to describe the scatter in the bending strength values. The Weibull distribution function is a simple empirical expression that can represent such stochastic data. The Weibull distribution is (Weibull, 1951; Dodson, 1994):

$$F(x) = 1 - e^{-\left(\frac{x - x_u}{x_0}\right)^m} \quad (5.10)$$

In our application, x represents the measured strength. The constant x_u locates the origin of the distribution, which in this case is the applied stress below which there is a zero probability of failure. Therefore it is reasonable to assume $x_u = 0$. The constant x_0 is a scaling factor that stretches the distribution. When $x = x_0$, $F(x) = 0.632$, which represents the applied stress at which 63.2% of the population would be expected to fail. The Weibull modulus, m , controls the shape of the distribution and represents the degree of scatter in the population. A larger value of m represents less scatter. When $m = 3.44$, the Weibull distribution closely approximates a normal distribution.

In order to determine the Weibull modulus, the bending strength values in Fig. 5.13 are placed in ascending order and a mean rank, or survival probability, is assigned by

$$P_n = \frac{n}{N + 1} \quad (5.11)$$

where N is the size of the population (number of samples). A plot of $\ln(\ln[(1 - P_n)^{-1}])$ is plotted against $\ln(\sigma_b)$ and is shown in Fig. 5.14(a). The slope of a straight line fitted to this data gives the Weibull modulus. The y -intercept (y_0) is used to determine the scaling factor, x_0 :

$$x_0 = \exp\left(\frac{-y_0}{m}\right) \quad (5.12)$$

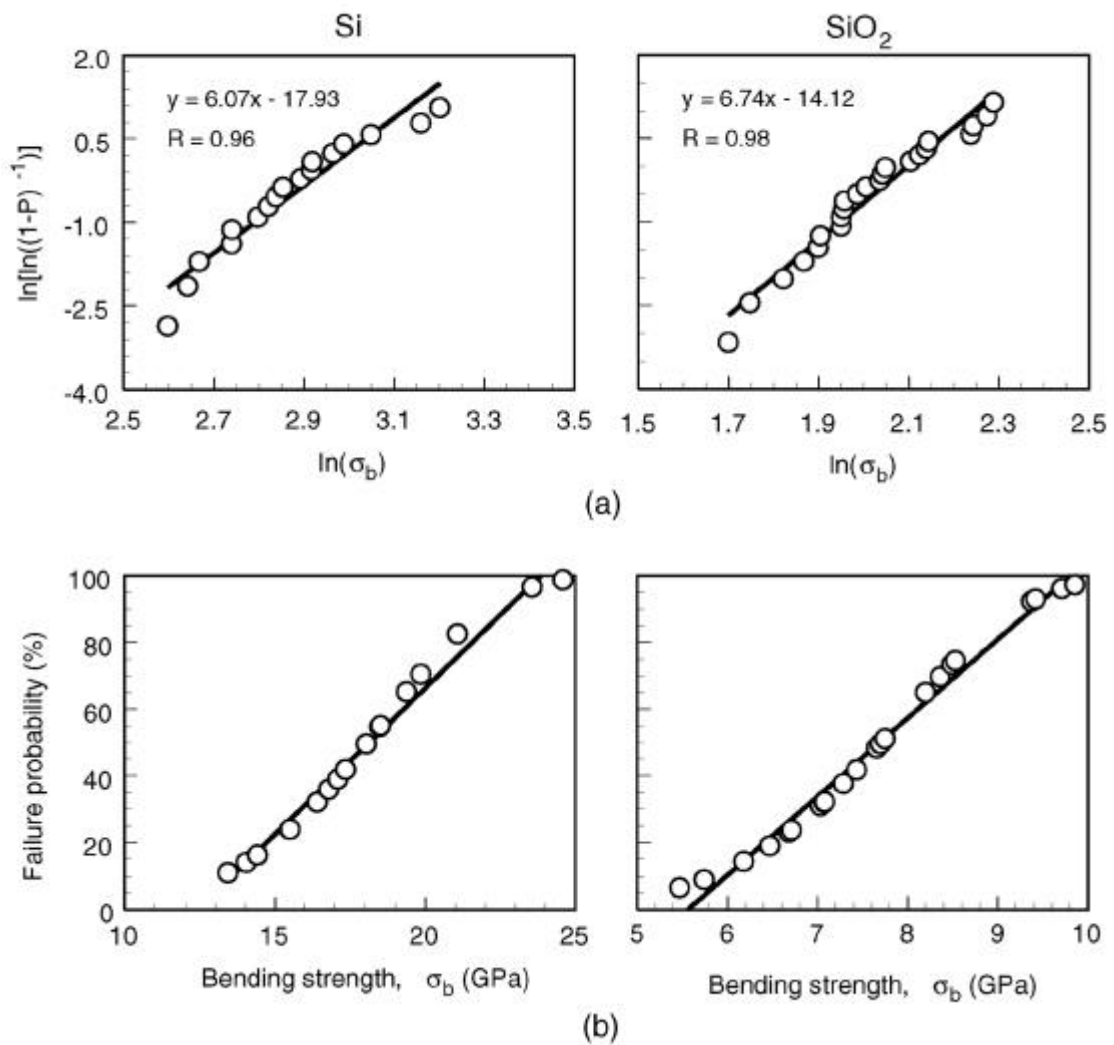


Figure 5.14: Weibull analysis of bending strength data. (a) Both Si and SiO_2 data fit a 2-parameter Weibull distribution as shown. The slopes of the fitted lines give the Weibull moduli. (b) Failure probability plotted as a function of bending strength (fracture stress).

This graphical method is one of several accepted methods for determining the Weibull parameters. The goodness of fit of the data is revealed by the regression coefficients (0.96 for Si and 0.98 for SiO₂). The Weibull distributions for the bending strengths are given as:

$$F(x) = 1 - e^{-\left(\frac{x}{19.20}\right)^{6.07}} \quad \text{for Si}$$

$$F(x) = 1 - e^{-\left(\frac{x}{8.13}\right)^{6.74}} \quad \text{for SiO}_2 \quad (5.13)$$

Figure 5.14(b) shows the same data as in Fig. 5.14(a) presented in terms of probability of failure for a given applied bending stress. The means of the distributions were found to be 17.9 GPa and 7.6 GPa for Si and SiO₂ respectively. Previously reported numbers of strengths range from 1 - 6 GPa for silicon and about 1 GPa for SiO₂ microscale specimens. This clearly indicates that bending strength shows a specimen size dependence. Strength of brittle materials is dependent on pre-existing flaws in the material. Since for nanoscale specimens, the volume is smaller than for micro and macroscale specimens, the flaw population will be smaller as well, resulting in higher values of strength.

5.3.2 Fracture toughness

Table 5.3 shows the beam dimensions, relevant scratch dimensions and the fracture stresses obtained for both Si and SiO₂ beams. The beams in Table 5.3 represent about 60% of total beams tested for fracture toughness, as the other beams did not break at the location of the scratch. This fact was verified by AFM imaging of the beams before and after the bending test. Estimates of fracture toughness calculated using Equation (5.9) for Si and SiO₂ are shown in Figure 5.15. The results show that the K_{IC} estimate for Si is about 1 - 2 MPa√m whereas for SiO₂ the estimate is about 0.5 - 0.9 MPa√m. These values are comparable to values reported by others on larger specimens for silicon and SiO₂. The high values obtained for Si could be due to the fact that the

Sample	Upper width w_1 (nm)	Distance of scratch from fixed end, d (nm)	Scratch dims. Width/depth, c/a (nm)	Fracture Load (μN)	Fracture stress evaluated by FEM, σ_{fracture} (GPa)
Silicon	275	350	170/35	65	19.9
Silicon	462	15	150/35	45	18.5
Silicon	250	35	150/30	42	24.6
Silicon	437	290	140/30	54	23.6
Silicon	150	120	180/40	110	21.0
SiO ₂	475	270	180/35	124	7.7
SiO ₂	784	50	180/20	138	7.0
SiO ₂	520	250	160/30	129	7.3
SiO ₂	829	80	180/30	120	7.8
SiO ₂	510	100	180/30	115	7.4
SiO ₂	819	100	190/50	152	9.9

Table 5.3: Fracture stresses for experiments to estimate K_{IC}

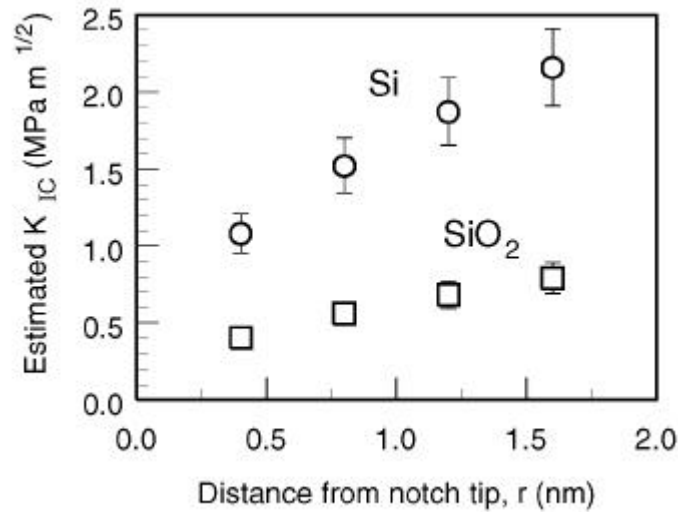


Figure 5.15: Values of fracture toughness (K_{IC}) calculated from Eq. 5.9 for increasing values of r corresponding to distance between neighboring atoms in $\{111\}$ planes of silicon (0.4 nm). Hence r -values between 0.4 and 1.6 nm are chosen. The K_{IC} values thus estimated are comparable to values reported by others for both Si and SiO₂.

scratches, despite being quite sharp, still have a finite radius of about 100 nm. This means that the toughness values obtained may be notch toughness rather than fracture toughness. However, researchers have measured actual cracks in silicon microscale specimens using an AFM (Komai et al., 1998) and have reported crack dimensions (width to depth ratio of 10:1) that are comparable to the scratch dimensions in this study, hence giving some confidence to the claim here that it is indeed fracture toughness that we are evaluating. The bulk value for silicon is about $0.9 \text{ MPa}\sqrt{\text{m}}$. Fracture toughness is considered to be a material property and is believed to be independent of specimen size. The values obtained in this study, given its limitations, appear to show that fracture toughness is comparable, if not a little higher on the nanoscale.

Table 5.4 summarizes the various properties measured via quasi-static bending in this study. Also shown are bulk values of the parameters along with values reported on larger scale specimens by other researchers. Elastic modulus and fracture toughness values appear to be comparable to bulk values and show no dependence on specimen size. However bending strength shows a clear specimen size dependence with nanoscale numbers being twice as large as numbers reported for larger scale specimens.

Sample	Elastic modulus E (GPa)		Bending strength σ_b (GPa)		Fracture toughness K_{IC} ($\text{MPa}\sqrt{\text{m}}$)		
	Measured	Bulk value	Measured	Reported, microscale	Estimated	Reported, microscale	Bulk value
Si	182 ± 11	169	18 ± 3	$< 10^1$	1.67 ± 0.4	$0.6 - 1.65^3$	0.9^4
SiO ₂	85 ± 13	73	7.6 ± 2	$< 2^2$	0.60 ± 0.2	$0.5 - 0.9^2$	-
Number of samples:		E: Si - 11, SiO ₂ - 12		σ_b : Si - 17, SiO ₂ - 23		K_{IC} : Si - 5, SiO ₂ - 6	

¹Ericson and Schweitz, 1990; Wilson and Beck, 1996; Sharpe et al., 1997; Tsuchiya et al., 1998; Greek et al., 1999; Yi et al., 2000. ²Tsuchiya et al., 2000. ³Johansson et al., 1989; Ballarini et al., 1997; Fitzgerald et al., 2000. ⁴Anonymous, 1988.

Table 5.4: Summary of measured parameters from quasi-static bending tests.

5.3.3 Fatigue

Table 5.5 shows the stress levels applied to the various beams used in the fatigue study along with the measured fatigue lives. The minimum stress was 3.5 GPa for Si beams and 2.2 GPa for SiO₂ beams. The frequency of applied load was 4.2 Hz. In general, the fatigue life decreased with increasing mean stress as well as increasing stress amplitude. When the stress amplitude was less than 15% of the bending strength, the fatigue life was greater than 30,000 cycles for both Si and SiO₂. However, the mean stress had to be less than 30% of the bending strength for a life of greater than 30,000 for Si whereas even at a mean stress of 43% of the bending strength, SiO₂ beams showed a life greater than 30,000. Figure 5.16 shows that during fatigue, the beams broke under the loading point or at the ends, when loaded at the center of the span. This was different from the quasi-static bending tests, where the beams broke at the ends almost every time. This could be due to the fact that the stress levels under the load and at the ends are not that different and fatigue crack propagation could occur at either location. Figure 5.17 shows a nanoscale S-N curve, with bending stress (S) as a function of fatigue

Sample	Mean Stress (GPa)	Stress Amplitude (GPa)	Fatigue life (x 1000 cycles)
Silicon	8.0	4.6	2.03
	7.5	4.0	8.72
	6.9	3.4	12.60
	6.5	3.0	5.96
	4.9	1.4	> 30
SiO ₂	4.8	2.6	0.1
	4.3	2.1	5.2
	4.1	1.9	5.6
	4.1	1.8	12.8
	4.0	1.8	2.4
	3.9	1.7	2.5
	3.7	1.6	13.4
	3.3	1.2	> 30
	3.2	1.0	> 30

Bending strength, σ_b : Si – 18 ± 3 GPa; SiO₂ – 7.6 ± 2 GPa.

Table 5.5: Summary of fatigue test data.

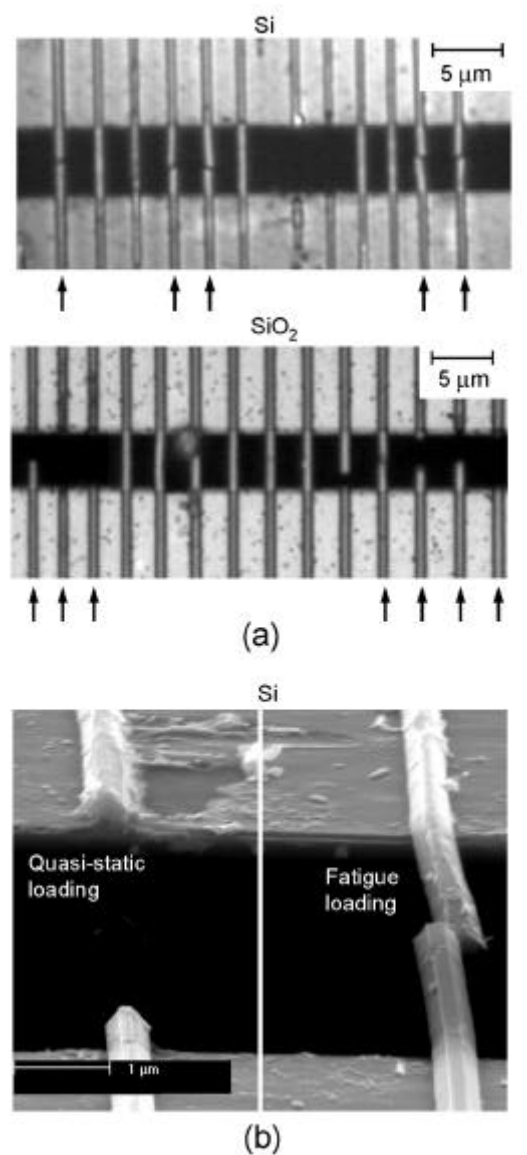


Figure 5.16: (a) Optical micrographs with arrows indicating beams failed under cyclic (fatigue) loading. During fatigue, failure of the beam occurs under the point of loading (near the center of the span) or at the beam-ends. (b) SEM micrograph showing a close up of failure locations under quasi -static bending and fatigue.

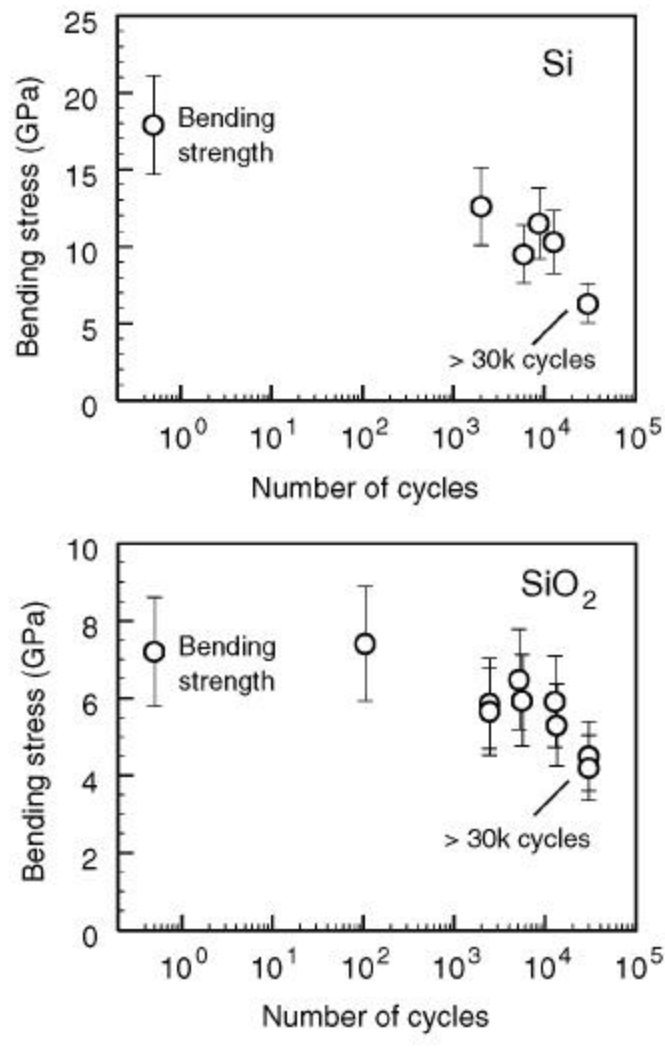


Figure 5.17: Fatigue test data showing applied bending stress as a function of number of cycles; nanoscale SN curves.

in cycles (N) with an apparent endurance life at lower stress. This study clearly demonstrates that fatigue properties of nanoscale specimens can be studied. The loading position during fatigue is prone to shifting due to piezo drift, which results in an uncertainty of about 25% in the applied load and hence the stress (indicated by the error bars in Fig. 5.17).

5.3.4 SEM observations of fracture surfaces

Figure 5.18 shows SEM images of the fracture surfaces of beams broken during quasi-static bending as well as fatigue. In the quasi-static cases, the maximum tensile stresses occur on the top surface, so it is reasonable to assume that fracture initiated at or near the top surface and propagated downward. The fracture surfaces of the beams suggest a cleavage type of fracture. Silicon beam surfaces show various ledges or facets, which is typical for crystalline brittle materials. Silicon usually fractures along the (111) plane due to this plane having the lowest surface energy to overcome by a propagating crack. However, failure has also been known to occur along the (110) planes, despite the higher energy required as compared to the (111) planes (Wilson and Beck, 1996). The plane normal to the beam direction in these samples is the (110) plane while (111) planes will be oriented at 35° from the (110) plane. The presence of facets and irregularities on the silicon surface in Fig. 5.18(a) suggest that it is a combination of these two types of fractures that has occurred. Since the stress levels are very high for these specimens, it is reasonable to assume that crack propagating forces will be high enough to result in (110) type failures. In contrast, the silicon fracture surfaces under fatigue, shown in Fig. 5.18(b), appear very smooth without facets or irregularities. This is suggestive of low energy fracture, i.e. of (111) type fracture. We do not see evidence of fatigue crack propagation in the form of steps or striations on the fracture surface. Such features have never been reported for silicon at room temperature and may be expected only at higher temperatures. We believe that for the stress levels applied in these fatigue experiments, failure in silicon occurred via cleavage associated with ‘static fatigue’ type of failures.

SiO_2 shows very smooth fracture surfaces for both quasi-static bending and fatigue. This is in contrast to the hackled surface one might expect for the brittle failure

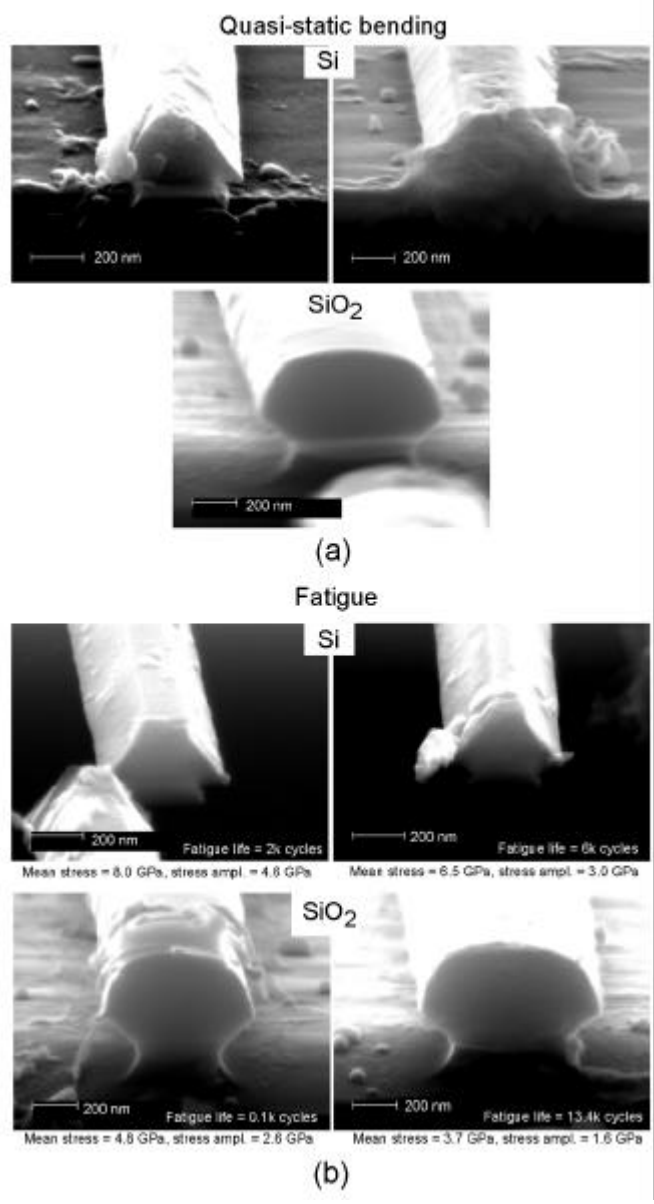


Figure 5.18: Fracture surfaces of silicon and SiO₂ beams subjected to (a) quasi-static bending and (b) fatigue.

of an amorphous material. However, in larger scale fracture surfaces for such materials, the region near the crack initiation usually appears smooth or mirror -like (Hertzberg, 1989). Since the fracture surface here is so small and very near the crack initiation site, it is not unreasonable to see such a smooth surface for SiO₂ on this scale. There appears to be no difference between the fracture surfaces obtained by quasi-static bending and fatigue for SiO₂.

5.4 Summary

A technique to perform bending tests of nanometer scale fixed beam specimens made of single-crystal silicon and SiO₂ using an AFM was developed. The bending tests were utilized to evaluate elastic modulus and bending strength (fracture stress). Techniques to estimate nanoscale fracture toughness (K_{IC}) of the beam materials and to study nanoscale fatigue response of the beams were also developed. This study is one of the first in the literature to study such mechanical properties of *nanoscale* structures.

- The beams exhibited elastic linear response with sudden brittle fracture.
- Elastic modulus values of 182 ± 11 GPa for Si<110> and 85 ± 3 GPa for SiO₂ were obtained, which are comparable to bulk values.
- Bending strength values of 18 ± 3 GPa for Si and 7.6 ± 2 GPa for SiO₂ were obtained, which are twice as large as values reported on larger scale specimens.
- Fracture toughness value estimates obtained were 1.67 ± 0.4 MPa \sqrt{m} for Si and 0.60 ± 0.2 MPa \sqrt{m} for SiO₂, which are also comparable to values obtained on larger specimens.
- At stress amplitudes less than 15% of their bending strength and at mean stresses of less than 30% of the bending strength, Si and SiO₂ displayed an apparent endurance life of greater than 30,000 cycles.
- SEM observations of the fracture surfaces revealed a cleavage type of fracture for both materials when subjected to bending as well as fatigue.

CHAPTER 6

CONCLUSIONS

In this research, techniques to study nanoscale tribological of MEMS components and coatings as well as to evaluate mechanical properties of nanoscale structures were developed and utilized to understand mechanisms behind observed phenomena. Below are the significant results of the various studies performed.

6.1 Topography-induced contributions to friction forces measured using an AFM

The following characteristics of the topography-induced contributions to measured friction forces in an AFM will be useful when attempting to differentiate these effects from material in samples with numerous topographical features (e.g. high roughness). In addition, they aid in understanding the forces experienced by an asperity (AFM tip) when moving over other asperities and similar surface features.

The changes in the friction force due to topography-induced effects will be of the same sign in both Trace and Retrace friction profiles (peaks in Trace correspond to peaks in Retrace) of the friction loop whereas changes due to material effects are in opposite directions. Topography-induced friction transitions always correspond to transitions in surface slope. The magnitude of the increase in friction force experienced by a tip when traversing up an asperity, step or similar topography feature is greater than the magnitude of the decrease in friction force experienced by the tip when traversing down the same feature. This is attributed to the ratchet mechanism of friction and to the 'collision' force encountered by the tip during the upward movement, which is absent during the downward movement. As a result, subtraction of Trace and Retrace friction profiles will

not eliminate topography-induced friction forces. This subtraction operation will, however, remove the effect of detector cross talk on the measured friction forces.

6.2 Static friction in micromotors

A novel technique to measure the static friction force of surface micromachined polysilicon micromotors using an AFM was developed. This technique was used to study the friction characteristics of unlubricated and lubricated motors. Static friction forces normalized to the rotor weight for a polysilicon-polysilicon contact were found to be in the range of 4 - 10 for unlubricated micromotors.

Perfluoropolyether (PFPE) lubricants were used to lubricate the motors. It was found that a bonded layer of Z-DOL lubricant appeared to provide good lubrication to the micromotors by reducing the normalized static friction force to below 4. A thin mobile layer of lubricant resulted in static friction forces up to three times higher than the values obtained for unlubricated ones.

A variation in the static friction forces with humidity was observed for the unlubricated motors. Meniscus effects at the rotor-hub interface are believed to be the cause of this variation. Bonded Z-DOL suppressed the effect of humidity on observed friction forces due to its hydrophobic nature. Solid-like hydrophobic lubricants appear to be ideal for lubrication of MEMS.

The undersides of the rotors exhibited drastically different topography from the topsides, possibly due to contact with etchants. Surface roughness measurements showed that the undersides exhibit negative skewness, which favors large real areas of contact and consequently high friction forces. This suggests that in order to reduce the problem of stiction, MEMS designers should try to ensure that the contacting surfaces exhibit surface roughness characteristics favoring low real area of contact, including positive skewness and high kurtosis.

6.3 Scratch/wear resistance of ultra-thin DLC coatings

AFM-based techniques were utilized to investigate scratch/wear resistance of DLC coatings less than 20 nm thick deposited by various deposition methods, including a continuous microscratch technique, which was developed as part of this study.

The continuous microscratch technique developed using the AFM yielded useful information on critical loads and initial failure mechanisms of the coatings. For both bare silicon and the coatings, the onset of ploughing, associated with plastic deformation, was the failure mechanism at the critical load. Critical loads were found to be directly proportional to the hardness and fracture toughness of the coatings. For coatings less than 5 nm thick, the deformation zones extended into the substrate and a good match of elastic properties between the coating and substrate resulted in higher load carrying capacity. Some non-uniform failure of the coatings were observed suggesting non-uniformity in coating properties.

Based on these studies, it was concluded that the coatings deposited using Electron Cyclotron Resonance Chemical Vapor Deposition (ECR-CVD) generally showed the best scratch/wear performance due to its high hardness, fracture toughness and good matching of elastic modulus with the silicon substrate as compared to the other coatings. Sputtered (SP) coatings generally showed the poorest scratch/wear resistance because of their low hardness. A thickness of 5 nm appears adequate for scratch/wear resistance (especially ECR-CVD) while 3.5 nm is too thin to be used as protective overcoats.

6.4 Mechanical properties of nanoscale structures

A technique to perform bending tests of nanometer scale fixed beam specimens made of single-crystal silicon and SiO₂ using an AFM was developed. The bending tests were utilized to evaluate elastic modulus and bending strength (fracture stress). Techniques to estimate nanoscale fracture toughness (K_{IC}) of the beam materials and to study nanoscale fatigue response of the beams were also developed.

The beams exhibited elastic linear response with sudden brittle fracture. Elastic modulus values of 182 ± 11 GPa for Si<110> and 85 ± 3 GPa for SiO₂ were obtained, which are comparable to bulk values. Bending strength values of 18 ± 3 GPa for Si and 7.6 ± 2 GPa for SiO₂ were obtained, which are twice as large as values reported on larger scale specimens. Fracture toughness value estimates obtained were 1.67 ± 0.4 MPa√m for Si and 0.60 ± 0.2 MPa√m for SiO₂, which are also comparable to values obtained on larger specimens. At stress amplitudes less than 15% of their bending strength and at mean stresses of less than 30% of the bending strength, Si and SiO₂ displayed an apparent endurance life of greater than 30,000 cycles. SEM observations of the fracture surfaces revealed a cleavage type of fracture for both materials when subjected to bending as well as fatigue.

APPENDIX A

DESCRIPTION OF ATOMIC FORCE/FRICTION FORCE MICROSCOPE (AFM/FFM), TIPS AND TECHNIQUES

A.1 Description of AFMs

The various studies reported were performed using either the small sample MultiMode AFM or the large sample Dimension 3000 AFM (Fig. A.1). Both are commercial AFMs made by Digital Instruments/Veeco (Santa Barbara, CA) utilizing the Nanoscope III and IIIa controllers respectively.

A schematic of the operation of the AFMs is given in Fig. A.2. A small -sample AFM/FFM operates on the following principle. The sample is mounted on a PZT tube scanner, which is scanned in the x -y plane and moved in the vertical (z) direction. A sharp tip at the free end of a flexible cantilever is brought into contact with the sample .

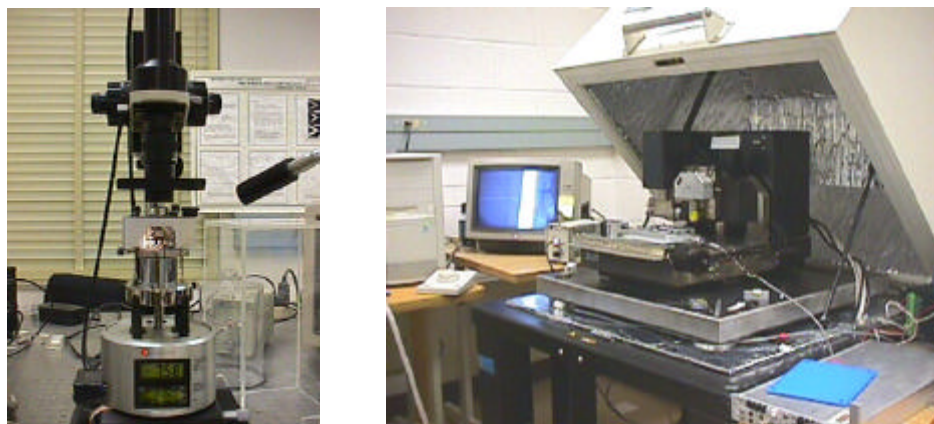


Figure A.1: The small sample MultiMode AFM (left) and the large sample Dimension 3000 AFM (right) from Digital Instruments.

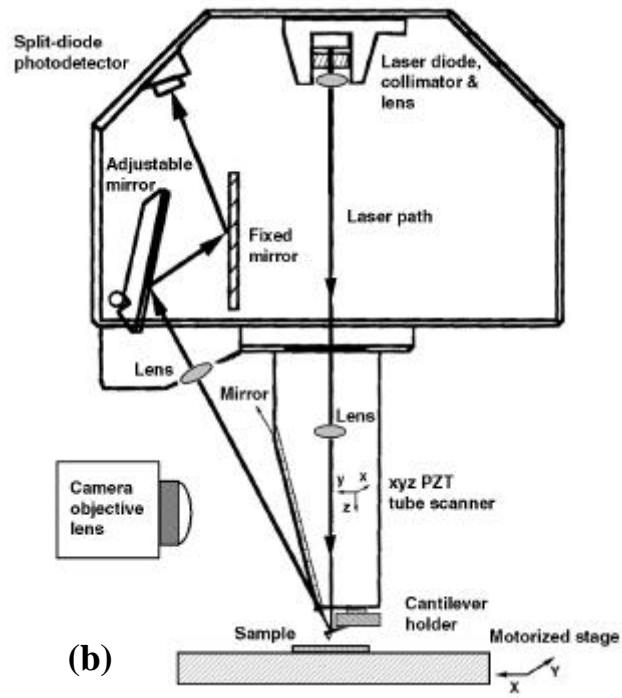
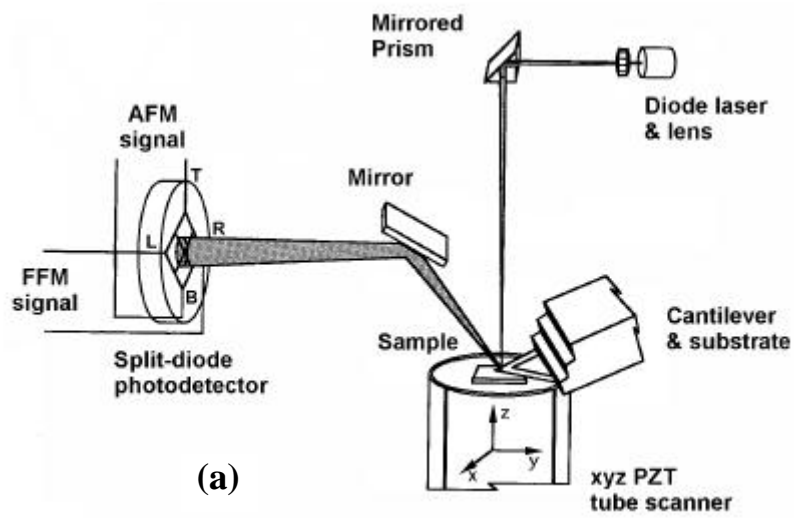


Figure A.2: Schematics of operation of (a) small sample AFM and (b) large sample AFM.

Normal and frictional forces being applied at the tip-sample interface are measured using a laser beam deflection technique. A laser beam generated from a diode laser (wavelength – 670 nm, peak power output – 5 mW) is directed by a prism onto the back of the cantilever near the location of the tip. The reflected beam from the cantilever is directed by a mirror onto the quad photodetector (Fig. A.2). When the tip is scanned across a sample, features on the sample surface (roughness etc.) will cause the tip to deflect in the vertical deflection. As a result, the laser spot on the photodetector will deflect vertically. This signal (labeled AFM signal) is used as a feedback signal in the normal mode of AFM operation (known as ‘height’ mode, shown in Fig. A.3). This signal is kept constant during scanning by moving the Z -piezo up or down to keep the deflection of the cantilever constant (i.e. constant normal load) while scanning. Thus the movement of the z-piezo is a direct representation of the surface topography of the sample surface. Normal loads can range from a few nanonewtons to a few hundred micronewtons depending on the cantilever stiffness used. Simultaneous measurements of friction force (FFM signal, explained in A.2) and surface roughness can be made with these instruments when scanning perpendicular to the long axis of the cantilever beam. The only difference between the small -sample AFM and the large -sample one is that in the latter, the tip (rather than the sample) is mounted on the piezo and scanned over a stationary sample as shown in Fig. A.2(b). The large -sample AFM also has a motorized X-Y stage to facilitate location of specific areas on the sample for scanning.

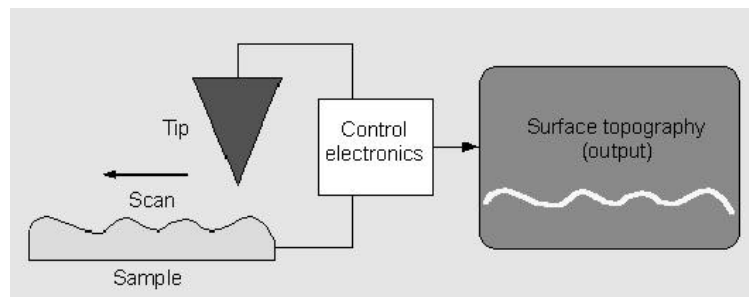


Figure A.3: Schematic of ‘height’ mode operation of an AFM to obtain surface topography.

The AFM can be operated in two basic modes: contact and tapping modes. In contact mode, the tip drags over the surface of the studied sample. Friction and wear measurements are therefore necessarily made in contact mode. In tapping mode, there is intermittent contact between the tip and the sample as the tip is vibrated at a frequency close to the resonance of the cantilever while scanning. Tapping mode images usually result in images with higher lateral resolution than in contact mode because the tips used for tapping mode are much sharper than those used for contact mode. Also tapping mode results in negligible damage to the sample as compared to contact mode.

A.2 Friction measurements

When scanning is performed in contact mode in a direction perpendicular to the long axis of the cantilever beam, friction forces between the tip and the surface cause torsion of the cantilever, which is responsible for the change in the FFM signal (see Fig. A.1). To convert this signal change (measured in Volts) into force units, a number of calibration experiments are needed. A brief description of the calibration procedures developed by Ruan and Bhushan (1994) and which are used in this study is given below.

First, the tip is traced and retraced across the surface parallel to the cantilever axis for a number of contact forces. The plot of profile separation (directly measured on the AFM; called ‘TMR’ signal) versus average piezo center position results in a linear fit as shown in Fig. A.4(a) with a slope given by

$$\mu = \delta(2\ell/L) \quad (\text{A.1})$$

where μ is the coefficient of friction, δ is the slope obtained from the experimental data, ℓ is the distance from the end of the tip to the height of the cantilever base and L is the cantilever length. It is assumed that the normal forces used result in an elastic contact (no ploughing).

Once the coefficient of friction is determined, contact mode scans perpendicular to the cantilever axis are performed, again in the elastic contact regime for various loads. The friction force (FFM) signals for a number of normal loads during trace and retrace scans are obtained. A ‘true’ friction signal is obtained by $\{FFM_{\text{trace}} - FFM_{\text{retrace}}\}/2$ in

order to eliminate errors due to misalignment between the vertical deflection line of the cantilever and the vertical line of the photodetector (Ruan and Bhushan, 1994). A plot of true friction signal versus the normal load is obtained as shown in Fig. A.4(b). By equating the slope of this plot (Volts/Newton) to the value of coefficient of friction, the torsional conversion factor for the FFM signal in Newtons/Volt can be obtained for the given tip/cantilever.

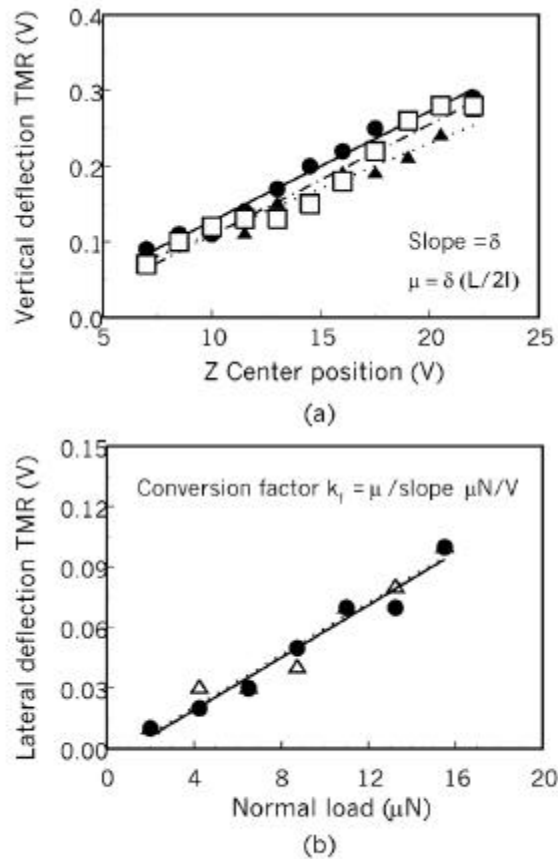


Figure A.4: Friction calibration data obtained on Al_2O_3 . (a) Three data sets of Trace minus Retrace (TMR) value of surface height as a function of normal load. The slope of this plot δ , is related to the coefficient of friction μ between sample and tip. (b) Two data sets of true friction signal as a function of normal load. Equating the slope of this plot to μ obtained from (a), the conversion factor to convert lateral deflection signal to friction force can be obtained.

A.3 Scratch/wear experiments at constant load

Figure A.5 shows schematics of scratch and wear experiments with the AFM. For scratching and wear studies, the sample is scanned with a diamond tip (tips are described in section A.4) in a direction normal to that of the long axis of the cantilever beam typically at a rate of 0.5 Hz. For scratch studies, ten reciprocatory scratches (5 μm scratch length) are made at different normal loads. For wear studies, typically an area of 2 μm x 2 μm is scanned at various normal loads for a selected number of cycles (effect of normal load). In order to study evolution of wear, a normal load is selected and the number of cycles is varied. An area larger than the scratched or worn regions is scanned at a low normal load of about 0.5 – 0.8 μN using the same diamond tip to observe the scratch or wear marks. In addition to these techniques, adhesive forces between the tip and sample can be measured directly with the AFM.

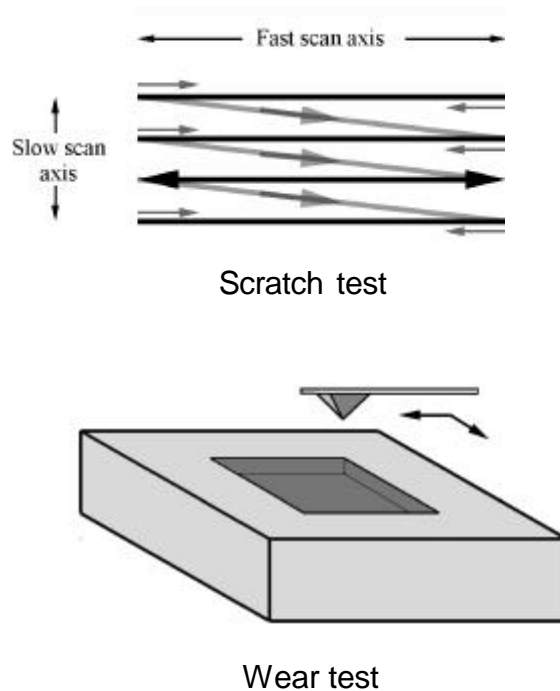


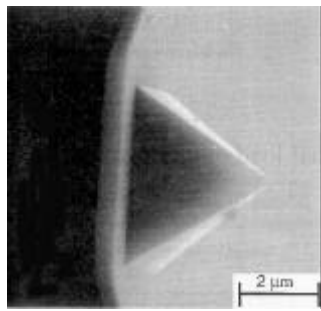
Figure A.5: Schematics of micro/nanoscale scratch and wear tests conducted using an AFM.

A.4 Tips used in AFM/FFM studies

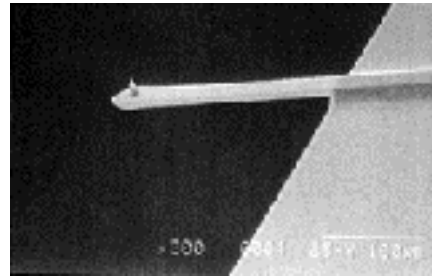
Figure A.6 shows the various tips that are used in the AFM. For contact mode measurements, a microfabricated square pyramidal Si_3N_4 tip with a tip radius of about 50 nm on a Si_3N_4 cantilever beam (normal beam stiffness of about 0.6 N/m) is generally used at normal loads ranging from 10 to 500 nN. Microfabricated Si tips (radius of about 5 – 10 nm) on rectangular silicon beams (stiffness 2 – 100 N/m) are used for tapping mode measurements. For scratching and wear experiments, the diamond tip/stainless steel cantilever assembly is used. The diamond tip is a three-sided pyramid (apex angle of 60° and radius of ~ 100 nm) and the stiffness of the cantilever can be adjusted by adjusting the cantilever length. The stiffness of the beam is obtained by approximating it to be the spring constant of an end-loaded cantilever beam of rectangular cross-section, which is given by

$$k = \frac{Et^3w}{4L^3} \quad (\text{A.2})$$

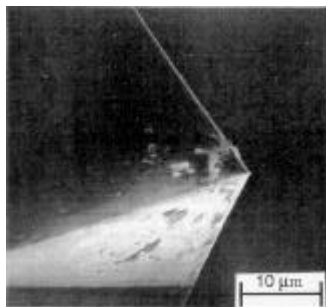
where E is the elastic modulus, t is the thickness, w is the width and L is the length of the cantilever beam as seen in Fig. A.7. By changing the length of the beam in the cantilever holder, the desired spring constant can be obtained. Normal loads in the range of 0.5 – 500 μN can be obtained by varying the stiffness.



Si₃N₄ tip



Si tip



Diamond tip

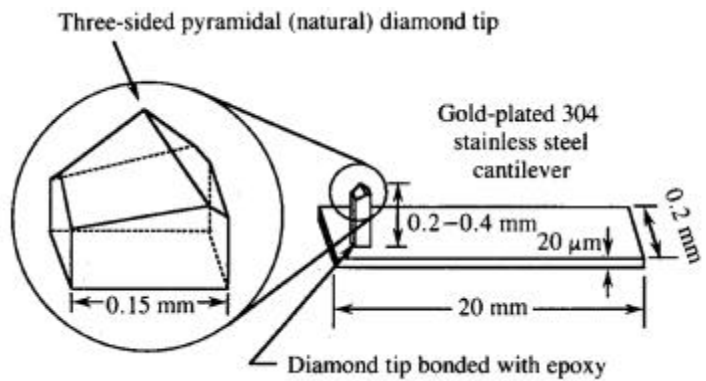


Figure A.6: Tips used in AFM/FFM.

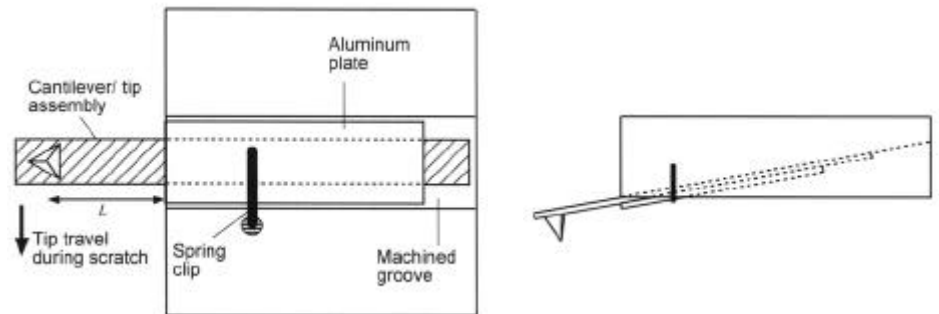


Figure A.7: Schematic of diamond tip -cantilever assembly mounted in an AFM cantilever holder. The cantilever sits in the machined groove. The thin aluminum plate and spring clip provide rigid clamping of the cantilever. The cantilever length L can be varied.

APPENDIX B

MACROS FOR CONTROLLED TIP MOVEMENT FOR VARIOUS AFM EXPERIMENTS

Several of the experiments performed using the AFM required movement of the tip in ways totally different from the usual raster scanning. This requirement was met by using the *lithography* module of the Nanoscope controller . This module allows the user to write macros (or programs) that direct the controller to perform controlled movements of the piezo. This programming interface is called *NanoscriptTM* and is based on the ‘C’ programming language and uses the same syntax and conventions. The one disadvantage of the lithography module is that during the execution of the macros, data collection and processing are disabled (as designed by Digital Instruments). In other words, the signals of interest must be tapped out of the microscope and collected independently.

This appendix contains the macros written for various experiments performed in this research. More details on the commands and other information on the Lithography module and Nanoscript can be found in the Nanoscope Command Reference Manual from Digital Instruments.

B.1 Continuous microscratch experiment

```
#include <litho.h>

void main()
{
    LITHO_BEGIN

    LithoDisplayStatusBox();
    LithoScan(FALSE);           // Turn off scanning
    LithoCenterXY();           // Move tip to center of field
}
```

```

// Input parameters

double scr_lngth = 25;      // Scratch length in microns
int incr = 500;           // Normal load increments
double rate = 0.5;        // Speed of tip in microns/second
double fstep = 0.02;      // Magnitude of normal load increment
                           // Since this is achieved by varying setpoint, units are Volts
double dir = -1;          // 1 is positive scratch dir and -1 is neg (defined for piezo)
double dstep = dir*(scr_lngth/incr); // Length of segment for each normal load increment
int i;

// Commands start here

LithoPause(5);
LithoTranslate(-dir*(scr_lngth/2),0,2); // Move to beginning of scratch

LithoPulseOutput(aoAna1,3,2); // Wait for 8 seconds,send pulse of 5V

// Scratch with increasing normal load

for (i=1;i<=incr;i++)
{
    LithoSetSetpoint(fstep);
    LithoTranslate(dstep,0,rate);
}
LithoSetSetpoint(-2);
LithoPulseOutput(aoAna1,3,1); // Control signal indicating end of test

LITHO_END

}

```

B.2 Quasi-static bending of nanobeams

This macro is run after locating the tip at the center of the beam span.

```

#include <litho.h>

void main()
{
    LITHO_BEGIN

    LithoDisplayStatusBox();
    LithoScan(FALSE); // Turn off scanning
    LithoCenterXY(); // Move tip to center of field

    // input parameters

    double depth = -2.50; // Z displacement of piezo into sample (microns)
    double z_rate = 0.010; // Rate of Z displacement in microns/second

```

```

// Commands start here

LithoPause(2);
LithoPulse(IsAna1,2.0,1.0); // Signal indicating start of test
LithoPause(1);

LithoPulse(IsAna1,2.0,1.0); // Signal indicating start of piezo motion
LithoMoveZ(depth,z_rate); // Move piezo down
LithoPulse(IsAna1,2.0,2.0); // Signal indicating end of piezo forward movement

LithoMoveZ(-(depth),0.2); // Move piezo back to where it was

LithoPulse(IsAna1,2.0,2.0); // Signal indicating end of test

LITHO_END
}

```

B.3 Monotonic-cyclic loading of nanobeams

This macro is run after locating the tip at the center of the span.

```

#include <litho.h>

void main()
{
    LITHO_BEGIN

    LithoDisplayStatusBox();
    LithoScan(FALSE); // Turn off scanning
    LithoCenterXY(); // Move tip to center of field

    //variable values are in MICRONS

    double first_depth = -0.3; // Initial Z displacement of piezo towards sample
    // to ensure a minimum load on the beam
    double rept_depth = 0.7; // Magnitude of cyclic displacement
    double z_rate = 20*rept_depth; // Rate of Z displacement in micr/s is 20*rept_depth
    // for target 10 Hz. This results in 4.2 Hz response

    double up_val = rept_depth;
    double down_val = -(rept_depth);
    double correct_depth = -0.075; // magnitude of compensation for piezo drift
    int i,j;

    // Commands start here

    LithoPause(2);
    LithoPulse(IsAna1,2.0,1.0); // Signal indicating start of piezo motion
    LithoMoveZ(first_depth,0.025); // Moves piezo towards beam to ensure minimum normal load

    // The following is an infinite loop where cyclic displacement of piezo occurs

```

```

// Test is stopped manually when failure of beam is observed by hitting abort on screen

while(1)
{
  for(i=0;i<=1000;i++)
  {
    LithoMoveZ(down_val,z_rate);    // Move piezo down
    LithoMoveZ(up_val,z_rate);     // Move piezo up
  }
  LithoPulse(IsAna1,2.0,2.0);
  LithoMoveZ(correct_depth,0.025); // Compensate for drift of piezo by increasing initial load
                                   // every 5 minutes

  i=0;
  j=j+1;
  if (j == 5)
  {
    correct_depth = correct_depth - 0.025; // Increase magnitude of drift compensation by
                                             // 30% over time (about 20 minutes)

    j = 0;
  }
}

LITHO_END

}

```

APPENDIX C

SURFACE ROUGHNESS PARAMETERS

All solid surfaces, however smooth they may seem to the naked eye, are comprised of random and/or repetitive variations in surface height. These deviations are also known as surface roughness. Surface roughness is always associated with a length scale. This is because the magnitude of the surface height deviations (or roughness) can be different at different length scales for the same surface as shown in Fig. C.1. Fluctuations that have a long wavelength in particular form the waviness of a surface while deviations that are found on a shorter wavelength are commonly associated with the term ‘surface roughness’. Surface roughness is characterized by peaks or asperities and depressions or valleys of various magnitudes as shown in Fig. C.1.

Surface Roughness Parameters

Surface roughness parameters describe the vertical deviations in surface height that comprise the roughness and are statistical descriptors of the distribution of the surface heights, when measured with respect to a reference plane. Since most surface roughness is random, the distribution of the surface heights usually follows a Gaussian distribution (Fig. C.2). The most common measures of surface roughness are the centerline-average (CLA) or R_a and root mean square roughness (RMS) or R_q . If we consider a profile $z(x)$ of length L in which profile heights are measured from a mean line, then

$$R_a = CLA = \frac{1}{L} \int_0^L |z - m| dx \quad (C.1)$$

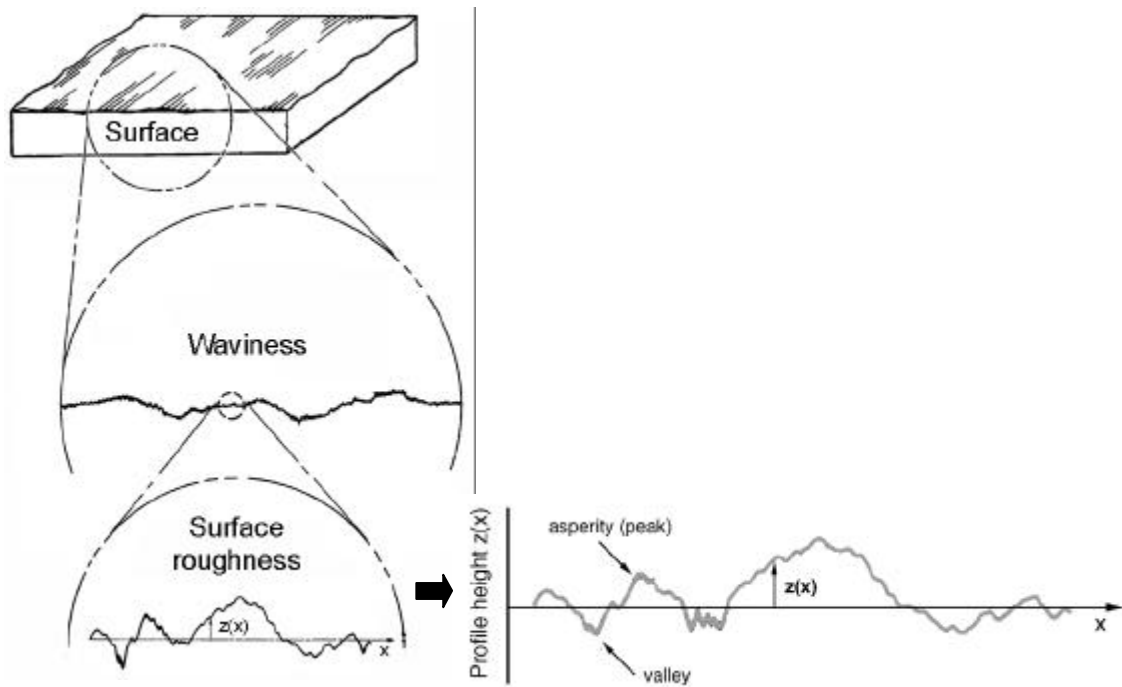


Figure C.1: Surface roughness of solid surfaces.

and

$$R_q^2 = RMS^2 = \frac{1}{L} \int_0^L z^2 dx \quad (C.2)$$

where $m = \frac{1}{L} \int_0^L z dx .$

The variance of the distribution, σ , is given by

$$s^2 = \frac{1}{L} \int_0^L z^2 dx = R_q^2 - m^2 \quad (C.3)$$

Skewness and Kurtosis

The skewness (Sk) of a surface height distribution is a measure of the asymmetry in the distribution. A Gaussian distribution is a symmetric distribution and therefore has a skewness of zero. In mathematical terms, skewness is the third moment about the mean

of the surface height distribution function. Skewness is usually represented in the normalized form as:

$$Sk = \frac{1}{S^3 L} \int_0^L (z - m)^3 dx \quad (C.4)$$

The kurtosis of a surface height distribution represents the ‘peakedness’ of the distribution and is a measure of the pointedness or bluntness of the distribution function. Gaussian distributions have a kurtosis value of 3. In mathematical terms, kurtosis is the fourth moment about the mean of the surface height distribution. Kurtosis is usually represented in the normalized form as:

$$K = \frac{1}{S^4 L} \int_0^L (z - m)^4 dx \quad (C.5)$$

Figure C.2 shows a Gaussian distribution function as well as distribution functions with various skewness and kurtosis values.

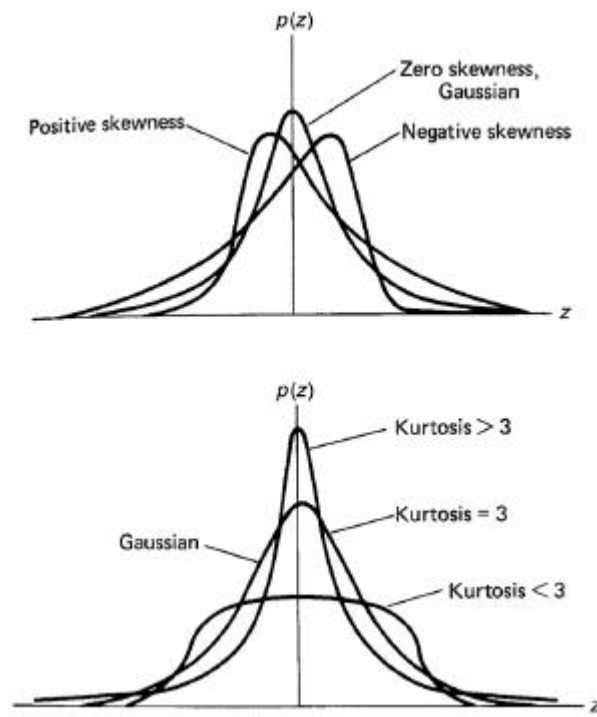


Figure C.2: Surface height distributions with different values of skewness and kurtosis. Most surfaces have a Gaussian distribution of surface heights, with skewness of 0 and kurtosis of 3.

Figure C.3 shows examples of surfaces with different skewness and kurtosis values. A surface with a Gaussian distribution has peaks and valleys evenly distributed about the mean. A surface with negative skewness has more peaks with heights close to the mean as compared to a Gaussian distribution. A surface with positive skewness has a wider range of peak heights that are higher than the mean. A surface with very low kurtosis has more local maxima (asperities) above the mean as compared to a Gaussian distribution, while a surface with very high kurtosis has fewer asperities above the mean.

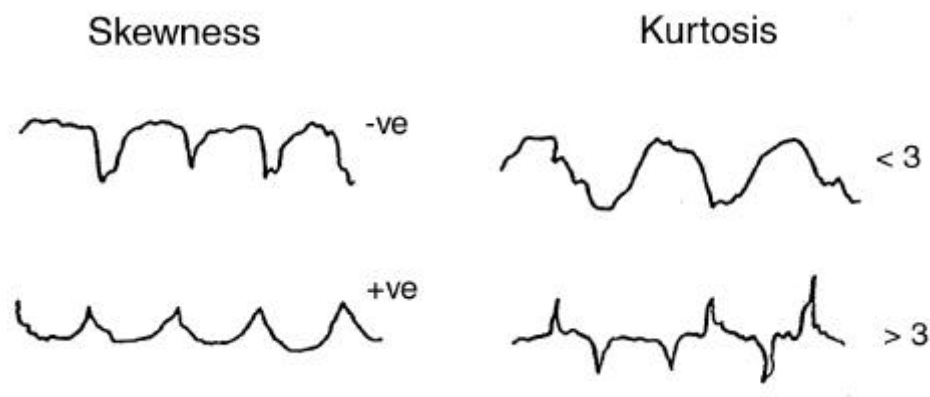


Figure C.3: Examples of surface profiles with different values of skewness and kurtosis.

BIBLIOGRAPHY

- Anonymous (1996), *Nanoscope Command Reference Manual, Version 4.22ce*, Digital Instruments.
- Anonymous (1988), *Properties of silicon*, EMIS Datareviews Series No. 4, INSPEC, Institution of Electrical Engineers, London.
- Ballarini, R., Mullen, R.L., Yin, Y., Kahn, H., Stemmer, S. and Heuer, A.H. (1997), "The fracture toughness of polysilicon microdevices: A first report", *J. Mater. Res.* **12**, 915-922.
- Becker, E. W., Ehrfeld, W., Hagmann, P., Maner, A., and Munchmeyer, D. (1986), "Fabrication of Microstructures with High Aspect Ratios and Great Structural Heights by Synchrotron Radiation Lithography, Galvanoforming, and Plastic Moulding (LIGA Process)", *Microelectronic Eng.* **4**, 35-56.
- Beerschwinger, U., Albrecht, T., Mathieson, D., Rueben, R.L., Yang, S.J. and Taghizadeh, M. (1995), "Wear at microscopic scales and light loads for MEMS applications", *Wear*, **181-183**, 426-435.
- Beerschwinger, U., Yang, S. J, Reuben, R. L., Taghizadeh, M. R., and Wallrabe, U. (1994), "Friction Measurements on LIGA-Processed Microstructures", *J. Micromech. Microeng.* **4**, 14-24.
- Behary, N., Ghenaaim, A., El -Achari, A. and Caze, C. (2000), "Tribological Analysis of Glass Fibers using Atomic Force Microscopy (AFM)/Lateral Force Microscopy (LFM)", *J. Appl. Polymer Sci.* **75**, 1013-1025.
- Benjamin, P. and Weaver, C. (1960), "Measurement of Adhesion of Thin Films", *Proc. R. Soc. London A* **254**, 163-176.
- Bhattacharya, A.K. and Nix, W.D. (1988), "Analysis of Elastic and Plastic Deformation Associated with Indentation of Thin Films on Substrates", *Int. J. Solids Structures* **24**(12), 1287-1298.
- Bhushan, B. (1996), *Tribology and Mechanics of Magnetic Storage Devices*, 2nd ed., Springer-Verlag, New York.
- Bhushan, B. (1998), *Tribology Issues and Opportunities in MEMS*, Kluwer Academic, Dordrecht, Netherlands.
- Bhushan, B. (1999a), *Handbook of Micro/nanotribology*, 2nd ed., CRC, Boca Raton, FL.

- Bhushan, B. (1999b), *Principles and Applications of Tribology*, Wiley, New York.
- Bhushan, B. and B.K. Gupta (1991), *Handbook of Tribology: Materials, coatings and surface treatments*, McGraw Hill, New York.
- Bhushan, B. and Gupta, B.K. (1997), *Handbook of Tribology: Materials, Coatings and Surface Treatments*, Reprint edition, Krieger, Malabar, FL.
- Bhushan B. and Koinkar, V.N. (1994), "Tribological Studies of Silicon for Magnetic Recording Applications", *J. Appl. Phys.* **75**, 5741-5746.
- Bhushan, B. and Koinkar, V.N. (1995), "Microscale mechanical and tribological characterization of hard amorphous coatings as thin as 5 nm for magnetic disks", *Surface Coatings and Technology*, **76-77**, 655-669.
- Bhushan, B. and Li, X. (1997), "Micromechanical and tribological characterization of doped single-crystal silicon and polysilicon films for microelectromechanical systems", *J. Mat. Res.* **12**, 54-63.
- Bhushan, B. and Ruan, J. (1994), "Atomic -Scale Friction Measurements Using Friction Force Microscopy: Part II - Application to Magnetic Media", *ASME J. Tribol.* **116**, 389-396.
- Bhushan, B. and Sundararajan, S. (1998), "Micro/Nanoscale Friction and Wear Mechanisms of Thin Films Using Atomic Force and Friction Force Microscopy", *Acta Materialia*, **46**, 3793-3804.
- Bhushan, B. and Venkatesan, S. (1993), "Mechanical and tribological properties of silicon for micromechanical applications: A review", *Advances in Information Storage Systems* **5**, 211-239.
- Bhushan, B. and Zhao, Z. (1999), "Macroscale and Microscale Tribological Studies of Molecularly Thick Boundary Layers of Perfluoropolyether Lubricants for Magnetic Thin-Film Rigid Disks", *J. Info. Storage Proc. Syst.* **1**, 1-21.
- Bhushan, B., Gupta, B.K and Azarian, M.H. (1995a), "Nanoindentation, Microscratch, Friction and Wear Studies of Coatings for Contact recording Applications", *Wear* **181-183**, 743-758.
- Bhushan, B., Kulkarni, A.V., Koinkar, V.N., Boehm, M., Odoni, L., Martelet, C. and Belin, M. (1995b), "Microtribological characterization of self-assembled and Langmuir-Blodgett monolayers by atomic force and friction force microscopy", *Langmuir* **11**, 3189-3198.
- Bhushan, B., Kulkarni, A.V., Bonin, W. and Wyrobek, J. T. (1996), "Nanoindentation and Picoindentation Measurements Using a Capacitive Transducer System in Atomic Force Microscopy", *Phil. Mag. A* **74**, 1117-1128.
- Binnig, G., Quate, C.F. and Gerber, Ch. (1986), "Atomic Force Microscope", *Phys. Rev. Lett.* **56**, 930-933.
- Blackman, G.S., Mate, C.M. and Philpott, M.R. (1990), "Atomic force microscope studies of lubricant films on solid surfaces", *Vacuum* **41**, 1283-1286.

- Bluhm, H., Schwarz, U.D., Meyer, K.P. and Wiesendanger, R. (1995), "Anisotropy of Sliding Friction on the Triglycine Sulfate (010) Surface", *Appl. Phys. A* **61**, 525-533.
- Bonnell, D.A. (2001), *Scanning probe microscopy and spectroscopy : theory, techniques, and applications*, Wiley-VCH, New York.
- Bryzek, J., Peterson, K., and McCulley, W. (1994), "Micromachines on the March", *IEEE Spectrum* May, 20-31.
- Bull, S. J. (1995), "Tribology of carbon coatings: DLC, diamond and beyond", *Diamond and Rel. Mater.* **4**, 827-836.
- Callahan, D. L. and Morris, J. C. (1992), "The Extent of Phase Transformation in Silicon Hardness Indentation", *J. Mater. Res.* **7**, 1612-1617.
- Camon, H., LAAS-CNRS, Toulouse, France, personal communications (2000).
- Conedera, V., Fabre, N., Camon, H., Rousset, B., Pham, H.H. and Solano, C. (1995), "First steps towards the fabrication of electrostatic micromotors using SOG", *Sensors and Actuators A* **46-47**, 82-84.
- Connally, J.A. and Brown, S.B. (1993), "Micromechanical fatigue testing", *Exp. Mech.* **33**, 81-90.
- Core, T. A., Tsang, W. K., and Sherman, S. J. (1993), "Fabrication Technology for an Integrated Surface-Micromachined Sensor", *Solid State Technol.* **36** (Oct), 39-47.
- Deng, K., Collins, R.J., Mehregany, M. and Sukenik, C.N. (1995), "Performance impact of monolayer coatings of polysilicon micromotors", *Proc. MEMS 95*, Amsterdam, Netherlands, Jan -Feb.
- DeVecchio, D. and Bhushan, B. (1998), "Use of a nanoscale Kelvin probe for detecting wear precursors", *Rev. Sci. Instr.* **69** (10), 3618-3624.
- Dodson, B. (1994), *Weibull Analysis*, Quality Press, Milwaukee.
- Ericson, F. and Schweitz, J. (1990), "Micromechanical Fracture Strength of Silicon", *J. Appl. Phys.* **68**, 5840-5844.
- Fan, L. S. and Woodman, S. (1995), "Batch Fabrication of Mechanical Platforms for High-density Data Storage", *8th Int. Conf. Solid State Sensors and Actuators (Transducers '95)/Euroensors IX*, Stockholm, Sweden, 25-29 June, pp. 434-437.
- Fan, L. S., Ottesen, H. H., Reiley, T. C., and Wood, R. W. (1995), "Magnetic Recording Head Positioning at Very High Track Densities Using a Microactuator-based, Two-stage Servo System", *IEEE Trans. Ind. Electron.* **42**, 222-233.
- Fitzgerald, A.M., Dauskardt, R.H. and Kenny, T.W. (2000), "Fracture toughness and crack growth phenomena of plasma -etched single crystal silicon", *Sensors and Actuators A* **83**, 194-199.
- Forschungszentrum Karlsruhe GmbH, Technik und Umwelt, Project Mikrosystemtechnik (PMT), Karlsruhe, Germany.

- Friedrich, C. R. and Warrington, R. O. (1998), "Surface Characterization of Non - Lithographic Micromachining", *Tribology Issues and Opportunities in MEMS* (B. Bhushan, ed.), pp. 73-84, Kluwer Academic, Dordrecht, Netherlands.
- Fujimasa, I. (1996), *Micromachines: A New Era in Mechanical Engineering*, Oxford University Press, Oxford, U.K.
- Gabriel, K.J., Behi, F., Mahadevan, R. and Mehre gany, M. (1990), "In situ friction and wear measurement in integrated polysilicon mechanisms", *Sensors and Actuators A* **21-23**, 184-188.
- Gane, N. and Cox, J. M. (1970), "The Micro-hardness of Metals at Very Light Loads", *Philos. Mag.* **22**, 881-891.
- Grafstrom, S., Ackermann, J., Hagen, T., Neumann, R. and Probst, O. (1994), "Analysis of Lateral Force Effects on the Topography in Scanning Force Microscopy", *J. Vac. Sci. Technol. B* **12**, 1559-1564.
- Greek, S., Ericson, F., Johansson, S., Furtch, M. and Rump, A. (1999), "Mechanical characterization of thick polysilicon films: Young's modulus and fracture strength evaluated with microstructures", *J. Micromech. Microeng.* **9**, 245-251.
- Guckel, H. and Burns, D. W. (1989), "Fabrication of Micromechanical Devices from Polysilicon Films with Smooth Surfaces", *Sensors and Actuators* **20**, 117-122.
- Gupta, B.K. and Bhushan, B. (1995a), "Micromechanical properties of amorphous carbon coatings deposited by different deposition techniques", *Thin Solid Films* **270**, 391-398.
- Gupta, B.K. and Bhushan, B. (1995b), "Mechanical and tribological properties of hard carbon coatings for magnetic recording heads", *Wear* **190**, 110-122.
- Hamilton, H. (1991), "Contact Recording on Perpendicular Rigid Media", *J. Mag. Soc. Jpn.* **15** (Suppl. S2), 483-481.
- Hattori, T., Ejiri, Y. and Sato, K. (1994), "Fabrication of nanometer -scale structures using atomic force microscopy with conducting probe", *J. Vac. Sci. Technol. A* **12**, 2586-2590.
- Haugstad, G. and Gladfelter, W.L. (1993), "Friction Force Microscopy of AgBr Crystals: Ag⁰ Rods and Adsorbed Gelatin Films", *Langmuir* **9**, 3717-3721.
- Hector, L.G. and Schmid, S.R. (1998), "Simulation of asperity plowing in an atomic force microscope Part I: Experimental and theoretical methods", *Wear* **215**, 247-256.
- Henck, S. A. (1997), "Lubrication of Digital Micromirror Devices", *Tribol. Lett.* **3**, 239-247.
- Hertzberg, R.W., *Deformation and Fracture Mechanics of Engineering Materials*, 3rd ed, John Wiley, New York 1989, pp. 277-278
- Holmberg, K. and Matthews, A. (1994), *Coatings Tribology: Properties, Techniques and Applications in Surface Engineering*, Elsevier, New York.

- Hornbeck, L. J. (1999), "A Digital Light Processing(tm) Update - Status and Future Applications (Invited)", *Proc. Soc. Photo-Opt. Eng.* **3634**, *Projection Displays V*, 158-170.
- Hornbeck, L. J. and Nelson, W. E. (1988), "Bistable Deformable Mirror Device", *OSA Technical Digest Series Vol. 8: Spatial Light Modulators and Applications*, 107-110.
- Horsley, D. A., Cohn, M. B., Singh, A., Horowitz, R., and Pisano, A. P. (1998), "Design and Fabrication of an Angular Microactuator for Magnetic Disk Drives", *J. Microelectromech Syst.* **7**, 141 – 148.
- Jacobson, S., Jonsson, B., and Sundquist, B. (1983), "The Use of Fast Heavy Ions to Improve Thin Film Adhesion", *Thin Solid Films* **107**, 89-98.
- Jaeger, R. C. (1988), *Introduction to Microelectronic Fabrication*, Vol. 5, Addison-Wesley, Reading, MA.
- Johansson, S., Schweitz, J.A., Tenerz, L. and Tiren, J. (1988), "Fracture testing of silicon microelements in -situ in a scanning electron microscope", *J. Appl. Phys.* **63**, 4799-4803.
- Johansson, S., Ericson, F. and Schweitz, J.A. (1989), "Influence of surface -coatings on elasticity, residual -stresses, and fracture properties of silicon microelements", *J. Appl. Phys.* **65**, 122-128.
- Kahn, H., Ballarini, R., Mullen, R.L . and Heuer, A.H. (1999), "Electrostatically actuated failure of microfabricated polysilicon fracture mechanics specimens," *Proc. R. Soc. Lond. A* **455**, 3807-3823.
- Kodali, P., Walter, K.C. and Nastasi, M. (1997), " Investigation of mechanical and tribological properties of amorphous diamond-like carbon coatings", *Tribol. Int.* **30**, 591-598.
- Koinkar, V.N. and Bhushan, B. (1996a), "Micro/nanoscale Studies of Boundary Layers of Liquid Lubricants for Magnetic Disks", *J. Appl. Phys.* **79**, 8071-8075.
- Koinkar, V.N. and Bhushan, B. (1996b), "Microtribological Studies of Unlubricated and Lubricated Surfaces Using Atomic Force/Friction Force Microscopy", *J. Vac. Sci. Technol. A* **14**, 2378-2391.
- Koinkar, V.N. and Bhushan, B. (1997), "Effect of Scan Size and Surface Roughness on Microscale Friction Measurements", *J. Appl. Phys.* **81**, 2472-2479.
- Komai, K., Minoshima, K. and Inoue, S. (1998), "Fracture and fatigue behavior of single crystal silicon microelements and nanoscopic AFM damage evaluation", *Microsystem Technologies* **5**, 30–37.
- Komvopoulos, K (1996), "Surface engineering and microtribology for microelectro - mechanical systems", *Wear* **200**, 305-327.
- Kovacs, G. T. A. (1998), *Micromachined Transducers Sourcebook*, WCB McGraw-Hill, Boston, MA.

- Lehr, H. Abel, S., Doppler, J., Ehrfeld, W., Hagemann, B., Kamper, K. P., Michel, F., Schulz, Ch., and Thurigen, Ch. (1996), "Microactuators as Driving Units for Microrobotic Systems", in *Proc. Microrobotics: Components and Applications* (A. Sulzmann, ed.), Vol. 2906, pp. 202-210, SPIE.
- Lehr, H., Ehrfeld, W., Hagemann, B., Kamper, K. P., Michel, F., Schulz, Ch., and Thurigen, Ch. (1997), "Development of Micro-Millimotors", *Min. Invas. Ther. Allied Technol.* **6**, 191-194.
- Lettington, A.H. (1998), "Applications of diamond-like carbon thin films", *Carbon* **36** 555-560.
- Li, X. and Bhushan, B. (1998), "Micromechanical and tribological characterization of hard amorphous carbon coatings as thin as 5 nm for magnetic recording heads", *Wear* **220**, 51-58.
- Li, X. and Bhushan, B. (1999), "Micro/Nanomechanical and Tribological Characterization of Ultra-Thin Amorphous Carbon Coatings", *J. Mat. Res.* **14**, 2328-2337.
- Lim, M. G., Chang, J. C., Schultz, D. P., Howe, R. T., and White, R. M. (1990), "Polysilicon Microstructures to Characterize Static Friction", *Proc. IEEE 3rd MEMS Workshop*, Napa Valley, CA, USA, Feb 1990, pp. 82-88.
- Maboudian, R. (1998), "Adhesion and friction issues associated with reliable operation of MEMS", *MRS Bulletin* June, 47-51.
- Maboudian, R. and Howe, R.T. (1997), "Critical review: Adhesion in surface micromachined structures", *J. Vac. Sci. Technol. B* **15**, 1-20.
- Madou, M. (1997), *Fundamentals of Microfabrication*, CRC Press, Boca Raton, Florida.
- Makinson, K.R. (1948), "On the cause of frictional variations of the wool fiber", *Trans. Faraday Soc.* **44**, 279-282.
- Mastrangelo, C. H. and Hsu, C. H. (1993), "Mechanical Stability and Adhesion of Microstructures Under Capillary Forces", *J. Microelectromech. Syst.* **2**, 33-55.
- Mastrangelo, C.H. (1997), "Adhesion-related failure mechanisms in micromechanical devices", *Trib. Lett.* **3**, 233-238.
- Mate, C.M. (1993), "Nanotribology Studies of Carbon Surfaces by Force Microscopy", *Wear* **168**, 17-20.
- Matheison, D., Beerschwinger, U., Young, S. J., Rueben, R. L., Taghizadeh, M., Eckert, S., and Wallrabe, U. (1996), "Effect of progressive wear on the friction characteristics of nickel LIGA processed rotors", *Wear* **192**, 199-207.
- Mazza, E., Abel, S. and Dual, J. (1996), "Experimental Determination of Mechanical Properties of Ni and Ni-Fe Microbars", *Microsystem Technologies* **2**, 197-202.
- Mehregany, M., Howe, R.T. and Senturia, S.D. (1987), "Novel Microstructures for the In-situ Measurement of Mechanical Properties of Thin Films", *J. Appl. Phys.* **62**, 3579-3584.

- Mehregany, M., Gabriel, K. J., and Trimmer, W. S. N. (1988), "Integrated Fabrication of Polysilicon Mechanisms", *IEEE Trans. Electron Devices*. **35**, 719-723.
- Mehregany, M., Senturia, S. and Lang J.H. (1990), "Friction and Wear in Microfabricated Harmonic Side-drive Motors", *Tech. Digest IEEE Solid State Sensors Actuators Workshop*, New York: IEEE, 17-22.
- Michel, F. and Ehrfeld, W. (1998), "Microfabrication Technologies for High Performance Microactuators" in *Tribology Issues and Opportunities in MEMS* (B. Bhushan, ed.), pp. 53-72, Kluwer Academic, Dordrecht, Netherlands.
- Mittal, K.L. (1978), *Adhesion Measurement of Thin Films, Thick Films and Bulk Coatings*, STP 640, ASTM, Philadelphia.
- Miu, D. K. and Tai, Y. C. (1995), "Silicon Micromachined Scaled Technology", *IEEE Trans. Industr. Electron.* **42**, 234-239.
- Muhlstein, C. and Brown, S. (1998), "Reliability and Fatigue Testing of MEMS", in *Tribology Issues and Opportunities in MEMS* (B. Bhushan, ed.), pp. 519-528, Kluwer Academic, Dordrecht, Netherlands.
- Muller, R. S., Howe, R. T., Senturia, S. D., Smith, R. L., and White, R. M. (1990), *Microsensors*, IEEE Press, New York.
- Muller, T., Lohrmann, M., Kasser, T., Marti, O., Mylnek, J. and Krausch, G. (1997), "Frictional Force between a Sharp Asperity and a Surface Step", *Phys. Rev. Lett.* **79**, 5066-5069.
- Namazu, T., Isono, Y. and Tanaka, T. (2000), "Evaluation of size effect on mechanical properties of single-crystal silicon by nanoscale bending test using AFM", *J. Microelectromech. Syst.* **9**, 450-459.
- Neumister, J.M. and Ducker, W.A. (1994), "Lateral, normal and longitudinal spring constants of atomic force microscope cantilevers", *Rev. Sci. Instrum.* **65**, 2527-2531.
- Nguyen, C.T.C. and Howe, R.T. (1999), "An integrated CMOS micromechanical resonator high-Q oscillator," *IEEE J Solid-St. Circ.* **34**, 440-455.
- O'Sullivan, T.C. and King, R.B. (1988), "Sliding Contact Stress Due to a Spherical Indenter on a Layered Elastic Half-Space", *ASME: J. Trib* **110**, 235-240.
- Ohwe, T., Mizoshita, Y., and Yonoeka, S. (1993), "Development of Integrated Suspension System for a Nanoslider with an MR Head Transducer", *IEEE Trans. Magn.* **29**, 3924-3926.
- Overney, R. and Meyer, E. (1993), "Tribological Investigations using Friction Force Microscopy", *MRS Bulletin* **18**, 26-34.
- Perry, A.J. (1981), "The adhesion of chemically vapour-deposited hard coatings on steel - The scratch test", *Thin Solid Films* **78**, 77-93.
- Peterson, K.E. (1982), "Silicon as a Mechanical Material", *Proc. of the IEEE* **70**, 420-457.

- Pharr, G. M. (1991), "The Anomalous Behavior of Silicon During Nanoindentation", in *Thin Films: Stresses and Mechanical Properties III* (W.D. Nix, J.C. Bravman, E. Arzt and L.B. Freund, eds.) **239**, pp. 301-312, Materials Research Soc., Pittsburgh, PA.
- Pharr, G.M., Oliver, W.C. and Clarke, D.R. (1989), "Hysteresis and discontinuity in the indentation load displacement behavior of silicon", *Scripta Met.* **23**, 1949-1952.
- Poon, C.Y. and Bhushan, B., "Comparison of Surface Roughness Measurements by Stylus Profiler, AFM and Non-contact Optical Profiler", *Wear*, **190**, 1995, 76-88.
- Roark, R.J. (1965), *Formulas for Stress and Strain*, McGraw-Hill, New York.
- Robertson, J. K. and Wise, K. D. (1998), "An Electrostatically Actuated Integrated Microflow Controller", *Sensors and Actuators A* **71**, 98-106.
- Ruan, J. and Bhushan, B. (1994), "Atomic -Scale Friction Measurements Using Friction Force Microscopy: Part I – General Principles and New Measurement Techniques", *ASME J. Tribol.* **116**, 378-388.
- Sandia National Labs (various), images and other information from www.sandia.gov.
- Sargent, P. M. (1986), "Use of the Indentation Size Effect on Microhardness for Materials Characterization", in *Microindentation Techniques in Materials Science and Engineering* (P.J. Blau and B.R. Lawn, eds.), STP 889, pp. 160-174, ASTM, Philadelphia, PA.
- Sato, K., Yoshioka, T., Anso, T., Shikida, M. and Kawabata, T. (1998), "Tensile testing of silicon film having different crystallographic orientations carried out on a silicon chip", *Sensors and Actuators A* **70**, 148-152.
- Sharpe Jr., W.N., Yuan, B. and Edwards, R.L. (1997), "A new technique for measuring the mechanical properties of thin films", *J. Microelectromech. Syst.* **6**, 193-199.
- Snow, E.S. and Campbell, P.M. (1994), "Fabrication of Si nanostructures with an atomic force microscope", *Appl. Phys. Lett.* **64**, 1932-1934.
- Srinivasan, U., Houston, MR, Howe RT, Maboudian R (1998), "Alkyltrichlorosilane - based self-assembled monolayer films for stiction reduction in silicon micromachines", *J. Microelectromech. Syst.* **7**, 252-260.
- Steinmann, P.A., Tardy, Y. and Hintermann, H.E. (1987), "Adhesion testing by Scratch Test Method: The Influence of Intrinsic and Extrinsic Parameters on the Critical Load", *Thin Solid Films* **154**, 333-349.
- Sulouff, R. E. (1998), "MEMS Opportunities in Accelerometers and Gyros and the Microtribology Problems Limiting Commercialization", *Tribology Issues and Opportunities in MEMS* (B. Bhushan, ed.), pp. 109-120, Kluwer Academic, Dordrecht, Netherlands.
- Sundararajan, S. and Bhushan, B. (1999), "Micro/Nanotribology of Ultra -Thin Hard Amorphous Carbon Coatings using Atomic Force/Friction Force Microscopy", *Wear* **225-229**, 678-689.

- Sundararajan, S. and Bhushan, B. (2000), "Topography-Induced Contributions to Friction Forces Measured Using an Atomic Force/Friction Force Microscope", *J. Appl. Phys.* **88**, 4825-4831.
- Sundararajan, S. and Bhushan, B. (2001a), "Static Friction Force and Surface Roughness Studies of Surface Micromachined Electrostatic Micromotors Using an Atomic Force/Friction Force Microscope", *J. Vac. Sci. Technol. A* **19**, 1777-1785.
- Sundararajan, S. and Bhushan, B. (2001b), "Development of a Continuous Microscratch Technique in an Atomic Force Microscope and its Application to Study Scratch Resistance of Ultra-thin Hard Amorphous Carbon Coatings", *J. Mater. Res.* **16**, 437-445.
- Sundararajan, S. and Bhushan, B. (2002), "Development of AFM -based Techniques to Measure Mechanical Properties of Nanoscale Structures", *J. Microelectromech. Syst.* (submitted for publication).
- Sundararajan, S., Bhushan, B., Namazu, T. and Isono, Y. (2002), "Mechanical Property Measurements of Nanoscale Structures Using an Atomic Force Microscope," *Ultramicroscopy* (in press).
- Suzuki, J. and Okada, S. (1995), "Deposition of diamond-like carbon films using electron cyclotron resonance plasma chemical vapor deposition from ethylene gas", *Jpn. J. Appl. Phys.* **34** 1218-1220.
- Tabata, O., Asahi, R., Funabashi, H., Shimaoka, K. and Sugiyama, S. (1992), "Anisotropic etching of silicon in TMAH solutions", *Sensors and Actuators A* **34**, 51-57.
- Tai, Y. C. and Muller, R. S. (1990), "Frictional Study of IC Processed Micromotors", *Sensors and Actuators A* **21-23**, 180-183.
- Tai, Y. C., Fan, L. S., and Muller, R. S. (1989), "IC-Processed Micro-Motors: Design, Technology and Testing", *Proc. IEEE Micro Electro Mechanical Systems*, 1-6.
- Tamayo, J., Garcia, R., Utzmeier, T. and Briones, F. (1997), "Submonolayer Sensitivity of InSb on InP Determined by Friction Force Microscopy", *Phys. Rev. B* **55**, R13 436-R13 439.
- Trimmer, W. S. (ed.) (1997), *Micromachines and MEMS, Classic and Seminal Papers to 1990*, IEEE Press, New York.
- Tsuchiya, T., Inoue, A. and Sakata, J. (2000), "Tensile testing of insulating thin films: humidity effect on tensile strength of SiO₂ films", *Sensors and Actuators A* **82**, 286-290.
- Tsuchiya, T., Tabata, O., Sakata, J. and Taga, Y. (1998), "Specimen size effect on tensile strength of surface-micromachined polycrystalline silicon thin films", *J. Microelectromech. Syst.* **7**, 106-113.
- Valli, J. (1986), "A Review of Adhesion Test Method for Thin Hard Coatings", *J. Vac. Sci. Technol. A* **4**, 3007-3014.

- Wang, K., Wong, A.C. and Nguyen, C.T.C. (2000), "VHF Free-Free Beam High-Q Micromechanical Resonators", *J. Microelectromech. Syst.* **9**, 347-360.
- Weibull, W. (1951), "A statistical distribution of wide applicability", *J. Appl. Mech.* **18**, 293.
- Wiesendanger, R. (1994), *Scanning probe microscopy and spectroscopy : methods and applications*, Cambridge University Press, Cambridge, UK.
- Wilson, C.J. and Beck, P.A. (1996), "Fracture testing of bulk silicon microcantilever beams subjected to a side load", *J. Microelectromech. Syst.* **5**, 142-150.
- Wilson, C.J., Ormeggi, A. and Narbutovskih, M. (1996), "Fracture Testing of Silicon Micro Cantilever Beams", *J. Appl. Phys.* **79**, 2386-2393.
- Wu, T.W. (1991), "Microscratch and Load Relaxation Tests for Ultra -thin Films", *J. Mater. Res.* **6**, 407-426.
- Yi, T., Li, L. and Kim, C.J. (2000), "Microscale material testing of single crystalline silicon: process effects on surface morphology and tensile strength", *Sensors and Actuators A* **83**, 172-178.
- Zhao, X. and Bhushan, B. (1998), "Material removal mechanisms of single -crystal silicon on nanoscale and at low loads", *Wear* **223**, 66-78.
- Zhao, Z. and Bhushan, B. (1996), "Effect of Bonded-Lubricant Films on the Tribological Performance of Magnetic Thin -Film Rigid Disks", *Wear* **202**, 50-59.